2018 International Students and Young Scientists Workshop

'Optoelectronics and Microsystems Packaging'

November 22nd - 24th, Dresden

TECHNISCHE UNIVERSITÄT DRESDEN

Wrocław University of Science and Technology

SNS ICM

Proceedings of
2018 International Students and Young Scientists Workshop

"Optoelectronics and Microsystems Packaging"

22-24 November 2018, Dresden, Germany

Wydawnictwo GMORK
Wrocław 2019

Editors:
Sergiusz Patela, Associate Professor
Wojciech Kijaszek, MSc
Dariusz Przybylski, MSc

Cover design:
Marta Turkiewicz, MSc

Wydawnictwo Gmork Swiatkowska Ryba Sp.j.
Ignacego Domeyki 16, 53-209 Wrocław, Poland
http://www.gmork.pl; e-mail: wydawnictwo@gmork.pl

ISBN: 978-83-951333-3-6

TABLE OF CONTENTS

Introduction 6

Hybrid materials having plasmonic and photochromic unit 7
D. Benkowska, E. Barrez, G. Laurent

Brief introduction to deep level transient spectroscopy 12
M. Glinkowski, B. Paszkiewicz, R. Paszkiewicz

DeploScope – A Modular Deployable CubeSat Telescope 18
A. Graja, M. Ćwikła, P. Kwapisz

Optical and structural properties of amyloids obtained from bovine insulin 25
M. Grelich, A. Grzesik, J. Olesiak-Bańska

Comparison of multilayered Au based and Au free ohmic contacts to AlGaN/GaN heterostructures 31
G. Ilgiewicz, W. Macherzyński, R. Paszkiewicz

Microfluidic micropot – fully 3D printed innovative tool for seed quality assessment 37
B. Kawa, K. Adamski, D. Lizanets, R. Walczak

The influence of quantum well and barrier thicknesses on PL spectra of InGaAs/AlInAs superlattices grown by LP-MOVPE 42
A. Łozińska, M. Badura, K. Bielak, B. Ściana, M. Tlaczała

Optical measurement in plasma microreactor 47
T. Matusiak, L. Golonka

Photophysical properties of dispersions of Zn-Ag-In-S-based alloyed semiconductor nanocrystals 51
S.G. Mucha, L.M. Mazur, K. Matczyszyn

Optical properties and applications of gold nanoparticles 57
K. Nadolski, P. Obstarczyk, J. Olesiak-Bańska, A. Żak, K. Matczyszyn

Applications of the charge transfer phenomenon occurring in hybrid semiconductor-metal nanosystems 62
K. Nawrot, D. Wawrzyńczyk, M. Nyk

Sol-Gel Layers in Microelectronic Applications 67
W. Nawrot, K. Malecha

Study of the etched pattern geometry change during RIE of nitrides 73
S. Owczarzak, A. Stafiniak, R. Paszkiewicz

Lab-on-chip platform for culturing and investigation of cells behavior 78
A. Podwin, D. Lizanets, W. Kubicki, P. Śniadek, R. Walczak, J. Dziuban

Numerical analysis of the influence of technology-related errors on optical parameters of two-dimensional photonic crystals 84
D. Przybylski, A. Zięba, S. Patela

Gold nanotriangles for applications in organic photovoltaics 92
N. Tarnowicz, L.K. Jagadamma, I.D.W. Samuel, K. Matczyszyn

Thermoelectric properties of semiconductor thin films obtained by magnetron sputtering 99
M. Turkiewicz, W. Wasyluk, D. Nowak

IP-Dip-based 3D Photonic Crystal Structure for Photonic Devices 108
P. Urbancová, A. Kuzma, D. Pudiš, P. Gašo, M. Goraus, J. Chovan

Simulation of near field exposition in UV lithography 114
A. Zawadzka, K. Indykiewicz, R. Paszkiewicz

Introduction

The 2018 International Students and Young Scientists Workshop "Optoelectronics and Microsystems Packaging" brought together students, PhD students, experienced scientists and experts interested and working in novel technologies within the field of optoelectronics, telecommunications, photonics and microsystems packaging. This event was a perfect platform for information and experience exchange and an excellent opportunity for the first presentation for many student participants.

The Workshop, organized by Technische Universität Dresden and Faculty of Microsystem Electronics and Photonics of Wrocław University of Science and Technology, was the 19th event in this series. The tradition of the Workshop goes back onto the collaboration in the field of photonics and scientific exchange between Technische Universität Dresden and Wrocław University of Science and Technology.

7 invited talks and 25 presentations were presented during the Workshop. The subjects of the presentations covered topics such as novel applications of microsystems, photonics, sensors, computer simulations, thin film characterization and microelectronic technology. Among the participants of the Workshop were representatives of Nanores Company and presented several topics connected with nanotechnology and photonics. The Workshop brought together 35 participants.

The book contains paper submissions of contributions presented by the participants during the Workshop and reviewed by the Scientific Committee. The organizing Committee would like to take the opportunity to thank all participants for high scientific level of their presentations and contributions.

Members of the Organizing Committee

Hybrid materials having plasmonic and photochromic unit

D. Benkowska[1*], E. Barrez[2], G. Laurent[2]

[1]Faculty of Chemistry, Wrocław University of Science and Technology, Wrocław, Poland
[2]PPSM Lab, Ecole Normale Superieur Paris-Saclay, Cachan, France
e-mail: dominika.benkowska@pwr.edu.pl

Abstract: In recent years, molecular photoswitches have drawn attention as active elements in electronic devices. The idea of coupling the photochromic unit with the plasmonic unit is promising because it offers time and space control. It was shown that such hybrid materials could be used to induce a switch of the molecular conductance by light excitation. In the present work, the formation and experimental results of hybrid systems showing coupling between photochromic and plasmonic units were presented. Many photochromic compounds have been studied but the diarylethene (DAE) molecules were chosen since they present great bistability, thermal stability and high fatigue resistance. Samples of gold nanorods (GNRs) with different aspect ratios were used to highlight the overlap needed between absorption spectra of DAE closed-form and the resonance band of gold nanoparticle. Modification of light-sensitive material properties was studied to see how interactions between the DAE and GNRs can be optimized.

Keywords: photonics, plasmonics, photochromism

1. INTRODUCTION

For several years, the unique properties of nanoparticles (NPs) compared to the bulk materials constitute a large ongoing research field. They can be classified into varieties of groups based on different parameters such as material, size and shape. Metal nanostructures can be distinguished because of their chemical reactivity and catalytic activity [1]. Among all metallic nanoparticles, noble metal nanostructures have received considerable attention due to their many potential biomedical applications. The mostly used and extensively studied are silver and gold nanoparticles because of their properties, which include excellent biocompatibility, electrical conductivity [2], thermal stability and optical resonance in the visible range. Herein, gold nanoparticles were examined owning to their high stability against surface oxidation over time [3], quick preparation of size controllable colloidal gold, strongly enhanced and tunable optical properties [4]. Additionally, they are able to transform energy of incident light into collective oscillation of the surface electrons, which is known as the localized surface plasmon resonance (LSPR). This resonant interaction causes enhancement of a local electric field and rise in absorption bands. The differences between the LSPR coupling of metallic nanostructures and individual constitutes play major role in nanoplasmonic [5].The coupling of the incident radiation to the metal surface can be used to modify light–matter interactions [6]. According to their outstanding plasmonic properties, gold nanoparticles (GNPs)are very promising in coupling with photochromic compounds. Among the varietyof possible molecular photoswitches, photochromic molecules show many advantages based on the reversible modification of their chemical structure under light irradiation. Many photochromic compounds have been studied but the diarylethene (DAE) molecules are particularly interesting since they present a high fatigue resistance. It was shown that coupling photochromic unit with plasmonic unit result in

modulations of photophysical properties such as shift or modification of the surface plasmon resonance (SPR) under light irradiation [7], irreversibility of the photochromic reaction [8] or improvement of the photoswitching efficiency [9]. Therefore the idea of coupling photochromic unit with plasmonic unit is very interesting and for example Feringa and co-workers showed that such hybrid materials could be used to induce a switch of the molecular conductance by light excitation. Thus the DAE derivatives can be used as active elements in electronic devices due to their great bistability [10].

In the present work, the formation and properties of hybrid GNPs-DAE materials were investigated. Gold nanorods (GNRs) with different aspect ratios were used to highlight the overlap needed between the photochromic and the plasmonic unit to enhance the cross-talking interactions. GNRs were deposited on a glass substrate and covered by a layer of photochromic compound by drop casting method. Modification of light-sensitive material properties was studied by absorption and continuous photolysis spectroscopy to see how to optimize the interaction between the photochromic and the plasmonic units.

2. MATERIALS AND METHOD

For the aim of this work 1,2-bis(2,4-dilethyl-5-phenyl-3-thienyl)-3,3,4,4,5,5-hexafluoro-1-cyclopenten, which is commercially available at Tokyo Chemical Industry as B2629, was used as the photochromic unit. The isomers of B2629 can be recognized by color due to significant differences in their absorption spectrum (Fig.1a). The irradiation upon UV light at 313 nm results with photocyclization, which indicates generation closed- form of B2629, whereas irradiation upon Vis light at 543 nm leads to back reaction, which causes an occurring open form of B2629. In the meantime, synthesis of different aspect ratios GNRs were performed by using the seed mediated method (Fig.1b) [11].

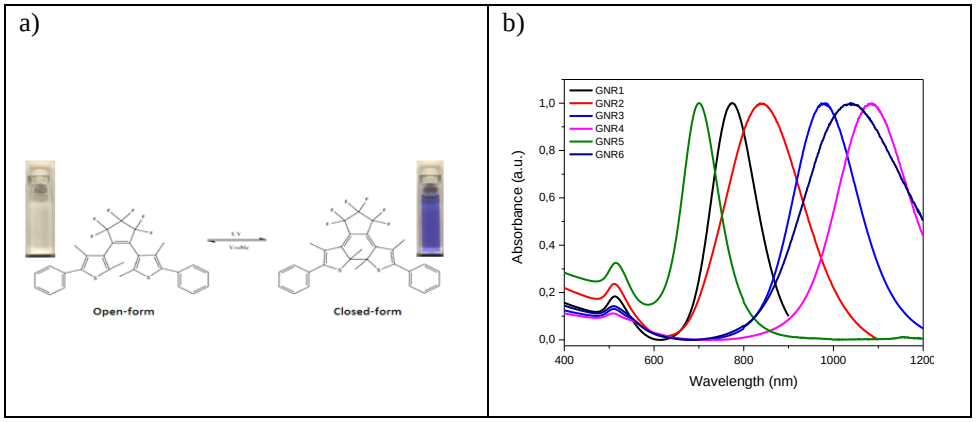

Fig. 1. (a) Schematic illustration of color changes, chemical structure and photoisomerization of B2629 (b) Normalized absorbance of gold nanorods with different aspect ratios

Hybrid materials were prepared by drop casting method on the micro slides, which were previously purified as follows: the glass substrate was washed in anhydrous ethanol for 10 min and completely dried. Additionally, the surface of glass was functionalized by solution of 3-aminopropyltriethoxysilane diluted in water. Then, solution of GNRs was dispersed on the prepared slide and after that the solution of B2629 was deposited on the top of the dried sample.

3. EXPERIMENTAL RESULTS

The kinetics of photo-induced reactions and the effect of GNPs on photochromic properties were determined by steady-state absorption spectroscopy (Fig.2.), which provides taking absorption spectra with continuously irradiation under increasing time. The cyclization and the cycloreversion reactions were performed on a sample with GNRs and without GNRs. It was reported that conversion from colourless to coloured form of B2629 in both cases has quite similar kinetics whether we consider the sample with or without GNRs. Thus there is no clear modulation of the photochromic reaction when irradiating at 313 nm. After irradiation at 543 nm, substantially faster reaction occurred in a sample with GNRs. In this case it was demonstrated that the kinetic of the back reaction increases due to the excitation at 543 nm, which affect both the photochromic and the plasmonic unit. The same tendency was observed for each synthesized population of GNRs.

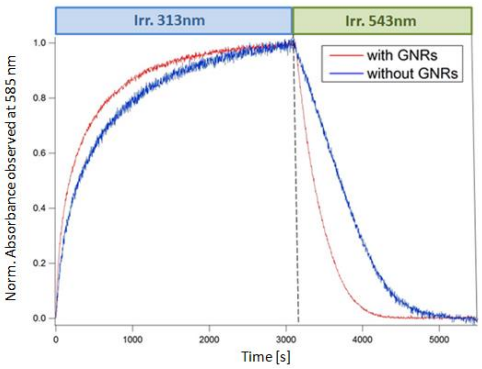

Fig. 2. Time profile of normalized absorbance at 586 nm for sample without GNRs (blue) and sample with GNR6 (red line) deposited on glass substrate and under continuous irradiation at 313 nm and at 543 nm

Furthermore, the study of photodegradation efficiency of photoinduced reactions in photochromic films with and without GNRs was investigated (Fig.3). After the first cycle the efficiency of photoinduced conversion from closed to open form, and from open to closed form, was the same. Then, the gradual decrease of cyclization process with regard to cycloreversion for the sample with GNRs was observed. The GNRs have some clear effect on the fatigue resistance of the photochromic film but this effect is relatively small (less than 10%) and can be avoided for the kinetic study of the photochromic reactions.

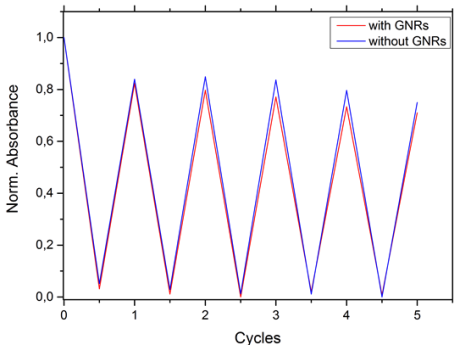

Fig. 3. The dependence of normalized absorption intensity on the number of cycles in sample of B2629 in solid state with GNR2 (red line) and without GNRs (blue line) at 586 nm

4. CONCLUSION

In this research, hybrid organic/metallic materials were performed by deposition GNRs on glass substrate and covered by layer of B2629 in closed-form by drop casting method. The photochromic process of the diarylethene derivative in systems having plasmonic and photochromic unit was examined and confirmed on a thin film. According to absorption spectra of hybrid materials, the GNRs insertions consequence is an increase of the kinetic of cycloreversion process. Moreover, reversible spectra modifications under alternate UV-Vis irradiation validated a high fatigue resistance of hybrid materials.

Acknowledgement

DB thanks to prof. Katarzyna Matczyszyn for help, support and many useful suggestions.

References

[1] S. Khatua, M. Orrit, Probing, *Sensing, and Fluorescence Enhancement with Single Gold*, J. Phys. Chem. Lett., 5 (17), pp 3000–3006 (2014)

[2] F.S. Rosarin, S. Mirunalini, *Nobel Metallic Nanoparticles with Novel Biomedical Propertie*, J. Bioanal. Biomed., 3, 085-091 (2011)

[3] M.C. Daniel, D. Astruc, *Gold Nanoparticles: Assembly, Supramolecular Chemistry, Quantum-Size-Related Properties, and Applications toward Biology, Catalysis, and Nanotechnology*, Chem. Rev., 104, 293−346 (2004)

[4] X. Huang, M. El-Sayed, *Gold nanoparticles: Optical properties and implementations*, J. of Adv. Re. 1, 13–28 (2010)

[5] I. Jung, M. Kim, M. Kwak , G. Kim, M. Jang, S. Kim S., et al., *Surface plasmon resonance extension through two-block metal-conducting polymer nanorods*., Nat. Commun., 9, 1010 (2018)

[6] G. Laurent, F. Morel, T. Asahi, K. Nakatani, R. Métivier, *Photoswitchable hybrid nanosystems based on diarylethene molecules and gold nanoparticles*. In: Y.Yokoyama, K. Nakatani, *Photon-Working Switches*, Springer, Tokyo (2017)

[7] H. Nishi, T. Asahi, S. Kobatake, *Enhanced One-Photon Cycloreversion Reaction of Diarylethenes near Individual Gold Nanoparticles.,* J. Phys. Chem. C 115, 4564-70 (2011)

[8] T. Kudernac, S.J. Molen, B.J. Wees, B.L. Feringa, *Uni- and bi-directional light-induced switching of diarylethenes on gold*., Chem. Commun. 34, 3597 (2006)

[9] H. Nishi, T. Asahi, S. Kobatake, *Plasmonic enhancement of gold nanoparticles on photocycloreversion reaction of diarylethene derivatives depending on particle size, distance from the particle surface, and irradiation wavelength.*, Phys. Chem., 14, 4898 (2012)

[10] A.Kronemeijer, H.Akkerman, H. B., Kudernac, B. Feringa, et. al., *Reversible Conductance Switching in Molecular Devices,* Adv. Mat.20, 8, 1467 (2008)

[11] X. Ye, Y. Gao, J. Chen, D. Reifsnyder, Ch. Zheng, Ch. Murray, *Seeded Growth of Monodisperse Gold Nanorods Using Bromide-Free Surfactant Mixtures,* Nano Lett., 13 (5), 2163–217 (2013)

BRIEF INTRODUCTION TO DEEP LEVEL TRANSIENT SPECTROSCOPY

M. Glinkowski*, B. Paszkiewicz, R. Paszkiewicz

Faculty of Microsystem Electronics and Photonics, Wrocław University of Science and Technology, Janiszewskiego 11/17, 50-372 Wrocław, Poland
*e-mail: mateusz.glinkowski@pwr.edu.pl

Abstract: *Deep Level Transient Spectroscopy DLTS belong to capacitance transient thermal scanning method used for observing deep impurities and defect states in semiconductor* [1]. *Deep levels introduced near the middle of the energy gap by strong localized imperfections* [2], *are probably the main reason for impair the properties of High Electron Mobility Transistors (HEMT): gate-lag, drain-lag and virtual gate. DLTS method allows finding non-radiative recombination point defects in semiconductors, which could influence the carrier properties between the areas below the gate electrode and drain electrode. DLTS method gives the information about the energy level, concentration, thermal emission rate and the capture cross section of each trap. This technique cooperate quite well with luminescence, which allows observing shallow centers localized near the edge of valance or conduction band. In this paper will presented, the fundamental physical description of transition process in semiconductor, the basic results of DLTS measurements and the conclusions.*

Keywords: DLTS, point defect, HEMT

1. INTRODUCTION

Defects have influence at properties of many semiconductor devices; these introduced intentionally called impurities are inherent part in semiconductor devices fabrication and these existing in semiconductor material are frequently responsible for many parasite effects, such as the gate-lag, drain-lag, current collapse, current suppression, negative differential resistance and kink effect. For the main reason of this negative phenomena's very often imputes traps of carriers at surface or in bulk [3]. In the following chapters will be present, the fundamental physical description of transition process in semiconductor. The basic comparison of DLTS measurements at intentionally doped BSX61 switching transistor BSX61 with BC211 low power transistor and the conclusion.

2. TRANSITION PROCESS

Defect states existing in semiconductor materials are localize inside the forbidden gap, impurities like donor or acceptors, are shallow defects, they lie near the edge of the valence and of the conduction bands. On the other hand, deep defects are localize at the middle of the forbidden gap. Deep defects are atoms that lie at interstitial position they cannot replace lattice atoms in semiconductor materials. Figure 1. (left) presented a deep defect in the silicon crystalline lattice. Au atoms interact with nearest silicon atoms and with the free electrons. The probability of capture free electron by deep defect are much higher than his recombination directly to the valence band. To the main transition process should be taken into account; the electron emission g_e the electron capture k_e the hole emission g_h and the hole capture k_h by Au atoms, presented in Figure 1. (right) as the band diagram. The trap

level with energy E_T is localize near the middle of the forbidden gap. The conduction band E_c with free electrons lie above the trap level and the valence band E_V with valence electrons lie under the trap level.

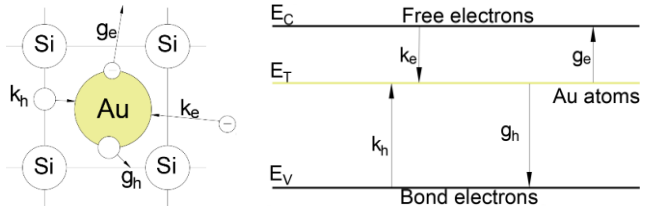

Fig. 1. The deep interstitial gold defect inside silicon lattice (left). The simplified band diagram of transitions: the electron emission g_e the electron capture k_e the hole emission g_h and the hole capture k_h (right)

The probability of capture an electron from the conduction band by deep defect in function of time is [4]:

$$k_e = \sigma_n v_n N_C \gamma \exp\left(-\frac{E_c - E_T}{k_B T}\right) \tag{1}$$

Comparing the kinetic energies and treating the electrons like particles with three degrees of freedom, the thermal velocity of electrons in function of temperature could be obtain [5, 6]:

$$\frac{1}{2} m v_e^2 = \frac{3}{2} k_B T \rightarrow v_e \sim \sqrt{T} \tag{2}$$

Assuming that all free electrons are localize near the conduction band the effective density of states [7] in function of temperature is:

$$N_c = 2\left(\frac{2\pi m_n k_B T}{(2\pi\hbar)^2}\right)^{\frac{3}{2}} \rightarrow N_c \sim T^{\frac{3}{2}} \tag{3}$$

Capture cross section for electrons σ_n and the degeneracy factor γ also changes with temperature, the equation (1) looks now:

$$k_e = \sigma_n(T)\, T^2 A \exp\left(-\frac{\Delta E}{k_B T}\right) \tag{4}$$

where: A is constant that not change with the temperature.

3. EXPERIMENTAL RESULTS

Emission rate is the time needed to achieve thermal equilibrium by carriers that intentionally have been introduce to non-equilibrium state. To determine the emission rate of the trap levels in test switching transistor BSX61 it is essential to provide non-equilibrium condition by "injected pulse" V_F that inject the carriers into the depleted region. Next applying the reverse bias V_R to measure the difference between the capacitance of base-emitter junction BSX61 switching transistor C and compensated capacitance C_0, $\Delta C = C - C_o$, presented at Figure 2. After the injected pulse, the width of the depleted region will decrease and majority carriers starts to diffuse, in results the capacitance of depleted region will change.

Under the reverse bias the width of the barriers increase and only the generation and minority carrier's current will occurs. The system will back to the equilibrium state before the next injected pulse the capacitance in depleted region will return to the initial value. The time for measuring the capacitance i.e. the time for applying the reverse bias is set for 200 ms and the time for injected pulse is set to 1 ms.

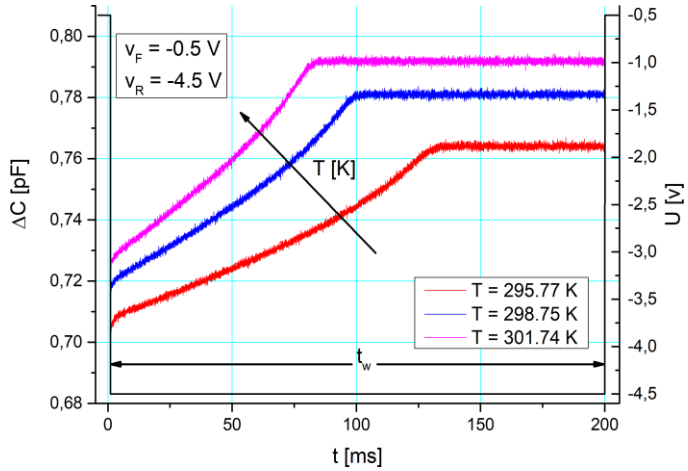

Fig. 2. Capacitance and applied voltage of base-emitter junction in BSX61 switching transistor for three different temperatures. Reverse voltage was applied for $t_w = 200$ ms

The capacitance transient are measured for wide range of temperatures and using the lock-in method (equation 5) DLTS signal presented at Figure 5 could be obtain:

$$S_{DLTS} = \int_{t'}^{2t'} \Delta C dt - \int_{0}^{t'} \Delta C dt \,;\; t' = \frac{t_w}{2} \tag{5}$$

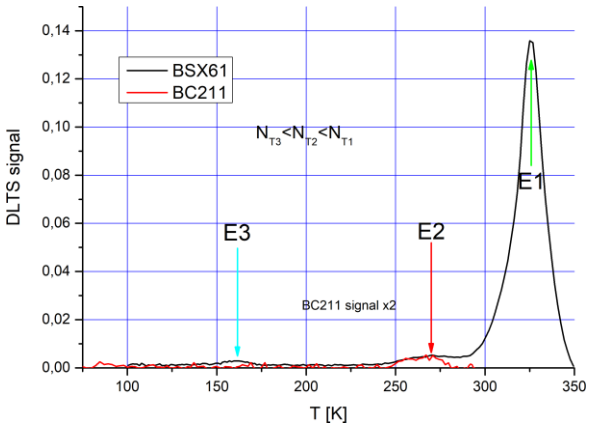

Fig. 3. DLTS signal for Si: BSX61 switching transistor (black) and Si: BC211 low power transistor (red), window width $t_w = 200$ ms. DLTS signal for BC211 was multiplied by 2

At Figure 3., three kinds of traps in BSX61 switching transistor are observe. The intensity of DLTS signal corresponds to trap concentration. The first trap level is active in temperatures from 150 K to 170 K the second trap level is active from 250 K to 370 K and the third from 300 K to 360 K. To determine the trap energies and the capture cross sections the inverted Laplace transform (equation 6) for each transients have to be involve.

$$f(t) = \int_0^\infty F(s)\exp(-st)dt \tag{6}$$

In result, receive the spectrum of exponents and peaks corresponds to the emission rate of carriers from different trap levels (Figure 4).

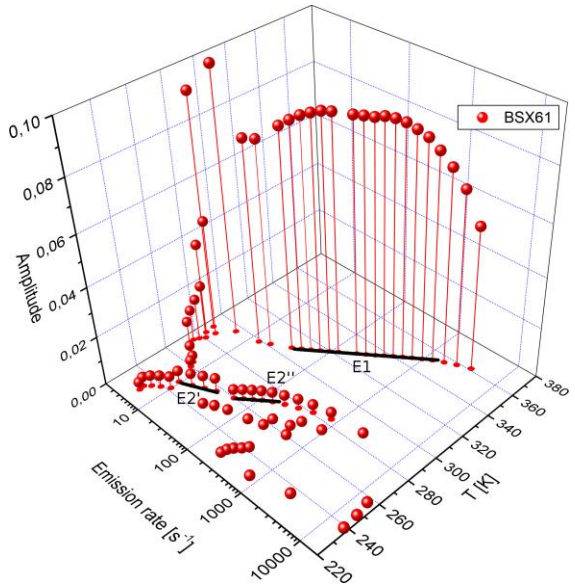

Fig. 4. Amplitude and emission rate following the Laplace transform applied to capacitance transients in wide range of temperatures. Three traps levels are observe E1 in temperature range from 300 K to 360 K temperatures and E2' with E2'' in temperature range from 220 K to 260K

Rewriting, the equation (4) in the straight-line form $y = ax + b$ the basic quantities could be obtain.

$$\ln\frac{g_n}{T^2} = -\Delta E\frac{1}{k_B T} + \ln\eta\sigma_n \tag{7}$$

The slope of the curve is equal to energy of the trap level and the intercept respond for the capture cross section. The Arrhenius plot for the first deep trap is present at Figure 5.

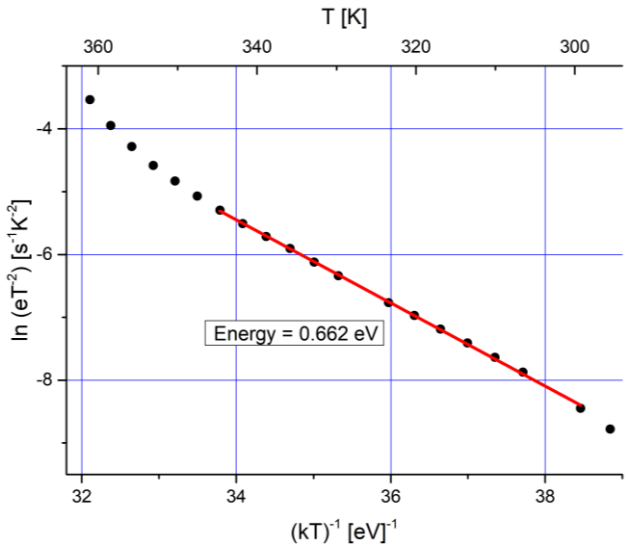

Fig. 5. Arrhenius plot of the first defect (equation 7) in switching transistor Si: BSX61, the curve determined by linear combination of emission rate peaks obtained from inverted Laplace algorithm

4. CONCLUSIONS

In this paper was present the basic physical and experimental concept of the Deep Level Transients Spectroscopy to determining deep defects in semiconductor materials. The measurements was make at the switching transistor BSX61 and BC211 low power transistor. From the data presented at Figure 5, the energy of E1 defects could be estimate. The E1 deep defect lies 0.662 eV below the conduction band. Energy equal to 0.662 eV match very well with the Mn atoms from the literature [8]. The deep traps in intentionally doped BSX61 switching transistor was detect by Laplace DLTS system are responsible for reducing the minority carrier lifetime in base, thereby for reducing the storage time. Non-doped BC211 low power transistor possess very low concentration of deep defects undetectable by typical Laplace a DLTS measurements.

Acknowledgement

This work was co-financed by the National Centre for Research and Development grants TECHMATSTRATEG No.1/346922/4/NCBR/2017, the National Science Centre grant No. DEC-2015/19/B/ST7/02494, Wroclaw University of Technology statutory grants and by the Slovak-Polish International Cooperation Program. This work was accomplished thanks to the product indicators and result indicators achieved within the projects co-financed by the European Union within the European Regional Development Fund, through a grant from the Innovative Economy (POIG.01.01.02-00-008/08-05) and by the National Centre for Research and Development through the Applied Research Program Grant No. 178782 and Grant LIDER No. 027/533/L-5/13/NCBR/2014.

References

[1] D. V Lang, “Deep-level transient spectroscopy : A new method to characterize traps in semiconductors Deep-level transient spectroscopy : A new method to characterize traps in semiconductors,” vol. 3023, no. 1974, 1974.
[2] J. Bourgoin and M. Lannoo, Point Defects in Semiconductors II : Experimental Aspects. Springer Berlin Heidelberg, 1983.
[3] W. Janke and W. Wojtasiak, “Właściwości i zastosowania tranzystorów HEMT na bazie azotku galu,” Prz. Elektrotechniczny, vol. 91, no. 9, pp. 65–73, 2015.
[4] Б. Ж. Ланно М, Точечные дефекты в полупроводниках. МОСКВА, 1985.
[5] D. Halliday, R. Resnick, and J. Walker, Podstawy Fizyki 1. Wydawnictwo Naukowe PWN, 2007.
[6] D. Halliday, R. Resnick, and J. Walker, Podstawy Fizyki 3. Wydawnictwo Naukowe PWN, 2006.
[7] В. Л. Бонч-Бруевич and С. Г. Калашников, Физика Полупроводников.
[8] R. F. Pierret and G. W. Neudeck, “Advanced Semiconductor Fundamentals,” Pearson Educ. Inc., vol. 6, pp. 17–18, 1987.

DEPLOSCOPE – A MODULAR DEPLOYABLE CUBESAT TELESCOPE

A. Graja[1], M. Ćwikła[2], P. Kwapisz[2]

[1]Faculty of Microsystem Electronics and Photonics, Wrocław University of Science and Technology, Janiszewskiego 11/17, 50-372 Wrocław, Poland
e-mail: adrianna.graja@pwr.edu.pl
[2]Faculty of Mechanical Engineering, Wrocław University of Science and Technology, Wybrzeze Wyspianskiego 27, 50-370 Wroclaw, Poland
e-mail: michal.cwikla@pwr.edu.pl
e-mail: 222764@student.pwr.edu.pl

Abstract: *The acquisition of detailed Earth images plays a crucial role in the fields of environmental protection, precision farming, monitoring of natural disasters and security. That kind of high-resolution data is related to utilization of high-volume telescopes with essential parameters, for instance large aperture and focal length of the optic system. The costs of fabricating and launching of those telescopes are enormous and cause the increase in overall price of the images, limited availability and prolonged revisit time for the chosen observation field. This article presents a conceptual geometric design of the modular telescope, possible to be implemented in a relatively small nanosatellite structures. Splitting the optical construction into particular segments provides an opportunity to fit the whole telescope system in the compact and standardized volume of CubeSat, with a significant savings of costs, volume and mass. A special attention in this work has been given to geometry implementation and deployment mechanism for the Cassegrain topology - a crucial segment of the mirrors configuration.*

Keywords: optics, nanosatellites, telescope, geometrical optics, simulation

1. INTRODUCTION

Nowadays, Earth Observation (EO) satellites with huge telescopes onboard provide high-resolution images and allow to distinguish two objects located on Earth at a distance of fewer than 0.5 m from each other [1]. Such high-quality image requirements result in huge volume and mass of the instruments, notably increasing the costs of their launch and fabrication. The goal of this article is to present a conceptual design of a synthetic aperture telescope [2], which may meet similar resolutions as current state-of-the-art Earth observation systems, but simultaneously, having a significantly smaller launch volume. It is assumed that in the future it will be possible to create a constellation of small, light and inexpensive Earth-observing nanosatellites, utilizing the solution proposed in this article. The greater number of devices results in a shorter time of revisit above a specific place, which may lead to the precise imaging of a chosen area in real-time. The main application of the telescope concept presented in this article is to monitor Earth phenomena, e.g. natural disasters. Therefore, the key criterions during the design process were to achieve a sufficient resolution and possibly the widest field of view. Additionally, it was attempted to obtain the smallest possible volume of the structure and dimensions corresponding with the CubeSat standard, in which the basic unit is 1 U = 100x100x100 [mm]. It is assumed that the overall dimensions of the stowed telescope module in the nanosatellite structure should

not exceed 5 U. The 2 U are reserved for the CubeSat bus which contains modules, such as: On Board Computer (OBC), Communication Module (CM), Electrical Power System (EPS), Attitude Determination and Control System (ADCS) – necessary for proper device operation on the orbit. The next 2 U or 3 U are intended for the telescope instrument topology. It is allowed to place part of the telescopic system in the nanosatellite bus structure.

2. CONCEPT DESIGN

2.1. Optical system topology

Two main types of the telescope optical systems have been taken into consideration – Gregorian and Cassegrain [3]. The Gregorian telescope includes two concave mirrors. The Cassegrain is characterized by a concave primary mirror and convex secondary mirror distributed in a smaller distance relative to each other. It results in a more compact overall volume of the whole instrument. To meet set requirements, the utilization of one of the Three Mirror Anastigmat (TMA) group designs, based on Cassegrain solution, was suggested [4]. TMA consists of three mirrors: primary mirror (PM), secondary mirror (SM) and tertiary mirror (TM). The proposed configuration overcomes problems with aberrations and narrow field of view. Two different solutions of TMA: Full-field Korsch and Annular Korsch are presented in figure 1 [5].

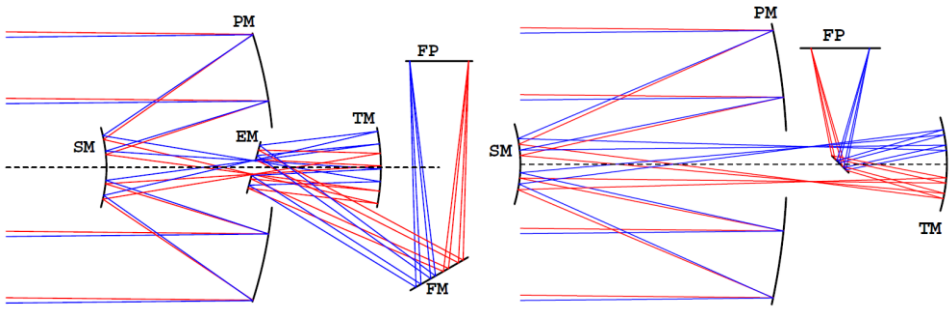

Fig. 1. Full-field Korsch (left) with additional angled extraction mirror (EM) and flat folding mirror (FM) and Annular Field Korsch (right) [5]

Despite the fact that Full-field Korsch has is characterized by far more complex structure comparing to Annular, it also has also some significant advantages. The Full-field provides nearly telecentric rays focusing on the detector, which means that the size of the image does not change when defocusing the detector [4]. Additionally, this optical system is more insensitive to distortions and provides lower numerical aperture, thus smaller distance between primary and secondary mirrors. Due to those aspects, Full-field Korsch is the most suitable solution for our requirements [2]. However, all presented concept designs assume utilization of monolithic primary mirror, which results in a significant increase in the overall pre-launched volume of the instrument. The idea is to use a few smaller mirror segments instead of one circular primary mirror. During the launch of the satellite, segments are being

folded along the height of the instrument and then, unfolded after reaching the Earth's orbit. This solution results in considerable costs savings and provides the possibility to transport a telescope in the CubeSat. Combining Full-field Korsch design with an idea of segmenting primary mirror leads to the configuration is known as Fizeau Synthetic Aperture (Fig. 2) [2].

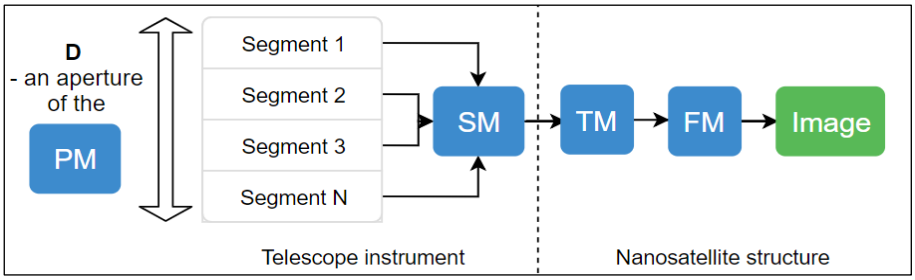

Fig. 2. Scheme of the Fizeau Synthetic Aperture, composed of: primary mirror (PM), secondary mirror (SM), tertiary mirror (TM), angled extraction mirror (EM) and flat folding mirror (FM)

Performance of the optical system for different spatial frequencies is expressed by MTF - Modulation Transfer Function. The highest and the best value of this parameter corresponds to the monolithic primary mirror [2]. While choosing the number of arms for the Fizeau Synthetic Aperture configuration, following aspects has been taken into account. Firstly, reducing the mass of the optical system while maintaining a satisfactory value of the MTF parameter. On the other hand, small complexity of the system and adjustment to the CubeSat structure standard. In the result, based on an overview of the image quality for different numbers of arms described in the reference literature [2], configuration composed of four segments was selected.

2.2. Geometrical optics calculations

Resolution of telescopes refers to the parameter called Ground Sample Distance (*GSD*) [3]. Eqn. (1) shows the Rayleigh criterion [2], which defines the minimum diameter of the primary mirror aperture (*D*) required to observe objects separated from each other by a specific distance (*GSD*). Farther, *h* variable expresses chosen orbit, thus distance from the telescope to a surface of the Earth, and λ is a specific wavelength. A limitation is caused by the diffraction nature of light.

$$D = 1.22\frac{h\lambda}{GSD} \tag{1}$$

Due to restrictions in terms of overall instrument volume and taking into account potential application aspects of our conceptual design, *GSD* value of 1 m was posited. The device is considered to be working on LEO (Low-Earth-Orbit) at the distance of about 500 km (*h*). Measuring range of the detector should correspond to the visible spectrum of light, therefore for the calculations, the wavelength (λ) of 700 nm has been selected. Due to the use of segmented primary mirror instead of monolithic one, 10 % margin has to be placed on a calculated value [2]. Finally, the calculated diameter of the entrance aperture (*D*) should be at least 470 mm.

Next critical factor is the geometry of the three nonplanar mirrors creating the TMA configuration. In every spherical optical element, a phenomenon called spherical aberration occurs. When parallel incident rays (propagating in different distances from the optical axis) reflect from the surface of the spherical element, they end up focusing at different spots. In the case of telescopic design, this type of aberration has a significant influence on image resolution, clarity and depth of focus [6]. Spherical aberration correction is realized by utilizing the geometrically complex optical elements. In the case presented in the article, aspherical conical mirrors have been taken under consideration. The geometry of such optical element is described by Eqn. (2) and depends on the paraxial radius of curvature (*c*) and conic constant (*k*) [2, 7].

$$z = \frac{cr^2}{1 + \sqrt{1 - (1 + k)c^2r^2}} \tag{2}$$

2.3. Image formation

A principle of lateral magnification was utilized to determine the relation between the focal length of the optical system and the size of the image recorded by the detector [8]. In the case of telescopic design, we can write down the equation in the following form [2]:

$$\frac{px}{f} = \frac{GSD}{h} \tag{3}$$

A size of the pixels is determined by the type of detector's matrix provided by a specific manufacturer. For our design, we assumed detector CCD in CMOS from *Imec* with a pixel size (*px)* of 5.4 μm [9]. After defining *GSD* and *h*, as respectively 1 m and 500 km, the focal length of the optical system (*f*) was 2700 mm.

2.4. Geometrical optics simulation and structure visualization

Previous calculations and assumptions led to the creation of the optical system model, which included the geometry of the mirrors and distance relations between them. Utilizing the *Ray Optics Module of Comsol Multiphysics* software, simulations of rays propagation from the object on Earth to the matrix of the detector was carried out (Fig. 3, left). Earth-Orbit distance of 500 km (*h*) and the maximum ground surface distance of 1 m (*GSD*) has been considered. Incident rays were propagated with the 1 μrad angle to Y-axis. The simulation was made for central VIS wavelength of 550 nm. Since the rays were propagating symmetrically to the axis of optical system, the spatial optical system was brought to 2D plane and the monolithic aspherical primary mirror (*M1*) instead of segmented ones has been designed. The final volume of the deployed instrument, was 470x470x550 [mm] (respectively depth/width/height) and it met defined requirements.
In the next step, utilizing the *Autodesk Inventor* software, geometrical model of the whole satellite structure was made (Fig. 3, right). Model includes i.a. 2U CubeSat bus with solar panels (*SP*); CCD detector matrix; a black baffle, an obstruction for the scattered light rays (*BB*); four arms of segmented primary mirror (*M1*) and platform with secondary mirror (*M2*).

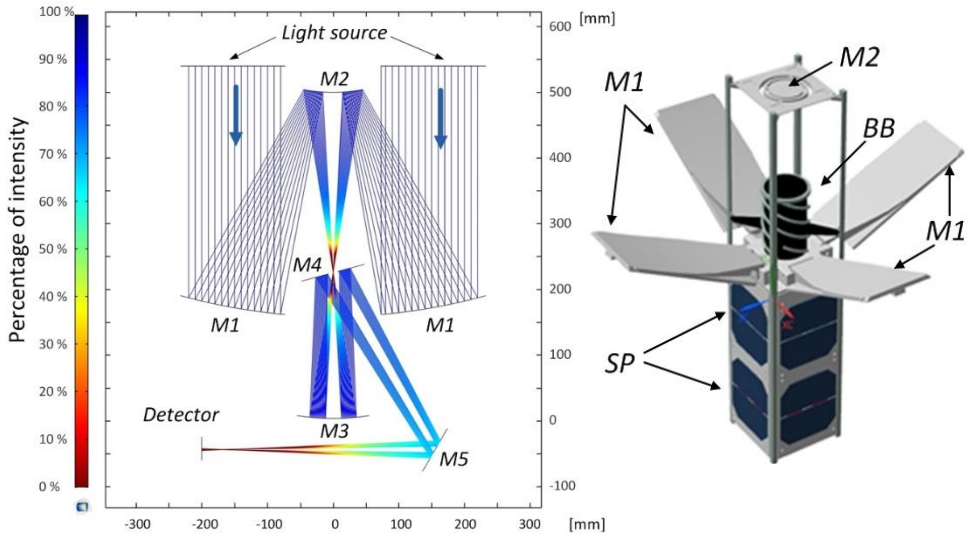

Fig. 3. The modular deployable CubeSat telescope: simulation of rays trajectories and optical intensity in the optical system (left) and mechanical design of the construction (right)

During the launch of the satellite, segments are being folded along the height of the instrument and then unfolded after reaching the Earth's orbit. It should be mentioned that secondary mirror (*M2*) can be mounted in the traveling stage, therefore extending *M1* to *M2* distance and overall focal length of the instrument. Thereafter, intensity distribution over focal plane (*Detector*) has been plotted out (Fig. 4).

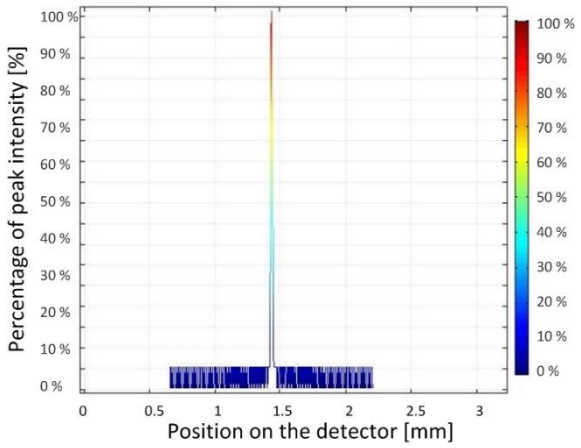

Fig. 4. Percentage intensity distribution in the focal plane of the telescope (*Detector*)

It turned out that aproximatelly 60 % of source energy can be considered as noise and stands for low intensity on the surface (less then 7 % of peak intensity). Thus, only 40 % of the source rays stands for peak intensity. Improvement of overall performance can be made by

utilizing narrow-band filter to eliminate majority of non-focused light or reducing spherical aberration phenomenon by redesigning the mirror's geometry or utilizing an adaptive optics [10-11]. Due to the Nyquist criterium, the diameter of light beam focused on the detector's plane should correspond to twice pixel size (in this case 2 x pixel size = 11 μm) [2]. Since the peak intensity distribution is close to Gaussian distribution we used FWHM to measure the diameter of the focused beam and we achieve the result of 18.5 μm, therefore the value was close to our expectations.

3. CONCLUSION

In the article, the realization attempt of the synthetic aperture telescope in the CubeSat structure, providing a high-resolution feature, was presented. The geometrical requirements for the overall structure were met. In the optical simulations spot beam diameter of 18.5 μm has been achieved and it was close to requirements. However, only 40 % of the source energy was considered as usable energy. Way to improve this performance has been presented. It should be taken into account that even a perfect project or simulation do not guarantee enough performance in a harsh and unpredictable space environment. Therefore, the further work should focus on the dynamic and thermal aspects of the system. Attention should be paid to the issue of deployment of four main mirrors. Inaccuracies in their positioning could be corrected by angular manipulation of secondary mirror with precise MEMS actuators. The ability to adjusting the mirror position in 3 axes, could result in continuous wavefront correction. Moreover, the selected material for the mirrors have a significant impact on the accuracy of the system. A trade-off between durability, mass and thermal conductivity should be considered. Based on the analizys presented in reference literature [2], the SIC material could be the appriciatest.

Acknowledgements

I would like to thank my supervisor prof. Jan Dziuban, PhD, DSc for the useful discussions and helpful feedback and also my colleagues from *SatRevolution* company for ideas and huge scientific material base.

References

[1] Digital Globe - Worldview 3: *http://worldview3.digitalglobe.com*, (access 11.2018).
[2] D. Dolkens, *A Deployable Telescope for Sub-Meter Resolutions from MicroSatellite Platforms*, (2015).
[3] Joseph G., *Building Earth Observation Cameras*, CRC Press, (2015)
[4] Korsch, D., *Anastigmatic three-mirror telescope*. Appl. Opt., (1977).
[5] Lampton, M. and M. Sholl, *Comparison of On-Axis Three-Mirror Anastigmat Telescopes*, International Society for Optical Engineering, (1999).
[6] Luo Yong, *Computing Surface Parameter of Conic Aspheric Mirror with Singular Value Decomposition*, Electrical and Information College, Jinan University, Zhuhai, China (2013).
[7] *www.vikdhillon.staff.shef.ac.uk/teaching/phy217/telescopes/phy217_tel_reflectors.html*, (access 11.2018).
[8] Paul A. Tipler, Physics for Scientists and Engineers 6th edition, W. H. Freeman (2007).

[9] *www.imec-int.com/drupal/sites/default/files/2016-12/Folder%20CCD-In-CMOS%20TDI%20and%20Multispectral%20TDI%20Imaging.pdf*, (access 11.2018).

[10] Michel E. Dearborn, et al., *A Deployable Membrane Telescope Payload for CubeSats*, JoSS, Vol. 3, No. 1, pp. 253-264, (2014).

[11] J. Cheng, *The Principles of Astronomical Telescope Design*, (2009).

OPTICAL AND STRUCTURAL PROPERTIES OF AMYLOIDS OBTAINED FROM BOVINE INSULIN

M. Grelich, A. Grzesik, J. Olesiak-Bańska*

Advanced Materials Engineering and Modelling Group, Wroclaw University of Science and Technology, Wyb. Wyspianskiego 27, 50-370 Wroclaw, Poland

e-mail: joanna.olesiak@pwr.edu.pl

Abstract: *Amyloid protein aggregates prompt a challenging research interest since they refer to many pathological conditions in living beings. There are two most commonly known types of amyloids – fibrils and spherulites. Amyloid fibrils have elongated morphology and are structurally dominated by cross β-sheets running along the fiber axis. Spherulites consist of an amorphous core radially surrounded by the fibrils. Bovine insulin (BI) is often used as a model protein for amyloids formation. We obtained above-mentioned structures and investigated their structural properties using polarized light microscopy (PLM), scanning electron microscopy (SEM) and atomic force microscopy (AFM). Fluorescence and UV-Vis absorption spectroscopies were used to study optical characteristics of fibrils and spherulites. Presented results indicate that enhanced autofluorescence of amyloids constitutes a helpful assay for distinguishing them from their native protein counterpart.*

Keywords: *amyloid fibrils, spherulites, β-sheet*

1. INTRODUCTION

There is a broad class of proteins that in mildly denaturating conditions undergo misfolding into different aggregate structures, including amyloid fibrils and spherulites. Mentioned assemblies constitute a subject of intense research since they are related to some degenerative diseases, such as type II diabetes, Alzheimer's and Parkinson's disease [1, 2]. Nevertheless, some of the proteins are not associated with any illness, indicating that amyloid formation is a generic property of polypeptide chains [3].

Bovine insulin is a protein consisting of two polypeptide chains linked together by means of two disulfide bonds. The A chain comprises of 21 amino acids and the B chain – of 30 amino acids. The primary structure of bovine insulin is characterized by the presence of the following aromatic amino acids: phenylalanine (Phe) at positions B1, B24, B25, tyrosine (Tyr) at A14, A19, B16, B26 and histidine (His) at B5, B10 [4]. Bovine insulin is commonly applied as a model protein for *in vitro* investigations of amyloids formation [3, 5].

In this work, general properties of fibrils and spherulites are described. We focus on amyloids obtained from bovine insulin. Further results concern studies on their optical and structural properties. Standard physicochemical tools are used to enable the characterization and interpretation of target assemblies.

2. STRUCTURAL CHARACTERISTICS

2.1. Amyloid fibrils

Amyloid fibrils (fibers) are ordered polymeric aggregates sharing a common structural motif – intermolecular β-sheets running along the fibril axis, wherein the constituent β-strands are arranged perpendicular to the aforementioned axis. In general, these structures should be long (approximately 1 μm or more), exhibit straight, unbranched morphology, with diameters ranging from about 6 to 12 nm [2]. Each amyloid fibril is characterized by an ordinary and extraordinary refractive index, n_o and n_e, respectively [6].

Amyloid fibril formation is a complex process during which native protein rearranges into β-sheet rich structure. In fact, protein can aggregate into many structurally different fibrils. They comprise of number of protofilaments being over-twisted “threads” [2].

2.2. Spherulites

Spherulites are defined as spherical structures consisting of a central core surrounded by amyloid fibrils that are radially aligned outwards. Their diameter varies from 5 to 50 μm. When observed under a polarizing light microscope, spherulites exhibit characteristic “Maltese cross” extinction pattern indicated as a dark center surrounded by four white lobes. The core is non-birefringent and consists of irregularly arranged polypeptide chains [6, 8].

3. EXPERIMENTAL PROCEDURE

A key effect on insulin fibrillation plays pH. At pH < 2 insulin reveals a monomeric structure. In acidic conditions, the highest nucleus rate formation is at temperatures > 60 ^{o}C. Moreover, increasing concentration renders an increase in an insulin fibrillation rate. These conditions mostly favour insulin fibrillation [7].

3.1. Sample preparation

Bovine insulin purchased from Sigma Aldrich (I5500) was dissolved in HCl (pH = 1.3) at concentration 5 mg/mL. The solution was incubated in 1.5 mL eppendorf tube at 70 ^{o}C without stirring for 2 h in IKA Dry Block Heater 1.

3.2. Atomic force microscopy

40 μL of 100 times diluted samples were deposited on mica sheet for 1 minute in order to allow adsorption of amyloids on the surface. Afterwards, the sample was rinsed by Milli-Q water and dried. Studies were made on Dimension V AFM Veeco using tapping mode.

3.3. Polarized light microscopy

After incubation, a volume of 20 μL of each solution was put onto clean microscope slides. The slides, without coverslips, were observed under polarized light microscope Olympus 60 BX with crossed polarizers. A first order waveplate was inserted at 45^{0} to the polarizers. Images were taken by a digital camera.

3.4. Scanning electron microscopy

50 μL of 10 times diluted solutions were put on carbon tape, covered by Petri dish in order to let it evaporate. Imaging was done on JEOL JSM-6610LV.

4. RESULTS

Preparation of bovine insulin described in subsection 3.1 resulted in the formation of both amyloid fibrils and spherulites. After incubation, the sample was turbid and dense.

Dimensions and shape of fibrils were confirmed by AFM imaging (Fig. 1). Their length varied between 366 and 810 nm, they had from 8 to 16 nm in width and from 12 to 18 nm in height.

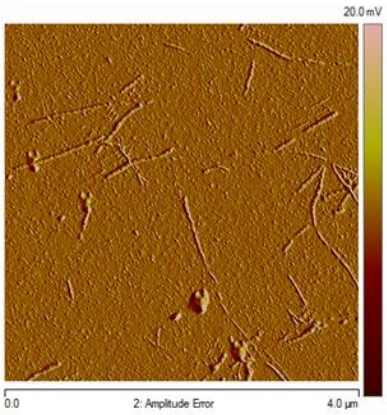

Fig. 1. AFM image of BI fibrils.

In order to confirm the presence of spherulites, the sample was viewed under PLM. The images revealed characteristic Maltese cross pattern (Fig. 2a). The dark centre confirms that the core consists of non-birefringent material. Observed spherulites presented size distribution with diameters ranging from 30 to 60 μm..

In order to investigate arrangement of amyloid fibrils forming spherulites, a first order retardation plate was inserted between the polarizer and analyzer at angle 45^0 (Fig. 2b). Two blue lobes of each spherulite reveal that their fast optical axis is aligned with the fast one of the retardation plate.

a) b)

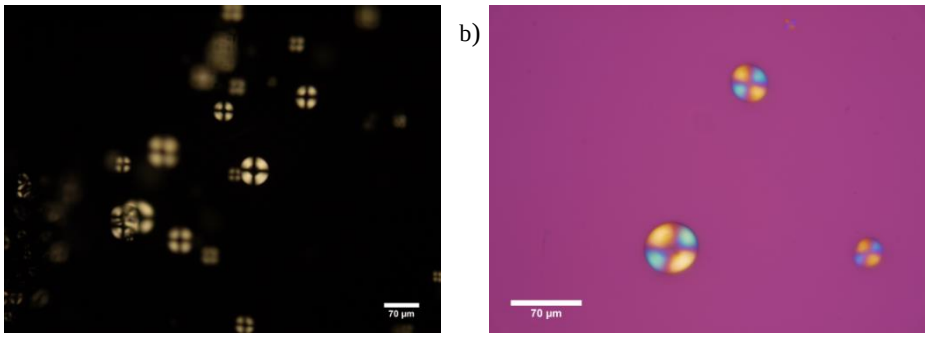

Fig. 2. Spherulites viewed under PLM (a) and after putting the first order retardation plate (b)

SEM imaging (Fig. 3) pointed out the spherical shape of structures observed under PLM. It indicated the presence of many spherulites with a rough surface and many cracks – probably due to low pressure in the chamber. Furthermore, a radial organization of fibrils within spherulites could be confirmed.

a) b)

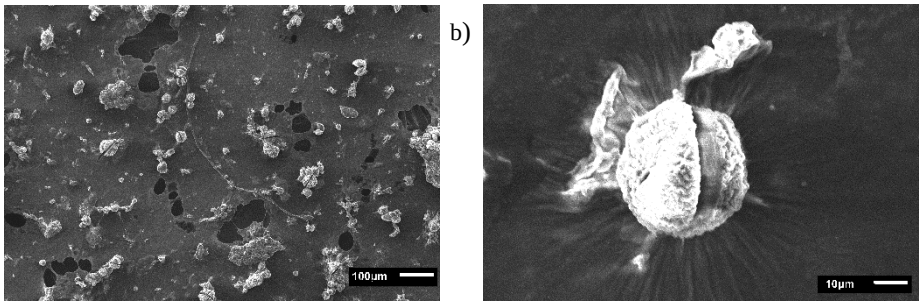

Fig. 3. Spherulites observed on SEM (a, b)

5. OPTICAL PROPERTIES

Optical properties of amyloid β-rich structures differ from those of their native protein. Hence, spectroscopic measurements can be utilized as good markers for characterization, detection and understanding of amyloids formation [9].

5.1. UV-Vis absorption

Since insulin comprises of aromatic amino acids, native protein, fibrils, and spherulites obtained from mentioned protein absorb near 280 nm at acidic conditions [5].

5.2. Autofluorescence

Native protein and amyloid aggregates of bovine insulin exhibit autofluorescence properties in the visible range [5]. However, the origin of this phenomenon is still unclear. It is obvious that intrinsic fluorescence of proteins arises from the presence of aromatic amino acids. It has been evidenced that proteins upon aggregation display enhanced autofluorescence. It is true even for peptide sequences devoid of aromatic amino acid residues. This phenomenon can be explained by extensive hydrogen bond network within structures consisting mainly of β-sheets. In such systems, probably charge delocalization is responsible for observed enhanced fluorescence emission [10, 11].

For autofluorescence measurements, 5 mg/mL BI solution in 25 mM HCl (pH = 1.6) was prepared. Emission spectra for BI native form, fibrils and spherulites were recorded for excitation wavelengths from λ_{exc} = 310 nm to λ_{exc} = 420 nm (Fig. 4) [5]. They clearly evidence that a position of emission peak is dependent on excitation wavelength, what unequivocally violates Kasha's rule. Each emission spectrum (Fig. 4 a-c) is normalized, however, the authors [5] provide information that compared to native protein, insulin fibrils and spherulites demonstrate enhanced autofluorescence.

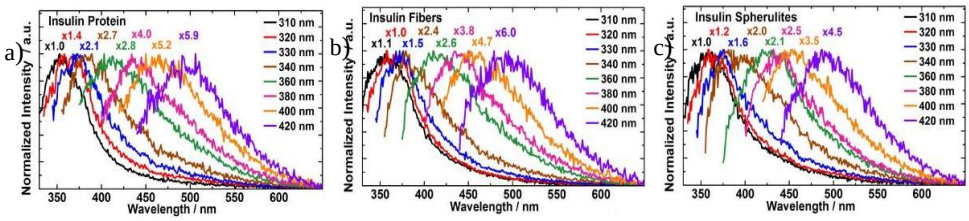

Fig. 4. Autofluorescence from BI native protein (a), fibrils (b) and spherulites (c) [5]

6. CONCLUSIONS AND CHALLENGES

Conducted studies revealed that sample preparation method described here leads to the formation of insulin fibrils and spherulites. Their presence can be underlined through many methods. Fibrils were identified by AFM. PLM gave insight into the structure of BI spherulites and confirmed non-birefringent character of their central core. Insertion of the first order retardation plate evidenced a radial arrangement of fibrils within spherulite. SEM imaging additionally helped to identify spherical structure of obtained spherulites. Observed fibrils varied in length from 366 to 810 nm, they had from 8 to 16 nm in width and from 12 to 18 nm in height. Additionally, the diameter of spherulites was in the range from 30 to 60 μm.

Presented autofluorescence spectra indicated that insulin amyloid aggregates can be noninvasively tracked since they exhibit more intensive emission than their native nonfibrillar form. Intrinsic fluorescence of proteins arises from the existence of aromatic amino acid residues. Probably, in amyloids enhanced autofluorescence is also due to a dense network of hydrogen bonds within β-sheets since it facilitates electron delocalization and the low-energy electronic transitions can occur. This method of amyloid imaging is label-free and therefore eliminates the risk of any perturbations during the aggregation of proteins. Obviously, in order to characterize amyloids in details, other techniques, including confocal fluorescence microscopy or SHG microscopy should be taken into account. Label-free imaging seems to be a good assay for identification and characterization of amyloids *in vitro*. However, still demanding challenge is to apply such assays in complex biological systems.

References

[1] V. Vetri and V. Foderà, FEBS Letters, 589, 2448–2463 (2015).
[2] S.S. Rogers, M.R.H. Krebs, E.H.C. Bromley, E. van der Linden, and A.M. Donald, Biophysical Journal, 90, 1043–1054 (2006).
[3] M.I. Smith, V. Foderà, J.S. Sharp, C.J. Roberts, and A.M. Donald, Colloids and Surfaces B: Biointerfaces, 89, 216–222 (2012).
[4] J. Brange and L. Langkjœr, Insulin Structure and Stability, in: Ed. by Y.J. Wang and R. Pearlman, Stability and Characterization of Protein and Peptide Drugs: Case Histories, Springer US, Boston, MA (1993), pp. 315–350.
[5] P.K. Johansson and P. Koelsch, Biomed Opt Express, 8, 743–756 (2017).
[6] M.I. Smith, J.S. Sharp, and C.J. Roberts, Soft Matter, 8, 3751–3755 (2012).

[7] J. Brange, L. Andersen, E.D. Laursen, G. Meyn, and E. Rasmussen, Journal of Pharmaceutical Sciences, 86, 517–525 (1997).
[8] M.R.H. Krebs, C.E. MacPhee, A.F. Miller, I.E. Dunlop, C.M. Dobson, and A.M. Donald, Proceedings of the National Academy of Sciences, 101, 14420–14424 (2004).
[9] D. Pinotsi, A.K. Buell, C.M. Dobson, G.S. Kaminski Schierle, and C.F. Kaminski, ChemBioChem, 14, 846–850 (2013).
[10] F.T.S. Chan, G.S. Kaminski Schierle, J.R. Kumita, C.W. Bertoncini, C.M. Dobson, and C.F. Kaminski, Analyst, 138, 2156–2162 (2013).
[11] D. Pinotsi, L. Grisanti, P. Mahou, R. Gebauer, C.F. Kaminski, A. Hassanali, and G.S. Kaminski Schierle, Journal of the American Chemical Society, 138, 3046–3057 (2016).

COMPARISON OF MULTILAYERED AU BASED AND AU FREE OHMIC CONTACTS TO ALGAN/GAN HETEROSTRUCTURES

G. Ilgiewicz*, W. Macherzyński, R. Paszkiewicz

Faculty of Microsystem Electronics and Phtonics, Wrocław University of Science and Technology, Janiszewskiego 11/17, 50-372 Wrocław, Poland
*e-mail: grzegorz.ilgiewicz@pwr.edu.pl

Abstract: *Typical composition of ohmic contacts to AlGaN/GaN heterostructures includes gold layer, as a metal protecting the contact from negative influence of the environment. Other role of Au is to make good connection with wire bonds that allows the current flow. But Au easily diffuse into contact metallization and into semiconductor structures especially at higher temperatures, that are needed to form the ohmic contact in Rapid Thermal Annealing (RTA) process. As a result contacts could have not fully predictable U-I characteristics or they are not linear. To protect contacts from gold atoms diffusion, special metallic layers must be used. As diffusion stopping layers usually the metals with high atomic mass, high melting point and big atomic radius are applied because these metals not diffuse as intensively as gold, and they form a barrier between gold layer and the remaining contact layers. Other way is to fabricate the Au free contacts. This solution could also allow to reduce number of metallic layers of contacts because the stopping diffusion layer is not necessary. To compare both types of contact the samples with different metallization schemes were fabricated: Ti/Al/Mo/Au and Ti/Al/W. The current-voltage (U-I) characteristics of the contact to AlGaN/GaN type heterostructure were measured and the SEM and EDX observations were conducted. The obtained result will be presented and validated.*

Keywords: AlGaN/GaN, ohmic contact, Au-free

1. INTRODUCTION

Usually used metallization scheme for ohmic contact preparation for AlGaN/GaN devices is Ti/Al/M/Au. Ti is a metal which role is to absorb nitrogen from heterostructure during RTA process and to improve adhesion of metallization to heterostructure. Aluminum is responsible for low contact resistance since it diffuses into heterostructure and makes electrical connection between metallization and two dimensional electron gas. Last layer could be gold, but during heating gold atoms diffuse into other layers and semiconductor resulting in interrupted contact structure. One way to prevent negative influence of gold is usage of the diffusion-stopping layers. In scheme for this layer sign M was used. M is usually metal with high molecular mass, big atomic radius and high melting point, like Mo, Ti, Ni, Pt. All these metals have low possibility of diffusion during RTA process and low risk of allow to diffuse gold atoms through them. Other way is to produce Au-free metallizations. Example of gold free ohmic contacts to AlGaN/GaN heterostructure, used in research described in this article, is Ti/Al/W [1]. Tungsten melting point is 3410–3422 °C, but usage of this metal also allow to reduce RTA temperature and it is a reason of comparison of two tungsten containing sample types – one annealed at temperature typical for gold including contacts (825°C) and other at lower temperature (600°C) [2].

2. SAMPLE PREPARATION

In research preparation of all samples was similar except deposited metallizations and annealing temperatures. Mutual steps in contacts fabrication were etching AlGaN/GaN heterostructure in RIE (Reactive Ion Etching) process using Cl_2/BCl_3/Ar plasma in purpose to obtain TLM (Transfer Length Measurement) devices. Heterostructures were produced in MOVPE (Metalorganic Vapor Phase Epitaxy) process. Metals were deposited on islands, obtained in RIE process, by PVD (Physical Vapor Deposition) method using an electron beam evaporator for W, Ti, Al and Mo and using a resistance heater for Au. Used metallization schemes were:

– Ti(23nm)/Al(100nm)/Mo(45nm)/Au(190nm),
– Ti(23nm)/Al(100nm)/W(100 nm).

Only one sample had first presented metallization scheme and it was proceeded in RTA process for 60 seconds at 825°C [3]. Second scheme was used for two samples. The first one was heated for 60 seconds at 825°C, and the other one was heated at 600°C for 60 seconds [4-6].

3. MEASUREMENTS AND RESULTS

After RTA process all samples surfaces were verified by examining their SEM images (Fig.1).

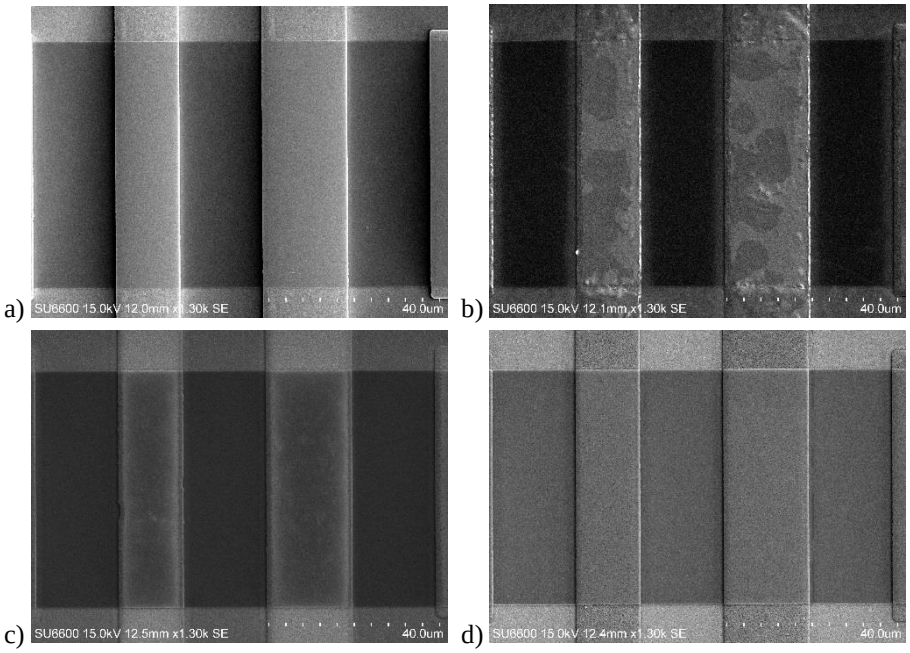

Fig. 1. Sample before annealing and samples after RTA process: a) Ti/Al/Mo/Au before RTA b) Ti/Al/Mo/Au (RTA: T = 825°C), c) Ti/Al/W (RTA: T = 825°C), d) Ti/Al/W (RTA: T = 600°C)

SEM images shows visible differences between all samples. Gold containing contacts after RTA process have not uniform surface, it means metals melted during process and became mixed. This process occurs although diffusion stopping layer was deposited and although gold melting point is 1 064 °C. In thin layers melting points are lower, so Au may melt at forming temperature and dissolve in other metals. Both Au-free samples characterizes with surface similar to samples before RTA process, but metallization heated at higher temperature (825°C) has edges different from surface located away from edges. EDX (Energy-Dispersive X-ray spectroscopy) analysis is difficult and in case of thin metallic layers it is hard to say, what metal is on the top, because signals are not from surface, but from depth between 0.3 to 3 µm depending on the material. But EDX may be helpful in concluding if layers are melted or if metals agglomerated. Samples checked using SEM looked as if they were melted and as if the remelting process started on edge and progress inside metallization. Responsible for this are atoms movements on edges, for lower small amount of energy is necessary to move atom on surface of metallization, than for diffusion of this atom through metallization, so melting process is highest on edges. EDX plots for samples shows that deeper layers are similar on edges and away from edges (Fig.2, Fig. 3).

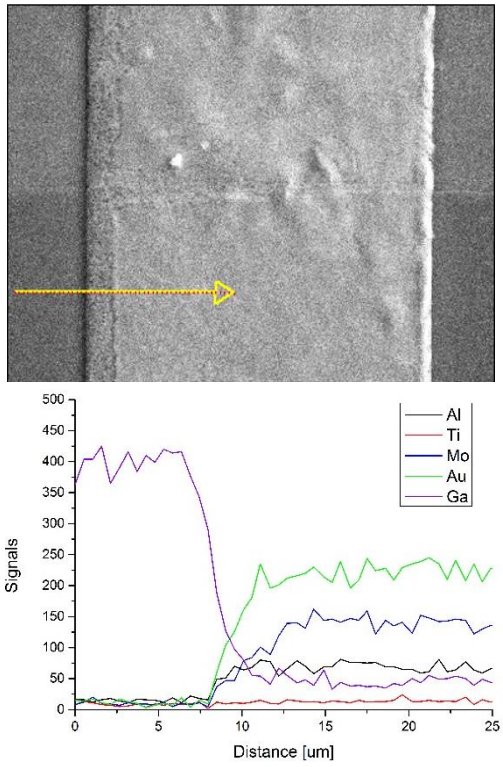

Fig. 2. SEM image with marked line checked by EDX (on left, the same for all samples) and EDX for sample with gold including contacts (on right)

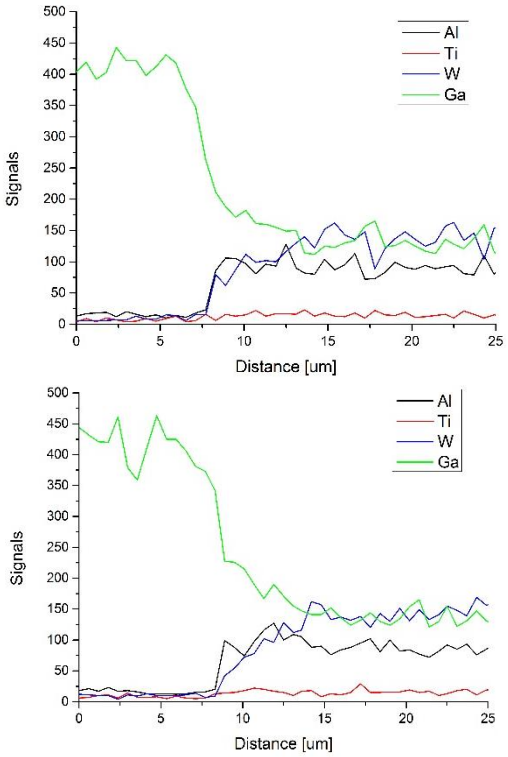

Fig. 3. EDX for Au-free samples: RTA 600°C on left and RTA 825°C on right

Resistances of contacts and sheet resistances for Au-free samples were higher, than in case of gold containing sample. But comparison of only Au-free contacts shows interesting conclusion, that for these contacts lower temperature allows to obtain lower resistances. Sheet resistances for metallizations with tungsten are high because of high resistivity of this metal, but alloys with other metals present in contacts and the amount of which increases with temperature increase makes sheet resistance of contacts higher for samples heated at higher temperatures (Tab.1, Fig.4).

Table 1. Electrical parameters of contacts

Metallization	RTA T[°C]	Rc[Ω*mm]	R[Ω/□]
Ti/Al/Mo/Au	825	4.10	2.05
Ti/Al/W	825	13.16	28.75
Ti/Al/W	600	10.44	18.29

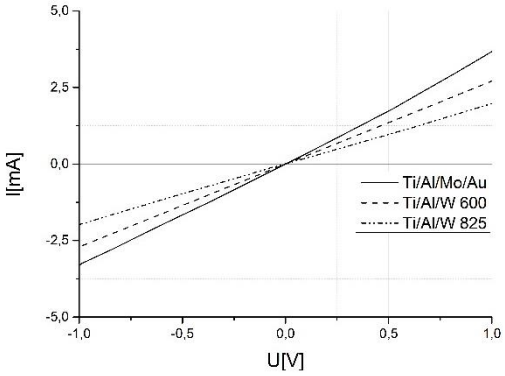

Fig. 4. U-I characteristic for checked samples

All measured characteristics were ohmic. But the results were not ideal results because of many reasons, for example differences in crystalline structure of semiconductor. Deviations from the straight line may be checked by determination of differential (Fig.5).

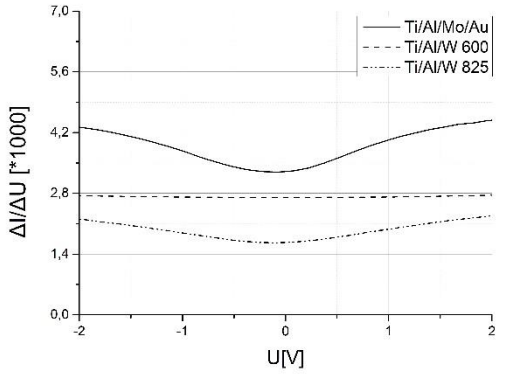

Fig. 5. Differential for checked samples

Differential for straight line is constant, so the more constant differentials of measured lines are, the lower is deviation of measurements from ideal linear function. The lowest deviation are for gold-free contacts heated at 600°C. Higher is for tungsten including contacts formed at 825°C, so lower temperature is proper for obtaining ohmic contacts in case of this metallization scheme. Deviations for gold including samples are the highest. For all samples differential range is 10^{-3}, so this check may be useful to conclude which formation conditions are proper for example in case, when voltage-current characteristics are similar.

4. CONCLUSION

In conducted research three sample types were checked, Ti/Al/Mo/Au, annealed at 825°C and two gold free samples, Ti/Al/W, heated at 600°C and 825°C. Because of gold high diffusity and lower melting point in case of thin metallic layers, the gold containing metallizations are remelted. Au-free contacts have better surface, with small remelts on edges in case of contacts heated at 825°C and no remelts in case of metallization formed at 600°C. EDX analysis suggest that inside metallization they are no agglomerates or metal losses. High resistivity of tungsten resulted in high sheet resistance, but lower of these two sample types was for samples annealed at lower temperature. Also differential suggest that better parameters to Au-free contacts formation is 600°C than temperature typically used for gold containing metallizations (825°C). Although gold containing samples had worse irregular surface than metallization with tungsten, the electrical parameters, which are more important than visual properties, are better for gold containing samples. Au-free contacts may be useful, but research on thickening of tungsten layer and research on reduce of contact resistance should be conducted.

Acknowledgement

This work was co-financed by the National Centre for Research and Development grants TECHMATSTRATEG No.1/346922/4/NCBR/2017, the National Science Centre grant No. DEC-2015/19/B/ST7/02494, Wroclaw University of Technology statutory grants and by the Slovak-Polish International Cooperation Program. This work was accomplished thanks to the product indicators and result indicators achieved within the projects co-financed by the European Union within the European Regional Development Fund, through a grant from the Innovative Economy (POIG.01.01.02-00-008/08-05) and by the National Centre for Research and Development through the Applied Research Program Grant No. 178782 and Grant LIDER No. 027/533/L-5/13/NCBR/2014.

References

[1] T. Yoshida, T. Egawa, *Phys. Status Solidi A*, (1700825) 1-5, (2018)

[2] A. Firrincieli, B. De Jaeger, S. You, D. Wellekens, M. Van Hove, S. Decoutere, *Japanese Journal of Applied Physics*, 53, (04EF01) 1-3 (2014)

[3] J. Zhang, S. Huang, Q. Bao, X. Wang, K. Wei, Y. Zheng, Y. Li, C. Zhao, X. Liu, Q. Zhou, W. Chen, and B. Zhang, Applied Physics Letters, 107, (262109) 1-5 (2015)

[4] Q. Li, Q. Zhou, S. Gao, X. Liu, H. Wang, Solid State Electronics 147, 1–5, (2018)

[5] T.Hsieh, Y.Lin, C. Chu, Y. Chuang, Y. Huang, W.Shi, C. Dee, B. Majlis, W. Lee, E. Chang, *Journal of Electronic Materials*, 45, 3285-3289 (2016)

[6] G. Greco, F. Iucolano , F. Roccaforte, Applied Surface Science 383, 324–345, (2016)

MICROFLUIDIC MICROPOT – FULLY 3D PRINTED INNOVATIVE TOOL FOR SEED QUALITY ASSESSMENT

B. Kawa*, K. Adamski, D. Lizanets, R. Walczak

Faculty of Microsystem Electronics and Photonics, Wrocław University of Science and Technology, Janiszewskiego 11/17, 50-372 Wrocław, Poland
*e-mail: bartosz.kawa@pwr.edu.pl

Abstract: *Traditional methods of seed quality assessment include sowing seeds, waiting for them to grow and then evaluating the quality from amount of harvested plants. This approach is time consuming, subjective and costly. If we think about maximizing production of the plants used for food industry we have to develop objective and more precise method for modern farming. In this work, we present an innovative tool for seed quality measurement. The device is fully 3D printed microsystem and utilizes cantilever like sensors for root and stalk growth force measurement. It is done by determination of 3D printed, mechanically characterized, sensor deflection. The readout is carried out using optical detection and dedicated software. When deflection is converted to force, it can be correlated with a quality of the seed. Micropot utilizes 500 μm microchannels to supply seed with water and nutrition. The influence of nutrients on growing time and force of lepidium sativum was measured and compared to water supplying.*

Keywords: *3D printed microsystem, seed quality, mechanical characterisation, microfluidics*

1. INTRODUCTION

In nowadays farming there is a great need of reaching the highest efficiency to maximise plant production and therefore profit. One of the key factors to achieve that is testing and increasing sown seed quality. Modern agriculture place a great emphasis on developing new more precise and reliable tools for seed quality examination.

There are few standard methods of seed quality examination like: physical quality (appearance is checked); seed size and weight (which should be proper for specific plant type); warm test; genetic purity done by electrophoretic evaluation and vigor testing. In the last case, vigor testing, gives us the abbility to predict a seed lot's potential to perform during growth. The most popular vigour tests are: cold germination, accelerated aging, electrical conductivity measurement and seed growth rate. [1,2]

Those methods are slow, subjective and require qualified and experienced personnel. Recently Hida et al. presented an approach of correlating pressure generated by root with growth potential [3]. In this case technology of glass and silicon chip was used. This kind of micromachinning techniques require expensive materials such as silicon and borosilicate glass and perilous chemicals such as HF and KOH. Another disadvantage of this technological approach is that the geometry and packaging of the sensor and therefore whole system is limited. Moreover, technology due to the many litographic steps is complex and also require qualified personnel. Therefore there is a great need of

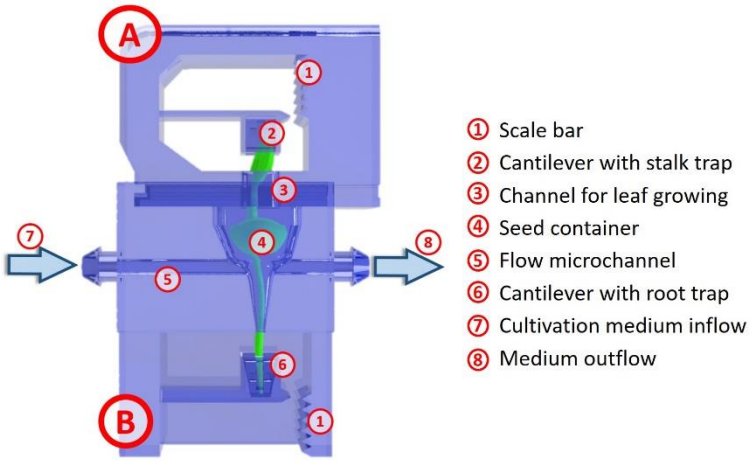

Fig. 1. Design of fully 3D printed microfluidic micropot

developing new tools and technologies for the seed potential investigation. 3D printing technology meets all assumptions for this field [4]. It is a technology that alows us to design and fabricate in short time systems like: modular[4] and integrated[5] fluidics, microfluidic structures [6], DNA chips[7]. In our work, we present fully inkjet 3D printed microfluidic microsystem (micropot) with embedded cantilever-type force sensor for stalk and root growth force measurement. One of the many advantages of this system is optical method of force measurement. The micropot design is shown on the Figure 1.

2. MATERIALS AND METHODS

2.1. Mechanical characterisation of 3D printed sensor

Presented micropot utilized 3D printed microcantilever like, force sensors. Structures were fabricated by Projet 3510 printer with XHD printing resolution (3D Systems, USA) with M3 Crystal as a building material and S300 used as support material. The resolution in planar directions was 750 dpi and layer thickness was 16 μm. This 3D printing technique requires post processing of printed objects which involves mineral oil bath, ultrasonic cleaning and in the end cleaning with detergent. Sensor structures were 4 mm long and 2 mm wide. The thicknesses of the microcantilevers were from 200 μm to 600 μm. For each thickness mechanical characterization was performed in previous work [9]. Structures were mechanically tested by Bondtester Dage 4000 Plus (Nordson Dage, Germany). Examples of deflected 3D printed microcantilever sensor and mechanical characterization are shown in the Figure 2

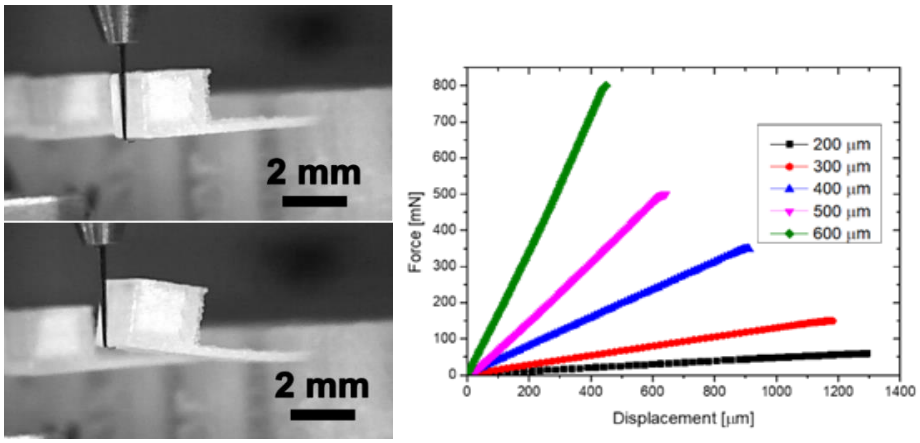

Fig. 2. Mechanical characterisation of 3D printed cantilever-type sensor: (I) non deflected, (II) deflected, (III) deflection and force characteristic

2.2. Optical detection of deflection and measuring set up

The key feaure of the system is that the measurement is performed with noninvazive way by CCD camera which acquire the image which is then analyzed by dedicated software. Program records the captions and in the end of the measurement processes them to obtain the information about cantilever deflection therefore, about the force of growth. The measuring setup consists of micropot itself which is supplied with water or nutriens (BIOHUMUS, natural nutrient, EKODARPOL). To obtain precise dosing of agents, piezoelectric micropump (Bartel's mp6 micropump) was used. Temerature of the cultication chamber was stabilized at 22 ºC to obtain optimal conditions for seed germination. The scheme of the system is shown in the Figure 3.

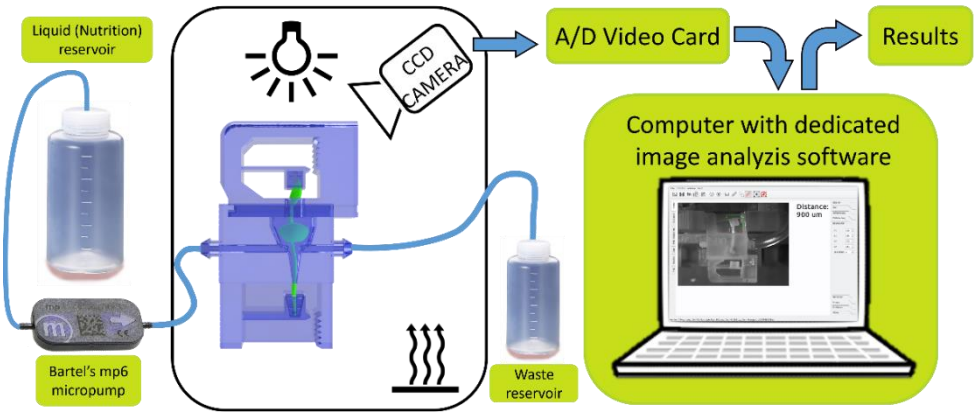

Fig. 3. Scheme of the measuring system

3. RESULTS

Presented system/tool for seed quality assessment utilizing fully 3D printed microfluidic microsystem was developed, characterized and preliminary plant growth studies were carried out on it. Using this system we measured driving forces of root and stalk for Lepidium sativium plant. The maximum force for the stalk was equal to 55 mN, plant was supplied with water, results are shown in the Figure 4. In case of stalk the maximum measured value was over 900 mN. In order to check real influence of nutrients on plant growth, seeds were provided through integrated microchannels with solution of 5 % nutrient (biohummus) in water. Results of comparison non stimulated and stimulated growth are shown in the Figure 5. It occurs that stalk with nutrient supply can reach growing forces over 3 N, comparing to non-stimulated 1 N. It is clearly visible that germinating time is reduced from 85 h to less than 50 h.

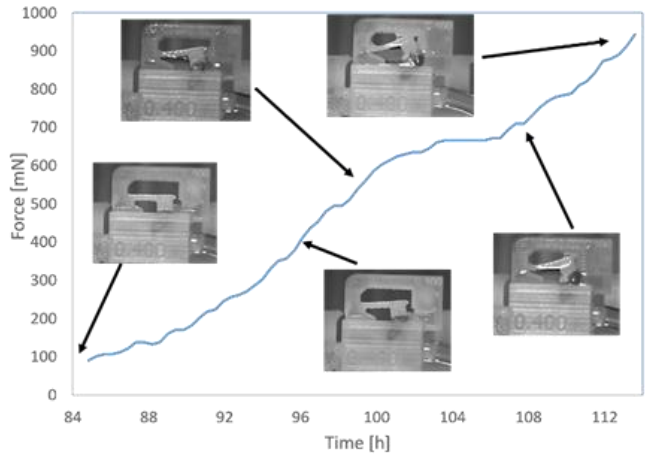

Fig. 4. Stalk growth in time

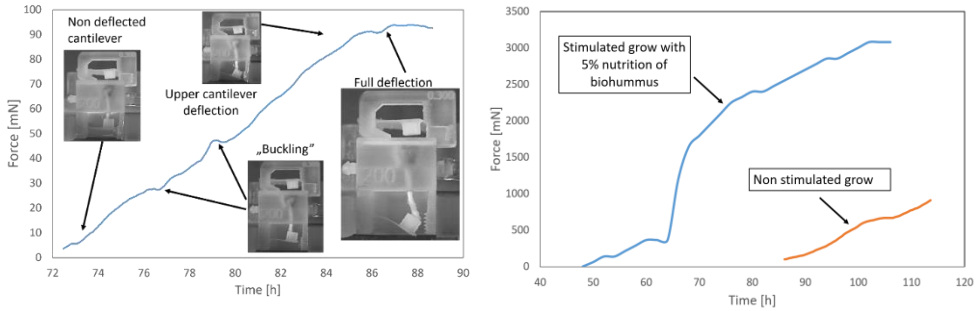

Fig. 5. Growth force in time characteristics: a) for root supplied with water, b) comparison in time for stimulated and non-stimulated grow

4. SUMMARY

In this work, we presented a modern tool for seed quality assessment. The device is fully 3D printed microfluidic microsystem. Two integrated cantilever-type mechanicaly characterised sensors are measuring root and stalk growing forces. The quality examination is conducted by correlating measured forces with growth potential of the plant. The whole measuring setup is fully automate. Thanks to the 3D printing technology, both micropot and the measuring system are scalable which is their great advantage. Micropot can be redesigned concerning size of the seed and predicted driving forces and measuring system can be scaled up to achieve big number of conducted test at one time. Presented system meets the requirements of the tool for modern farming for seed quality examination.

In this work, successful measurement of growing forces of root and stalk for Lepidium sativium was carried out. Additional the influence of stimulant on growing potential was examined .

Acknowledgement

This works was financed by Wroclaw University of Science and Technology grant for young scientist number 0402/0051/17 and Wroclaw University of Science and Technology statuary grant number 0401/0019/17

References

[1] P. Basu, A. Pal, A new tool for analysis of root growth in the spatio-temporal continuum, New Phytol. 2012 Jul;195(1):264-74. doi: 10.1111/j.1469-8137.2012.04149.x

[2] MARCOS FILHO, Julio. Seed vigor testing: an overview of the past, present and future perspective. *Sci. agric. (Piracicaba, Braz.)* [online]. 2015, vol.72, n.4 [cited 2018-11-21], pp.363-374

[3] H. Hida et al., *Proc. of 21st uTAS 2017* Conf., 978-0-692-94183-6/µTAS 2017/$20©17CBMS-0001, 185

[4] R. Walczak, K. Adamski, A. Pokrzywnicka, W. Kubicki, Inkjet 3D Printing–Studies on Applicability for Lab-on-a-chip Technique, Procedia Engineering Tom 168 pages 1362-1365

[5] R. Walczak, K. Adamski, W. Kubicki, "Configurable on-Chip Gel Electrophoresis in Inkjet 3D Printed Microfluidic Modules, Proceedings 2017, 1(4), 520; doi:10.3390/proceedings1040520

[6] K. Adamski, J. Adamski, J. Dziuban, R. Walczak, Inkjet 3D Printed Miniature Water Turbine Energy Harvester-Flow Meter for Distributed Measurement Systems, MDPI Proceedings 1 (4), 578, 2017

[7] R. Walczak, K. Adamski, A. Pokrzywnicka, W. Kubicki, Inkjet 3D Printing–Studies on Applicability for Lab-on-a-chip Technique, Procedia Engineering Tom 168 pages 1362-1365

[8] R. Walczak, K. Adamski, W. Kubicki "Inkjet 3D printed chip for capillary gel electrophoresis", Sensors and Actuators B: Chemical, vol. 261C, 474-480

[9] B. Kawa, K. Adamski, R. Walczak, D. Lizanets, Mechanical Characterization of Inkjet 3D Printed Microcantilevers, COE 2018 proceedings

THE INFLUENCE OF QUANTUM WELL AND BARRIER THICKNESSES ON PL SPECTRA OF INGAAS/ALINAS SUPERLATTICES GROWN BY LP-MOVPE

A. Łozińska, M. Badura, K. Bielak, B. Ściana, M. Tłaczała

Faculty of Microsystem Electronics and Photonics, Wrocław University of Science and Technology, Janiszewskiego 11/17, 50-372 Wrocław, Poland

Abstract: *In the presented work the influence of quantum well and barrier thicknesses on optical characteristics of InGaAs/AlInAs superlattices was reported. Six different structures of $In_{0.53}Ga_{0.47}As/Al_{0.48}In_{0.52}As$ superlattices lattice-matched to InP were grown by* ***Low Pressure Metal Organic Vapour Phase Epitaxy (LP-MOVPE)****. Optical properties of the obtained structures were examined by means of photoluminescence (PL) spectroscopy. This technique allows quick, simple and non-destructive measurements of radiative optical transitions in different semiconductor heterostructures. The analysis of recorded PL spectra revealed the influence of the quantum well and barrier thicknesses on the emission line energy and its intensity.*

Keywords: photoluminescence, quantum cascade lasers, MOVPE

1. INTRODUCTION

A superlattice is a periodic structure of layers of two or more different materials. It is important to realize a difference between superlattices and multiple quantum wells, because they are very comparable in their structure, except that unlike the multiple quantum wells, the superlattice barrier thickness is small enough that electron states interpenetrate between individual quantum wells [1]. Superlattices based on InGaAs/AlInAs heterostructure are mostly used in the construction of quantum cascade lasers QCLs [2]. The QCL core contains hundreds or even thousands of repetitions of thin layers with a thickness in the range of 0.5÷10 nm. Because of the sophisticated nature of QCL construction, it is important to find the optimal technological parameters. The growth kinetics depends on several factors such as: a flow rate of precursors, process pressure and temperature which strongly affect the growth of individual layers [3]. In the case of layers with a thickness of a few nanometers, many popular measurement methods can not be used. Photoluminescence is one of the most useful technique for optical characterization of different semiconductor structures dedicated to optoelectronic devices, especially emitters [4]. PL spectra allow to determine the band gap energy, the dependence of the peak location of the maximum emission on the temperature or the excitation power.
The paper presents optical characterization of InGaAs/AlInAs low-dimensional structures in which InGaAs is a quantum well (QW) and AlInAs is a barrier (B).

2. EXPERIMENTAL DETAILS

Six different structures of InGaAs/AlInAs superlattices were grown by Low Pressure Metal Organic Vapour Phase Epitaxy (LP-MOVPE). The designed material parameters of investigated structures are collected in Table 1.

Table 1. List of project assumptions of the investigated InGaAs/AlInAs superlattices

SAMPLE	NUMBER OF REPETITIONS	THICKNESS OF $In_{0.53}Ga_{0.47}As$ d_{QW} [nm]	THICKNESS OF $Al_{0.48}In_{0.52}As$ d_B [nm]
A	50	10	1
B		10	3
C		10	5
D		10	10
E		5	10
F		2	10

Each sample consisted of 50 repetitions of two layers: the InGaAs quantum well and the AlInAs barrier lattice-matched to InP (Fig. 1). In the case of the samples A÷D the thickness of InGaAs quantum well (d_{QW}) was constant of 10 nm while the thickness of AlInAs barrier was changed from 1 nm to 10 nm. For the samples D, E and F the thickness of AlInAs barrier (d_B) was kept constant of 10 nm while the thickness of InGaAs QW was varied from 2 nm to 10 nm.

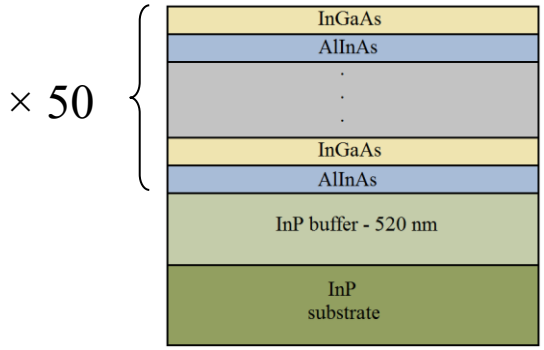

Fig. 1. A sectional view of the investigated InGaAs/AlInAs/InP heterostructures

The epitaxial processes were carried out using AIXTRON 3×2″ FT CCS system at the pressure of 100 mbar. The growth temperature was 645°C. A high purity hydrogen was applied as a carrier gas while trimethylaluminium (TMAl), trimethylgallium (TMGa), trimethylindium (TMIn), arsine (AsH_3) and phosphine (PH_3) were used as III- and V-group element sources, respectively. The superlattice composition was controlled by the hydrogen flow rate through TMGa and TMAl saturators at the fixed hydrogen flow rate through TMIn saturator. The optical properties of the fabricated samples were measured by means of low temperature photoluminescence (LT PL).

3. RESULTS

PL spectra were measured at low temperature (88 K) using AlGaAs/GaAs laser excitation of 641 nm (continuous wave CW, optical power 10 mW). As a detector the StellarNet DW ARF-STAR NIR-100 spectrometer was employed (InGaAs photodiode, 600g/mm, integration time 100 ms).

In the case of quantum cascade lasers one of the most important properties is a sharp and narrow peak of the maximum emission. According to the theory with decreasing the thickness of the quantum well, the peak should shift towards shorter wavelengths (Blue Shift). This dependence is described by a formula (1):

$$E = \frac{n^2 \hbar^2 \pi^2}{2 m d_{QW}^2} \quad (1)$$

where n is natural number describing the next energy level, $\hbar$ is the reduced Planck constant, m is the effective mass of the particle and d_{QW} is the thickness of the quantum well [1].

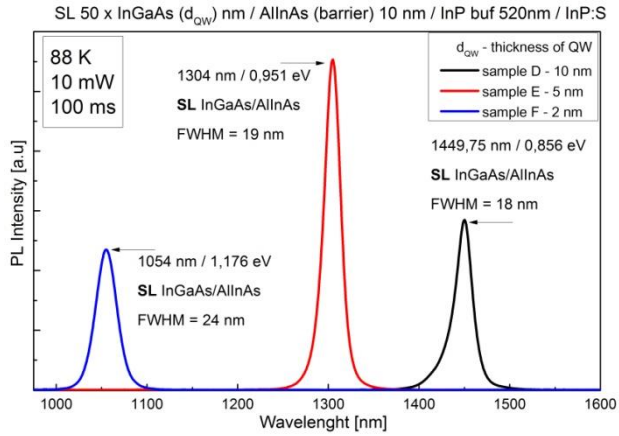

Fig. 2. PL spectra of the samples D, E, F recorded at 88 K with the excitation power of 10 mW

PL spectra of three samples D, E and F in which the variable parameter was quantum well thickness (10, 5 and 2 nm, respectively) are shown in Fig.2. According to the formula (1), as the thickness of the quantum well decreases, the energy of the optical transition increases, so the peak of maximum emission should be shifted towards shorter wavelengths [1,5]. In the case of the sample E, the PL peak location was shifted toward shorter wavelengths of 150 nm in comparison to the sample D, in which the quantum well thickness was twice larger. The separation between PL peaks of the samples E and F was 250 nm what corresponds to a reduction in the quantum well thickness 2.5 times. The observed changes of the PL peak position for different InGaAs quantum well thicknesses confirm the theory described by the formula (1). No additional optical transitions between light or heavy holes and electrons were observed in the presented PL spectra what can result from a high quality of the measured heterostructures. The PL intensity is not significant, because the samples were not measured simultaneously.

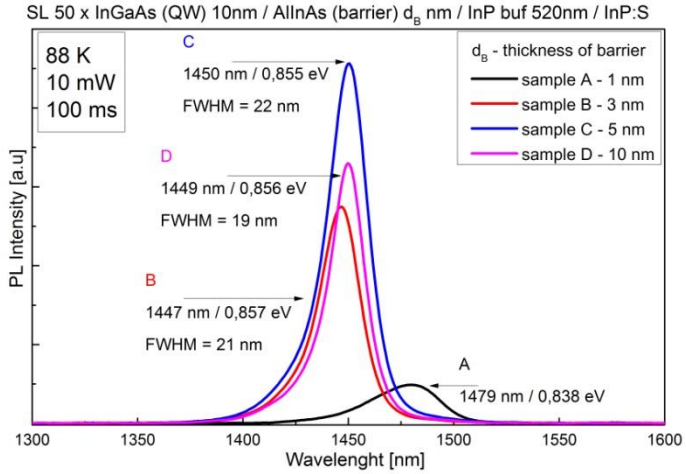

Fig. 3. PL spectra of the samples A, B, C and D recorded at 88 K with the excitation power of 10 mW

PL spectra of the samples A, B, C and D, in which the variable parameter was barrier thickness d_B (1, 3, 5 and 10 nm, respectively) are shown in Fig.3. The PL intensity is not significant, because the samples were measured at certain intervals of time. In the case of the samples B, C and D, the position of maximum emission does not change distinctly (only a few nanometers). The shift of the maximum emission by 2 nm (~ 1 meV) in the case of the sample B was probably caused by a change of the InGaAs quantum well thickness by half of a lattice parameter. The small influence of the barrier thickness on the PL line energy indicate that the emission depends mainly on the quantum well thickness, which was constant for the considered samples. The situation differs when the barrier thickness is very narrow of 1 nm (sample A). In the case of this sample, the position of maximum emission shifts towards the longer wavelengths of 30 nm and a broadening of PL spectrum is observed (FWHM= 41 nm). This is caused by the formation of a miniband characteristic for superlattice structure [1].

4. SUMMARY

Six InGaAs/AlInAs structures were grown on InP substrate by LP-MOVPE. The influence of the quantum well and barrier thicknesses on PL spectra was described. A shift of the emission line towards the shorter wavelengths caused by decreasing of the quantum well thickness was observed. The analysis of PL spectra recorded for the structures with different barrier thickness revealed that only the sample A with the narrowest barrier of 1 nm exhibits features attributed to a superlattice structure. The next stage of research will be focused on determination the maximum barrier thickness allowing the formation of the superlattice miniband.

Acknowledgements

This work was co-financed by Wrocław University of Science and Technology statutory grants and by the Polish National Centre for Research and Development through projects PBS2/A3/15/2013 (PROFIT), TECHMAT-STRATEG1/347510/15/NCBR/2018 (SENSE).

References

[1] S. Kasap, P. Capper, *Springer Handbook of Electronic and Photonic Materials 2nd Edition*, Springer International Publishing, 1037-1055, 2017, **DOI 10.1007/978-3-319-48933-9**.

[2] M. Bugajski, P. Gutowski, P. Karbownik, A. Kolek, G. Hałdaś, K. Pierściński, D. Pierścińska, J. Kubacka-Traczyk, I. Sankowska, A. Trajnerowicz, K. Kosiel, A. Szerling, J. Grzonka, K. Kurzydłowski, T. Slight, W. Meredith, *Physica Status Solidi (B)* **251**(6), 2014, pp. 1144–1157, **DOI 10.1002/pssb.201470135**.

[3] M. Badura, K Bielak, B. Ściana, D. Radziewicz, D. Pucicki, W. Dawidowski, K. Żelazna, R. Kudrawiec, M. Tłaczała, *Optica Applicata*, **Vol. XLVI**, No. 2, **DOI: 10.5277/oa160208, 2016**.

[4] A. Wójcik-Jedlińska, M. Wasiak, K. Kosiel, M. Bugajski, *Optica Applicata*, **Vol. XXXIX**, No. 4, 2009, pp. 967-974

[5] Y.Wang, X. Sheng , Q. Guo , X. Li , S. Wang , G.Fu, Y.I. Mazur , Y. Maidaniuk , M.E. Ware , G.J. Salamo , B. Lian, D. L. Huffaker, *Nanoscale Research Letters* (2017) 12:229**. DOI 10.1186/s11671-017-1998-8**

OPTICAL MEASUREMENT IN PLASMA MICROREACTOR

T. Matusiak*, L. Golonka

Faculty of Microsystem Electronics and Photonics, Wrocław University of Science and Technology, Janiszewskiego 11/17, 50-372 Wrocław, Poland
*e-mail: tomasz.matusiak@pwr.edu.pl

Abstract: *In this work, we present some practical aspects of optical measurement in plasma microreactor. Small optical path attenuation between the microreactor and a spectrometer is necessary for the measurement. Microreactors are made with minimum one open wall of discharge chamber to observe spectra. We present two ways of transmitting the optical signal: through a lens or using optical fiber. The properties of both solutions are presented.*

Keywords: optical emission spectroscopy, plasma, low temperature cofired ceramics

1. INTRODUCTION

Optical Emission Spectroscopy (OES) is one of the most popular tools to describe plasma properties. It is used to register spectra from ICP (Inductively Coupled Plasma) and CCP (Capacitively Coupled Plasma) reactors under atmospheric pressure and recently in Atmospheric Pressure Glow Discharge (APGD) in contact with liquid solutions. Last excitation source is the most promising in analytical chemistry. Atoms and molecules are emitting their characteristic wavelengths mainly in the range from 200 nm to 800 nm. The measurement in the UV region is a problem. We present solutions how to register emission spectra from plasma microreactor made in Low Temperature Cofired Ceramics (LTCC) technology [1].

2. METHODS

The LTCC microreactors are of the ELCAD (Electrolyte as Cathode Discharge) type [2,3]. The plasma is generating between liquid cathode and solid anode in atmospheric pressure. Metallic species in liquid cathode could be marked with some Detection Limit (DL) [4], which formula is given by:

$$DL = 3\sigma/\alpha \text{ [ppb]} \quad (1)$$

Where:

α – slope of the calibration curve,

σ – standard deviation of the background.

The DL formula gives us that the ratio of intensity at marked point to noise is the basic of OES calculation. The optical path of the emitted spectra and the correct alignment have an effect on DL. We propose two ways of transmitting the optical signal: through lens or using optical fiber.

2.1. Lens

The first proposed method is transmitting the optical signal through collimating lens and recording spectra by a spectrometer. This is a difficult solution due to the need for good positioning in one line of microreactor, lens and spectrometer. The small movement of microreactor sometimes has a huge influence on registered spectra. The schema of the setup is presented in Fig. 1. The main advantage of this method is that the high temperature from the plasma reactor does not disturb the optical path.

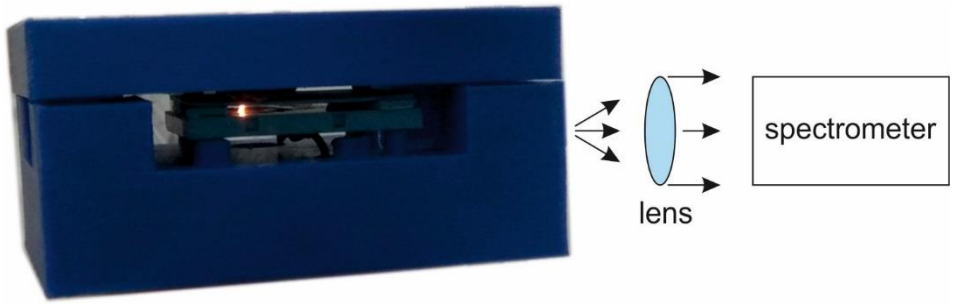

Fig. 1. Measurement setup with lens

2.2. Optical fiber

The second solution is optical fiber as the path for emitting light from the microreactor [1]. To proper alignment SMA slot between the open wall of the discharge chamber, we print polymer housing (Z-ABS) in 3D technology. This concept is presented in Fig. 2.

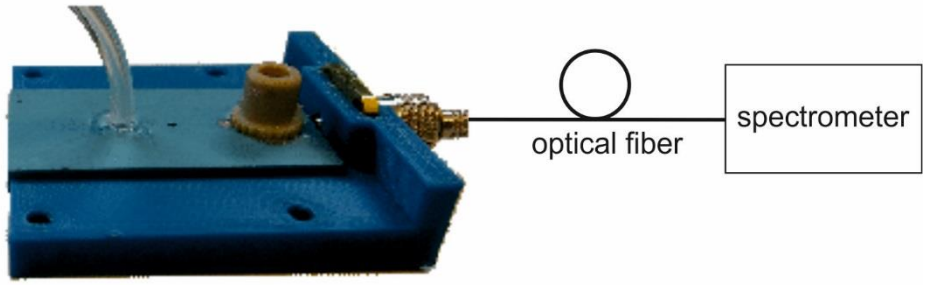

Fig. 2. Measurement setup with optical fiber

The emission lines of metallic species (Cd, Zn, Cu, Ag) are in UV region. The communication optical fibers have some attenuation in this part of the spectra. We propose to use optical fiber with high OH group concentration, which has good performance in the UV region. For example, attenuation of high OH fiber [5] for Cd spectrum (213.7 nm) is about 0.45 dB/m and for Na (589.8 nm) it is about 0.03 dB/m. These are good results for short fiber setup. Attenuation of the OH fibers as a function of the wavelength is presented in Fig. 3. Moreover, some emission lines of metals are also marked there.

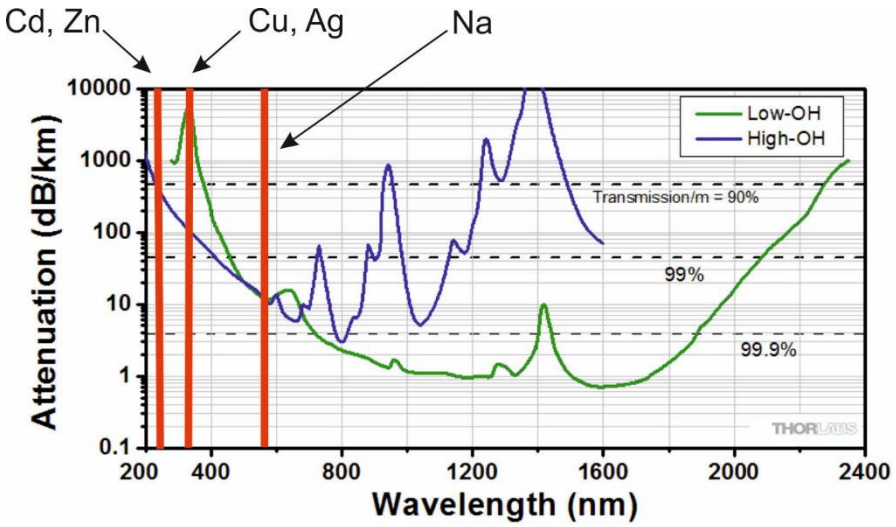

Fig. 3. Comparison of optical fibers with high and low OH concertation [5]

2.3. Discussion

Influence of optical path could be compared on OH-X group, which was registered in every spectrum. Andor Shamrock SR-500i was used as the spectrometer and detector CCD Newton 920 with diffraction grating 1800 lines per mm for UV range and 1200 lines per mm for VIS. In compare, we focus on generating radiation from OH molecules. Tab. 1 presents samples of register OH spectra with the normalized arbitrary unit. A solution of 0.1 M HNO3 was under test. In brackets are values corrected by fiber attenuation.

Table 1. Comparison of optical fibers with high and low OH concertation

Optical path	**Intensity of OH spectra [a.u.]**		
Lens	10	9.9	10
Optical fiber	9.4 (9.97)	9.3 (9.765)	9.3 (9.97)

3. SUMMARY

Two different solutions for the optical path are presented. Both require an additional stuff. Lens provides the best intensity for UV range, but there is the problem with the proper alignment of the lens between microreactor and spectrometer. It is a time-consuming work but the additional place in the housing of chip is not necessary for SMA slot. The optical fiber presents good performance and after correcting fiber attenuation, the results of intensity are almost the same as in lens case. The disadvantage of the fiber optic is some contamination on the front of the fiber which could have a huge effect on attenuation.

Acknowledgement

The authors wish to thank Dr Jan Macioszczyk for his help and University of Science and Technology (statutory activity) for financial support.

References

[1] J. Macioszczyk, T. Matusiak, P. Jamróz, L. Golonka, In *2017 40th International Spring Seminar on Electronics Technology (ISSE)*, Sofia, Bulgaria, 1-5 (2017)

[2] T. Cserfalvi, P. Mezei, P. Apai, *J. Phys. D Appl. Phys*. 26, 2184–2188 (1993)

[3] R. Webb, F. J. Andrade, G. M. Hieftje, *J. Anal. At. Spectrom.* 22, 766 - 774 (2007)

[4] T. Little, *BioPharm International 28, 48-51 (*2015)

[5] https://www.thorlabs.com/newgrouppage9.cfm?objectgroup_id=6838

PHOTOPHYSICAL PROPERTIES OF DISPERSIONS OF Zn-Ag-In-S-BASED ALLOYED SEMICONDUCTOR NANOCRYSTALS

S.G. Mucha, L.M. Mazur, K. Matczyszyn*

Advanced Materials Engineering and Modelling Group, Wroclaw University of Science and Technology, Wyb. Wyspianskiego 27, 50-370 Wroclaw, Poland

*e-mail: katarzyna.matczyszyn@pwr.edu.pl

Abstract: *Recently, non-toxic I-III-VI semiconductor nanocrystals (NCs) have been intensively studied as promising alternatives for nanostructures containing heavy metals (Cd, Pb, Hg) due to their low cytotoxicity and relatively high photoluminescence (PL) quantum yields. In this review, various Ag-In-Zn-S-type (ZAIS) colloidal solutions of NCs are presented from structural, as well as photophysical point of view confirming a facile tunability depending on composition, chemical nature of ligands and stoichiometry of individual components. Considering various spectroscopic techniques, a strong correlation between PL parameters and the aforementioned factors were mainly revealed. Moreover, they may constitute an outstanding background for interpretations of photophysical phenomena involving three radiative recombinations pathways which indicate the existence of donor/acceptor states.*

Keywords: photoluminescence, nanocrystals, semiconductors

1. INTRODUCTION

In recent times, the research in the field of nanoscience is focused on a more biocompatible alternative candidate for Pb-, Hg- and Cd-containing nanocrystals (NCs) leading to a reduction of a risk of further complications in living organisms, notably, it can be accumulated in mammal organs [1]. From the chemical point of view, incremental surficial oxidation of heavy metal-including chalcogenide-based NCs, without core-shell composition, induces an expulsion of ions (*e.g.* cadmium) revealing high cytotoxicity as an extremely dangerous system [2, 3]. Hence, a tremendous group can be defined wherein inspiring components, *i.e.* copper, indium, zinc, silver composed as sulfides or phosphides in alloyed, core-shell or cation-doped forms [4,5]. As a representative example, non-toxic I-III-VI semiconductor NCs, such as quaternary Zn-Ag-In-S-type (ZAIS), have attracted attention due to their remarkable electronic and optical properties offering an emission in the so-called 'biological window', which can be easily adjusted [6-8]. Knowing that the ZAIS NCs constitute a subject in chemistry, as well as in photophysics, many studies have been conducted in an effort to receive appropriate properties that may be used for biological applications (*e.g.* bioimaging), optoelectronics, solar cells, photodetection or photocatalysis [9, 10]. In this review, the major different approaches for composition design, chemical preparation of ZAIS NCs in correlation with their corresponding photophysical behaviour are briefly illustrated.

2. MATERIALS

2.1. Composition design

Taking into account their arrangement, the ZAIS NCs can be designed into two ways, either as an alloy (Zn-Ag-In-S) or as a core/shell composition (Ag-In-S/ZnS), within a ternary silver-indium polysulphide (denoted as AIS) is coated by means of zinc-like analog. Furthermore, a nanocrystalline composite may be doped with metal cations (*e.g.* Mn^{2+}) [11], whereby a unique example was reported by T.-T. Xuan *et al.* by incorporating Ag^{+} ions into Zn-In-S inorganic core [12]. Therefore, a crystal form of the common AIS part plays a significant role. Considering their stoichiometric constitution, two models are distinguished, such as $AgInS_2$ and $AgIn_5S_8$, which correspond to orthorhombic or tetragonal, and cubic structures, respectively [7, 13-15]. Nevertheless, they acquire non-identical lattice with a cubic ZnS that zinc ions have a tendency to a facile diffusion into the AIS core with a different rate, due to the Ag vacancies [4, 13, 16], resulting in off-stoichiometric formula ($Ag_xIn_yS_z$) and reaching enhanced photoluminescence (PL) properties [8]. Alternatively, in order to generate multilayer NCs, the lower temperature in the relatively rapid synthesis must be applied [7]. On the other hand, surface modifications *via* attaching different organic compounds are considered as an influential factor for adjusting a chemical affinity to solvents.

2.2. Synthesis methods

It should be noticed that widely-conducted studies on structural refinements, in the case of atomic ratios, as well as surface modifications, determine two principal routes for fabrications of the AIS and subsequently, the ZAIS NCs. The first one, proposed by Torimoto *et al.* [15], is dedicated to thermal decomposition of a prearranged single precursor, like metal ion-diethyldithiocarbamate or thiolates including: $Ag_xIn_{(1-x)}[S_2CN(C_2H_5)_2]_{(3-2x)}$ and $(AgIn)_xZn_{(2-2x)}[S_2CN(C_2H_5)_2]_4$ for the AIS and ZAIS, respectively [6, 17]. Moreover, long chain amines (oleyamine – OLA, octylamine – OA) can be used in a reaction system and alternatively, replaced by a mixture (octadecylamine - ODA oleic acid and 1-octacedene) or trioctylphosphine (TOP) [7]. The procedure requires a synthesis of these starting materials from simpler substances, for instance, highlighting a diethyldithiocarbamate anion mixing simultaneously with silver, indium and zinc nitrates in an aqueous solution. In the second preparation route, all components are acquired from simple precursors, wherein indium is obtained from $In(OAc)_3$ [9, 10, 18, 19], $In(acetyacetone)_3$ [4, 20] or $InCl_3$ [8, 21], silver from $AgNO_3$ [7, 8, 13, 20] or Ag(OAc) [9, 10, 18, 19]. Considering zinc, it can be injected into starting mixture (for alloys) or deposited as a novel layer onto prepared NCs (core/shell constitution). Depending on the method, $Zn(OAc)_2$ [9, 10, 18, 20] or zinc stearate [4, 7, 8, 13] are commonly used. As a sulfur source, pure sulfur or thiourea powder dissolved in OLA, and thiols (*e.g.* 1-dodecanothiol - DDT) play a key role in a core outline. Furthermore, DDT with OLA, OA, TOP, BA (n-butylamine) and MUA (11-mercaptoundecanoic acid) constitute standard ligands for both NCs [21].

3. PHOTOPHYSICAL PROPERTIES

Concerning the aforementioned well-developed fabrication approaches, they allow arranging nanocrystalline composites influencing on their photophysical properties, such as tunable emission color (location of PL spectrum), enhanced photoluminescence quantum yield (PLQY), temporal behavior (PL lifetime). The following changes have been monitored via steady-state and time-resolved spectroscopy techniques.

3.1. Correlation with a various design.

Firstly, to characterize particularly the mechanisms carried out upon photoexcitation, the fundamental difference between a pristine $AgInS_2$, an alloyed ZnS-$AgInS_2$, and a double-layered $AgInS_2$/ZnS should be illustrated. Hence, combining results which have been revealed by G. Gabka *et al*. [8] and M.J. Rao *et al*. [22] (**Fig. 1.**), changes in spectral features

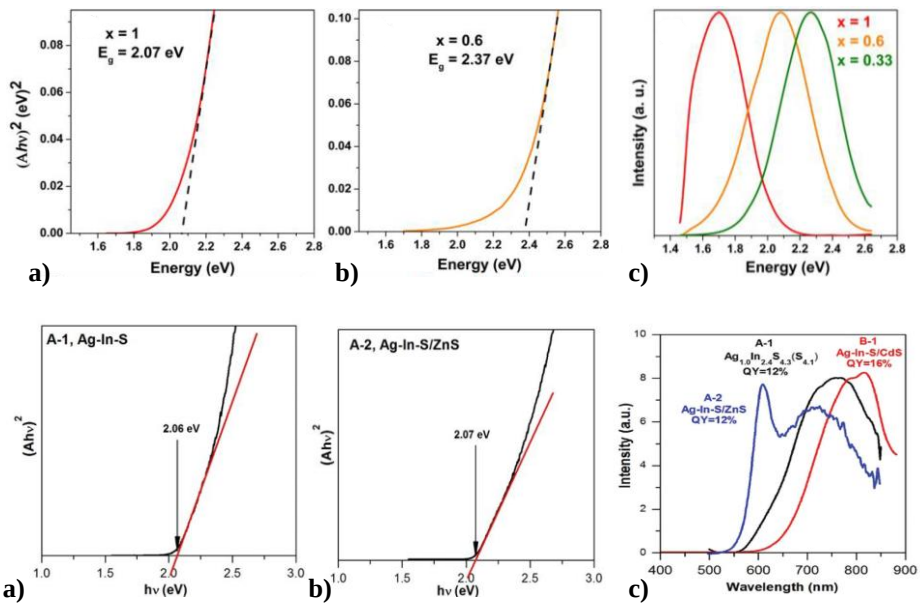

Figure 1. The Tauc plots (a-b) and PL spectra (c) for dispersed in hexane alloyed $(ZnS)_{1-x}(AgInS_2)_x$ (top) and a coated $AgInS_2$/ZnS (bottom). In both cases, graphs a correspond to pure $AgInS_2$ form [7, 22].

were stated, indicating similarities in bandgap energy values (E_g, calculated by conversion from absorption spectrum) between a free and capped AIS NCs with a hypsochromic shift of the band onset for the alloyed ZAIS – it can be assigned to alloying effects. On the other hand, zinc-enriched broad emission peaks are noticeably blue-shifted comparing to the AIS composite (c, bottom/top), centered at 751-754 nm (≈ 1.65 eV). As depicted above (c, top), the alloyed ZAIS possess the symmetric PL band with a maximum at 596 nm (2.08 eV for x = 0.6) or 549 nm (2.26 eV for x = 0.33). If core/shell structures are synthesized, with the shell layer being ZnS, one can observe asymmetric spectrum, consisting of a narrower peak at 612 nm (2.0 eV) and a broad peak centered at 720 nm (1.72 eV). This effect is explained

by partial alloying due to slow diffusion of zinc into a core. Taking into account the PLQYs, it turned out that the highest value is achieved by the alloyed ZAIS NCs, while the core/shell and pristine AIS NCs have the same (PLQY = 12%).

Thus, subsequent correlations, namely molar ratios between the components, are addressed only to the alloyed ZAIS NCs. As was widely studied, increasing content of zinc, as well as indium allows inducing significant variations of a PL spectrum position and PLQYs. Thereby, D.K. Sharma *et al.* [18] were focused on controlling emission color and efficiency

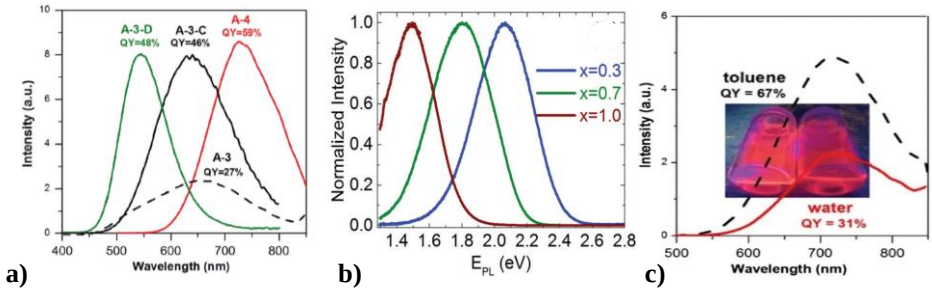

Figure 2. a) An emission spectra of the ZAIS NCs dispersed in hexane depending on contents of Zn, In and S: A-3 ($Ag_{1.0}In_{1.7}Zn_{1.0}S_{6.0}(S_{4.0})$), A-3-C ($Ag_{1.0}In_{2.7}Zn_{3.5}S_{5.0}(S_{8.0})$), A-3-D ($Ag_{1.0}In_{1.1}Zn_{5.6}S_{8.9}(S_{7.7})$) and A-4 ($Ag_{1.0}In_{3.1}Zn_{1.0}S_{4.0}(S_{6.1})$); b) The PL band for toluene-dispersed ZAIS NCs including a various amount of Zn: $Ag_{1.0}In_{1.0}S_{2.0}$ (red), $Ag_{0.7}In_{0.7}Zn_{0.6}S_{2.6}$ (green) and $Ag_{0.3}In_{0.3}Zn_{1.4}S_{3.4}$ (blue); c) Changes in the PL spectra for ZAIS NCs (A-4) in water and toluene [7, 18].

through an amount of zinc (**Fig. 2.b**), demonstrating a volcano-like tendency for PLQY values, but invariably blue-shifted spectra. It indicates that initially non-radiative surface states must be eliminated with simultaneous enhancement of radiative carrier recombination centers [4, 18] and afterwards, an effective separation of radiative sites is sharply reduced increasing a non-radiative pathway. These studies were developed by G. Gabka *et al.* [8]. Modifying molar ratios between Zn-, In- and S-components for a constant content of Ag (**Fig 2.a**) proved a previous relation (see **Fig. 2.b**) for **A-3** (630 nm, 1.97 eV) and **A-3-D** (543 nm, 2.28 eV). Further, effects of indium and non-organic sulfur (dissolved in OLA) were underlined illustrating an explicit red shift of emission band (**A-4**, an excess of indium component) and its fixed position (**A-3-C**, a higher amount of sulfur) with elevated PLQY in both cases. Indeed, a large quantity of slowly-diffusing indium precursors prompts a denser distribution of recombination centers [7, 10]. It should be noticed that a downgrade of non-thiolate sulfur, resulting in

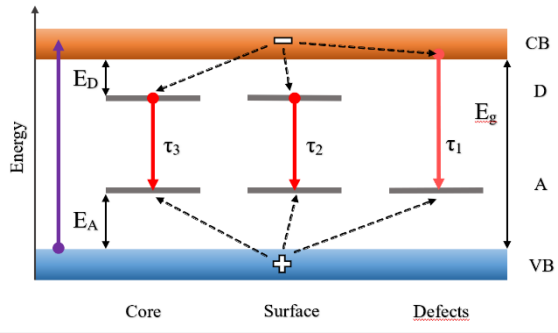

Figure 3. A proposed mechanism of photoluminescence in ZAIS NCs, where CB and VB denote conduction and valence bands, D/A donor/acceptor states, respectively [6].

more effective conversions of Zn and In during preparation. A similar outcome was found for a longer reaction time [10]. Additionally, by a dramatical change in a solvent polarity (*e.g.* transferring NCs from toluene to aqueous dispersions) and consequently, involving different ligand motifs various PLQY values can be obtained. They evidenced novel chemical reactions. As an example, less photoluminescent and labile aqueous systems arise from the oxidation of -SH moieties to a disulfide bridge (-S-S-) and further, the desorption of thiolate ligands.

3.2. Interpretation.

Widely-developed production approaches allow recognizing a role of each nanocomposite component in the PL properties. Hence, in order to interpret mechanisms upon photoexcitation, time-resolved emission spectroscopy (TRES) measurements have been carried out. As reported *via* T. Chevallier *et al.* [7], average PL lifetimes received from triple exponential PL decay are strictly associated with an emission wavelength indicating a different contribution of each time component. Correlating spectroscopic results (both TRES and steady-state) with general knowledge about photoluminescence of ternary NCs [23], it turned out that a traditional explanation with two radiative pathways [22] must be improved. In fact, triple-part emission model (**Fig. 3.**) is elaborated involving donor-acceptor pair (DAP) recombinations and another one which is related to defects in the crystalline structure. Accordingly, the PL energy which exhibits a single peak can be approximated by the following formula:

$$E_{emission} = E_g - E_D - E_A + \frac{e^2}{\varepsilon \cdot d} \qquad (1)$$

Where E_g denotes bandgap emission energy, E_D and E_A are energies of donor and acceptor states, ε is the material permittivity, d is a donor-acceptor distance and e charge of an electron. Despite a difference in efficiency, which favors a surface DAP, only PL lifetimes can deserve results allowing to unequivocally distinguish each of recombinations pathways. As result, the lowest component is related to intrinsic radiative transition and the highest, to a core DAP.

4. CONCLUSIONS

Herein, the method of characterization of Zn-Ag-In-S-type NCs was briefly introduced including diverse approaches to design (a pristine AIS, an alloyed ZAIS or a core/shell ZAIS) and preparation routes (based on the use of a single or individual simple precursors) which can be easily modified. Knowing their influence on photophysical properties, the NCs PL can be tuned over a wide range of wavelengths suitable for the biological window or alternative applications. Additionally, large Stokes shifts enable reduction of a negative self-absorption effect and non-radiative resonance energy transfer. Ultimately, the existence of three radiative recombination pathways (such as intrinsic defects and donor-acceptor transitions) were found indicating relations with a core, as well as surface states. A proper understanding of these mechanisms can help in the development of their potential applications.

References

[1] L. Ye, K.-T. Yong, L. Liu, I. Roy, R. Hu, J. Zhu, H. Cai, W.-C. Law, J. Liu, K. Wang, J. Liu, Y. Liu, Y. Hu, X. Zhang, M. T. Swihart, and P. N. Prasad, Nature Nanotechnology **7**, 453 (2012).
[2] A. M. Derfus, W. C. W. Chan, and S. N. Bhatia, Nano Letters **4**, 11 (2004).
[3] Y. Su, Y. He, H. Lu, L. Sai, Q. Li, W. Li, L. Wang, P. Shen, Q. Huang, and C. Fan, Biomaterials **30**, 19 (2009).
[4] B. Mao, C.-H. Chuang, J. Wang, and C. Burda, The Journal of Physical Chemistry C **115**, 8945 (2011).
[5] P. Bujak, Synthetic Metals **222**, 93 (2016).
[6] F. Chandezon, T. Chevallier, and G. Le Blevennec, Nanoscale **8**, (2016).
[7] G. Gabka, P. Bujak, K. Kotwica, A. Ostrowski, W. Lisowski, J. W. Sobczak, and A. Pron, Physical Chemistry Chemical Physics **19**, 1217 (2017).
[8] G. Gabka, P. Bujak, K. Giedyk, A. Ostrowski, K. Malinowska, J. Herbich, B. Golec, I. Wielgus, and A. Pron, Inorganic Chemistry **53**, 5002 (2014).
[9] T. Kameyama, T. Takahashi, T. Machida, Y. Kamiya, T. Yamamoto, S. Kuwabata, and T. Torimoto, The Journal of Physical Chemistry C **119**, 24740 (2015).
[10] Z. Luo, H. Zhang, J. Huang, and X. Zhong, Journal of Colloid and Interface Science **377**, 27 (2012).
[11] G. Manna, S. Jana, R. Bose, and N. Pradhan, The Journal of Physical Chemistry Letters **3**, 2528 (2012).
[12] T.-T. Xuan, J.-Q. Liu, C.-Y. Yu, R.-J. Xie, and H.-L. Li, Scientific Reports **6**, (2016).
[13] S. Jeong, H. C. Yoon, N. S. Han, J. H. Oh, S. M. Park, B. K. Min, Y. R. Do, and J. K. Song, The Journal of Physical Chemistry C **121**, 3149 (2017).
[14] X. Tang, W. B. A. Ho, and J. M. Xue, The Journal of Physical Chemistry C **116**, 9769 (2012).
[15] T. Torimoto, T. Adachi, K. Okazaki, M. Sakuraoka, T. Shibayama, B. Ohtani, A. Kudo, and S. Kuwabata, Journal of the American Chemical Society **129**, 12388 (2007).
[16] J.-Y. Chang, G.-Q. Wang, C.-Y. Cheng, W.-X. Lin, and J.-C. Hsu, Journal of Materials Chemistry **22**, 10609 (2012).
[17] T. Torimoto, S. Ogawa, T. Adachi, T. Kameyama, K. Okazaki, T. Shibayama, A. Kudo, and S. Kuwabata, Chemical Communications **46**, 2082 (2010).
[18] D. K. Sharma, S. Hirata, L. Bujak, V. Biju, T. Kameyama, M. Kishi, T. Torimoto, and M. Vacha, Physical Chemistry Chemical Physics **19**, 3963 (2017).
[19] Y. Hamanaka, K. Ozawa, and T. Kuzuya, The Journal of Physical Chemistry C **118**, 14562 (2014).
[20] S. Jeong, S. Yoon, S. Y. Chun, H. C. Yoon, N. S. Han, J. H. Oh, S. M. Park, Y. R. Do, and J. K. Song, The Journal of Physical Chemistry C **122**, 10125 (2018).
[21] G. Gabka, P. Bujak, K. Giedyk, K. Kotwica, A. Ostrowski, K. Malinowska, W. Lisowski, J. W. Sobczak, and A. Pron, Phys. Chem. Chem. Phys. **16**, 23082 (2014).
[22] M. J. Rao, T. Shibata, S. Chattopadhyay, and A. Nag, The Journal of Physical Chemistry Letters **5**, 167 (2014).
[23] H. Zhong, Z. Bai, and B. Zou, The Journal of Physical Chemistry Letters **3**, 3167 (2012).

OPTICAL PROPERTIES AND APPLICATIONS OF GOLD NANOPARTICLES

K. Nadolski[1], P. Obstarczyk[1], J. Olesiak-Bańska[1*], A. Żak[2], K. Matczyszyn[1]

[1]Advanced Materials Modelling and Engineering Group, Faculty of Chemistry, Wrocław University of Science and Technology, Wybrzeże Wyspiańskiego 27, 50-370 Wrocław, Poland
[2]Electron Microscopy Laboratory, Institute of Materials Science and Applied Mechanics, Wrocław University of Science and Technology, Wybrzeże Wyspiańskiego 27, 50-370 Wrocław, Poland
*e-mail: joanna.olesiak-banska@pwr.edu.pl

Abstract: *Gold nanoparticles exhibit optical response connected with the Localised Surface Plasmon Resonance, which can be modulated in a wide range of wavelengths by changing the nanoparticles shape and size [1]. Many different shapes of nanoparticles can be prepared with wet-chemistry methods, such as nanospheres [2], nanorods [3], nanobipyramids [4] or nanotriangles [5]. In this work, we discuss the process of gold nanoparticles synthesis, their scattering and nonlinear optical properties and applications such as nanoantennas [6] and for bioimaging [7].*

Keywords: *nanoparticles, gold, plasmonics, nonlinear optics*

1. INTRODUCTION

Gold has been a field of interest of humans for ages. It has had the role of showing wealth, affection, it caused plenty of battles and wars [8]. Gold crystals, which size is of nanoscale, are called gold nanoparticles. In this work, we show the process of their fabrication, investigation of their optical properties, as well as present various possibilities of their applications.

2. FABRICATION

Gold nanoparticles can be prepared in different ways, such as condensation of vaporised metal atoms under Ultra High Vacuum conditions, reduction of a solution of gold compound or deposition of a gold compound followed by decomposition or reduction to the metallic state or vaporised gold atoms onto a support [8]. In our laboratory we use the chemical reduction method. The most known method of nanospheres' synthesis is HAuCl4 reduction by a citrate [2], which allows fabrication of nanospheres of 10-20 nm diameter. Citrates' role is reduction, as well as stabilization of the colloid, which hinders the aggregation of the nanoparticles. Most of synthesis protocols of nanoparticles of other shapes are based on the seed-growth method. A solution containing nanospheres (seed) is used for further growth of nanoparticles [3]. Figure 1 presents Transmission Electron Microscopy pictures of gold nanospheres (a), nanorods (d) and bipyramids (g).

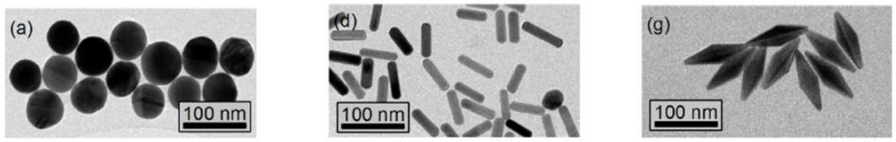

Fig. 1. TEM pictures of gold nanospheres (a), nanorods (d) and bipyramids (g) [9]

3. OPTICAL PROPERTIES

Optical properties of gold nanoparticles are connected with surface plasmons. Plasmon is a quantum of energy associated with an eigenfrequency of a plasma oscillation, meanwhile we can talk about plasma, when a gas of free electric charges moves under the influence of electromagnetic or gravitational force [8].

3.1. Dark-field microscopy

Dark-field microscopy was first used by Zsigmondy around 1900 for analysis of scattering of colloidal gold nanoparticles [10]. In this method, the light is directed in an angle, which does not let it fall directly into the objective (Fig. 2). A dark picture with bright points is obtained. The bright points are objects, which scattered the light. A drawback of this method is that gold nanoparticles are not the only objects, which can be detected, so additional methods of identification must be included. However, the simplest method is to look at the colour of the object, which should correspond to the localization of peaks, for instance a single gold nanorod is usually represented by a red point and a single gold nanosphere by a green point [11], but keep in mind that the shape of a nanoparticle is not the only factor which influences its plasmons' spectral localization - some other important factors are for instance its surrounding medium and pH of the solution [8, 11]. Since the setup used for dark-field microscopy is relatively simple, it is a good method for checking the quality of a sample (e.g. amount of gold nanoparticles, amount of nanospheres, etc.). Hence, the light scattered by gold nanoparticles is strongly polarized, which makes them a good material for polarization microscopes [12].

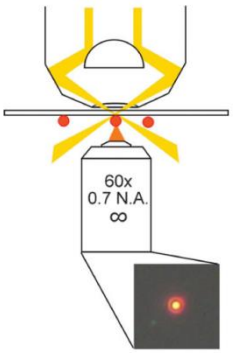

Fig. 2. Illustation of the light propagation in dark-field miscoscopy. The role of the dark-field condenser is to direct the light in such a manner, which does not let it fall directly into the objective [11]

3.2. Nonlinear optical processes in gold nanoparticles

In the classical optics four rules must be fulfilled:

- Optical properties of materials do not depend on the intensity of light.
- There is a superposition rule.
- The frequency of light never changes after passing a medium.
- Two independent light beams cannot interact with each other [13].

In the nonlinear optics, these rules can be broken. The induced polarization does not depend on the electric field linearly anymore [14]. It induces the possibility of absorbing two or more photons at the same time, as well as changing the wavelength of light.

In case of gold nanoparticles, two-photon absorption is easily obtained under femtosecond laser illumination [15]. It is strongest when exciting in the vicinity of the plasmon peak. M. Gordel showed that this effect depends on the shape of the nanoparticles - the Two-photon absorption cross-section is two orders of magnitude higher for nanospheres than for nanorods [16]. The reason of this process are d-sp interband transitions, which is shown in Figure 3.

4. APPLICATIONS

Since it is possible to change the range of light absorbed by gold nanoparticles and plasmon resonance can significantly enhance the local field, they find plenty of applications. Optical antennas are constructed for light conversion. An important parameter is their local field enhancement factor, which can be even a factor of 50 for gold nanoparticles [18].

Gold nanoparticles allow deep tissue penetration, which makes them useful in biology. Adding them to biological systems, allows bioimaging of single cells [7]. Hutter and Maysinger discussed bioimaging of neurons using gold nanorods (Figure 4). Mitochondria within the neurons were labeled with a green dye, which let confirm observations. Red dots in the picture mean imaged gold nanorods.

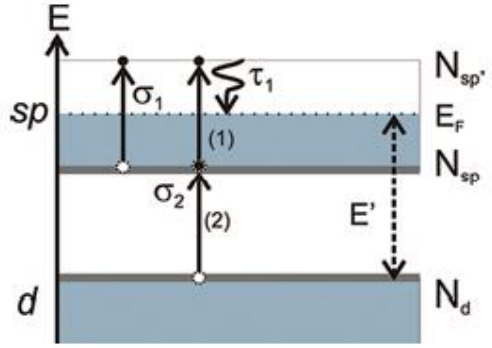

Fig. 3. Band scheme of gold nanorods. E' is an energy of transition from the top of the d band to E_f, E_f is the Fermi level, σ_1 and σ_2 - one- and two photon absorption cross-sections, $\tau_{1\,is}$ the characteristic time for the excited electron thermalization. $N_{sp'}$ and N_{sp} mean concentrations of sp-band electrons above and below E_f. N_d means concentration of electrons in the d band [17]

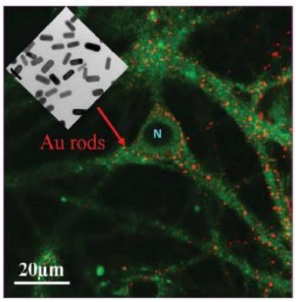

Fig. 4. Neurons imaged using gold nanorods [7]

There are plenty of other possible biological applications of gold nanorods. One of them was reported by T. Labouret [19]. Single gold nanorods, irradiated by a laser in the vicinity of near-IR, induce the production of reactive oxygen species (ROS), including singlet oxygen, which is crucial for Photodynamic Therapy, since it causes necrosis and apoptosis of cells. Aqueos dyhydrorhodamine 123 (DHR) was used as a fluorescent probe for the detection of ROS.

References

[1] U. Kreibig, M. Vollmer, Optical properties of Metal Clusters, Springer, Berlin (1995).
[2] J. Turkevich, P. C. Stevenson, J. Hillier, A study of the nucleation and growth processes in the sythesis of colloidal gold, Discuss. Farady Soc. 11, 55-75 (1951).
[3] J. Olesiak-Banska, M. Gordel, K. Matczyszyn, V. Shynkar, J. Zyss, M. Samoc, Gold nanorods as multifunctional probes in a liquid crystalline DNA matrix, Nanoscale, 5, 10975 (2013).
[4] M. Z. Liu, P. Guyot-Sionnest, Mechanism of silver(I)-assisted growth of gold nanorods and bipyramids, J. Phys. Chem. B 109, 22192-200 (2005).
[5] L. Scarabelli, M. Coronado-Puchau, J. J. Giner-Casares, J. Langer, L. M. Liz-Marzan, Monodisperse Gold Nanotriangles: Size-Control, Large-Scale Self-Assembly, and Performance in Surface-Enhanced Raman Scattering, ACS Nano, 8 (6), 5833-5842 (2014).
[6] P. Bharadwaj, B. Deutsch, L. Novotny, Optical antennas, Adv. Opt. Photon. 1, 438-483 (2009).
[7] E. Hutter, D. Maysinger, Gold Nanoparticles and Quantum Dots for Bioimaging, Microscopy research and technique 74, 592-604 (2011).
[8] C. Louis, O. Pluchery, Gold nanoparticles for physics, chemistry and biology, Imperial College Press (2012)
[9] S. M. E. Peters, M. A. Verheijen, M. W. Prins, P. Zijlstra, Strong reduction of spectral heterogeneity in gold bipyramids for single-particle and single-molecule plasmon sensing, Nanotechnology 27 (2016).
[10] S. Schultz, D. R. Smith, J. J. Mock and D. A. Schultz, Single-target molecule detection with nonbleaching multicolor optical immunolabels, Proc. Natl. Acad. Sci. U. S. A., 97, 996–1001 (2000)

[11] M. Hu, C. Novo, A. Funston, H. Wang H. Staleva, Sh. Zou, P. Mulvaney, Y. Xia, G. V. Hartland, Dark-field microscopy studies of single metal nanoparticles: understanding the factos that influence the linewidth of the localized surface plasmon resonance, J. Mater. Chem., 18 (17), 1949-1960 (2008)
[12] J. Olesiak-Banska, M. Gordel, K. Matczyszyn, V. Shynkar, J. Zyss, M. Samoc, Gold nanorods as multifunctional probes in a liquid crystalline DNA matrix, Nanoscale, 5, 10975 (2013).
[13] B. E. A. Saleh, M. C. Teich, Fundamentals of Photonics, Second Edition, John Wiley & Sons, Inc., Hoboken (2007).
[14] M. Born and E. Wolf, Principles of Optics: Electromagnetic Theory of Propagation, Interference and Diffraction of Light, Cambridge University Press, Cambridge (1999).
[15] J. Olesiak-Bańska, Dyes and nanoparticles as biolabels in two-photon microscopy of liquid crystalline DNA, A Dissertation Submitted to Faculty of Chemistry at Wroclaw University of Technology For the Degree of Doctor of Chemistry, Wrocław (2012).
[16] M. Gordel, R. Kolkowski, J. Olesiak-Banska, K. Matczyszyn, M. Buckle, M. Samoć, Z-scan studies of nonlinear optical properties of colloidal gold nanorods and nanoshells, Journal of Nanophotonics, 9 (1), 093797, (2014).
[17] J. Olesiak-Banska, M. Gordel, R. Kolkowski, K. Matczyszyn, M. Samoc, Third-Order Nonlinear Optical Properties of Colloidal Gold Nanorods, J. Phys. Chem. 116, 13731 (2012).
[18] M. Z. Liu, P. Guyot-Sionnest, T. W. Lee, S. K. Gray, Optical properties of rodlike and bipyramidal gold nanoparticles from three-dimensional computations, Phys. Rev. B 76, 235428 (2007).
[19] T. Labouret, J-F. Audibert, R. B. Pansu, B. Palpant, Plasmon-Assisted Production of Reactive Oxygen Species by Single Gold Nanorods, Small 11, 4475-4479 (2015).

APPLICATIONS OF THE CHARGE TRANSFER PHENOMENON OCCURRING IN HYBRID SEMICONDUCTOR-METAL NANOSYSTEMS

K. Nawrot*, D. Wawrzyńczyk, M. Nyk

Advanced Materials Engineering and Modelling Group,
Faculty of Chemistry, Wrocław University of Science and Technology,
Wybrzeże Wyspiańskiego 27, 50-370 Wrocław, Poland
*e-mail: katarzyna.nawrot@pwr.edu.pl

Abstract: *Semiconductor nanoparticles have gained a great deal of interest in energy storage and conversion applications, due to their ability of photoinduced charge separation. However, semiconductor nanoparticles usually display fast recombination of charge carriers. Deposition of metal nanostructures onto semiconductor nanoparticles surface has been widely proved to increase charge separation yield. In the presence of light, these hybrid nanosystems are thus able to efficiently support photo-induced, electrons-including processes. Therefore, they are promising materials for emerging applications such as next-generation solar cells, hydrogen or reactive oxygen species generation and microelectronic devices.*

Keywords: nanomaterials, photocatalysis, photocurrent generation, quantum dots

1. INTRODUCTION

Semiconductor nanoparticles, i.e. quantum dots (QDs) have been demonstrated to support charge-driven processes, as upon light excitation they undergo charge separation between their valence band and conduction band. In this way, electrons and holes may be exploited in such processes as current flow, energy conversion and redox reactions, and applied in electronic devices, photovoltaic cells and photocatalysis. However, the charge separation efficiency in simple semiconductors is low and it is followed by fast recombination of electrons and holes [1]. Profitability of their usage is thus limited. Combination of semiconductor nanoparticles with any electron-trapping materials have been proposed as a solution for the inefficiency problems. Metals, as strong electron acceptors, fulfil this function excellently. Nevertheless, semiconductor-metal junction in macroscale is a problematic one due to depletion layer formation at the interface between the materials which impede electron transfer. For this reason, nanometer size particles are employed to limit barrier generation.

2. CHARGE TRANSFER PHENOMENON

Figure 1. illustrates the principle of charge transfer phenomenon mechanism at the nanoscale semiconductor-metal interface. In case of junctions between metals and bulk n-type semiconductors, a depletion layer (also called space charge region) forms at the interface between two materials thus impeding electron transfer from the semiconductor conduction band into the metal. However, reduction of the semiconductor particle size down to nanometer scale, makes them sufficiently smaller than the space charge region thus inhibiting depletion layer formation. Therefore, the kinetics of electrons transfer is almost

not disturbed. Free diffusion of charge carriers allows electrons to travel to the metal nanoparticles within about 0.1 ps, and thus may exceed the rate of recombination processes [2].

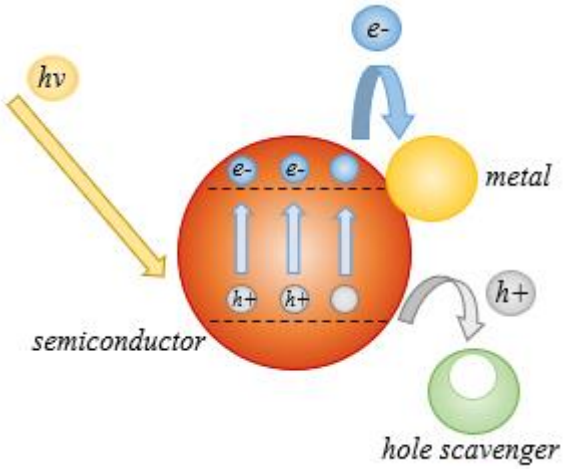

Fig. 1. Schematic representation of charge transfer phenomenon occurring in a hybrid semiconductor-metal nanosystem

The choice of a semiconductor-metal pair comes down to selecting a metal with Fermi level embraced within the band gap of given semiconductor. Moreover, the material should be suitable for desired application. Among the most popular heterostructures, nanomaterials such as ZnO [1], CdSe [3], CdS [4] and TiO_2 [5] combined with noble metals (e.g. gold, silver or platinum) gain a great deal of interest. Not only the composition type of the material but also the size and shape of both semiconductor and metal nanoparticle influence efficiency of desired charge transfer phenomenon. For example, instead of QDs, nanorods with metal nanostructures grown at their tips are willingly used because their shape ensures better charge separation [3]. Moreover, the size of metal nanoparticles plays an important role as the larger ones possess higher density of states in Fermi lever and therefore electron transfer is facilitated [4].

Not only support for electrons transfer but also a trap for the remaining holes is an efficient strategy to improve the charge separation process. For this purpose, so called hole scavengers are added to colloidal solution of the hybrid semiconductor-metal system. The most popular hole scavengers are low molecular weight alcohols such as methanol or ethanol [3]. However new routes proposed by Hippargi et al. [6] are investigated in order to maximize charge separation efficiency using electron-driven hydrogen evolution rate when chloride ions were engaged as hole scavengers.

3. APPLICATONS

The charge transfer between semiconductor QDs and metal results in charge separation promoting electron-dependent processes, including such emerging ones as current generation or water splitting. Studies on longer and more efficient charge separation enables development of photovoltaic cells as well as other electronic devices and photocatalysis of reduction and oxidation reactions led by hydrogen and oxygen generation. Some of the possible applications of nanomaterials showing efficient charge separation are briefly discussed below.

3.1. Electronic devices

As the hybrid semiconductor-metal nanosystems are able to transfer electrons within their structures, they are willingly investigated through application in electronic devices. Lavieville et al. [7] proposed a simple electrical setup applying CdSe nanorods linked to each other by gold nanoparticles deposited onto electrodes structures by dielecrophoresis. As-prepared networks showed appreciable conductivity with strongly nonlinear characteristic while no current was detected when only nanorods (without Au bridges) were deposited onto the electrodes.

3.1.1. Photovotaic cells

Enhancement of solar cells efficiency in order to improve profitability of using them, disseminate energy generation from sunlight and displace conventional energy sources is currently one of the most important scientific problems. Application of the semiconductor-metal nanosystems providing enhanced light-driven charge transfer into photovoltaic cells seems to be an ideal way to produce new generation solar panels. Dhas et al. [8] reported power conversion efficiency augmentation in the solar cells based on ZnO nanoflowers doped with Au nanoparticles in comparison to the system with undoped QDs.

3.2. Photocatalysis

Conversion of the solar energy into chemical energy by semiconductor-metal nanosystems is even more widely investigated than their application in third-generation photovoltaic cells. The photocatalytic activity of the nanohybrids is due to electron and holes separation which are essential in redox reactions – reduction and oxidation respectively.

3.2.1. Reduction reactions and hydrogen generation

After charge separation, which is the result of light absorption by semiconductor nanoparticle and electron transfer into metal, the electron may take part in reduction reactions. The ability of the hybrid systems to promote reduction have been widely proved with UV-VIS absorption spectroscopy of different dyes which absorbance is bleached after transformation to their reduced form. For instance, Dana et al. [4] demonstrated *rhodamine B* absorption bleaching when exposed on sunlight in the presence of CdSe@CdS-Au nanoheterostructures. Another example, published by Costi et al. [3], shows consistent reduction of *methylene blue* absorption activity during irradiation in the presence of CdSe nanorods terminated with Au tips.

Hydrogen may be produced in the same way via water splitting as this process involves electrons. Zhang et al. [5] successfully performed hydrogen generation after irradiation of

hybrid TiO_2-Au nanosystems dispersed in water with addition of methanol as a hole scavenger. Hydrogen evolution from the hybrid systems is significantly higher in comparison to TiO_2 or Au alone.

3.2.2. Reactive oxygen species (ROS) generation

While separated electrons may take part in reduction reactions, the remaining holes make excellent conditions for oxidation reactions. Reactive oxygen species (ROS) formed via water splitting and from dissolved oxygen in the presence of positively charged holes are widely known as factors causing oxidative stress in cells and therefore may serve as antimicrobial agents or in anti-tumour therapies. As an example, He et al. [1] prepared ZnO-Au nanosystems, which enabled both photo-reduction reactions as well as ROS generation. In the second case, both hydroxyl radicals and singlet oxygen were detected via electron spin resonance technique. Moreover, those authors suggested that the type of generated ROS may be designed by the choice of semiconductor with proper bandgap. ZnO, with valence band redox potential of 3.0V and conduction band redox potential of -0.2V, promotes hydroxyl radicals generation more efficiently than singlet oxygen production probably because there is a higher redox potential difference between the $H_2O/OH•$ couple and valence band edge than between $O_2/O_2•^-$ and conduction band (Figure 2).

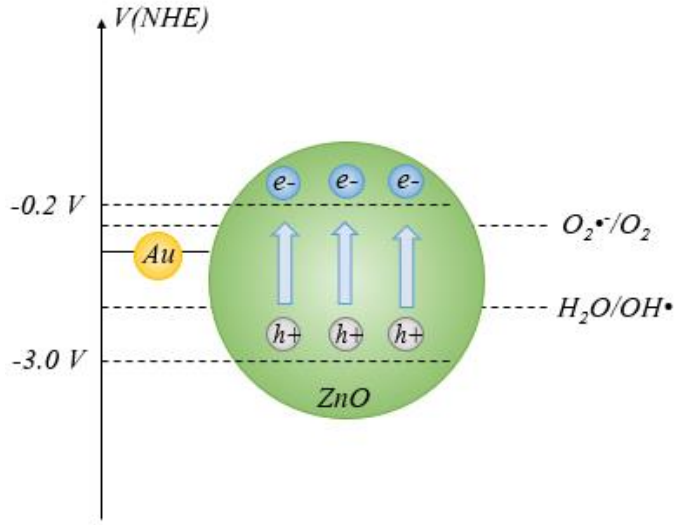

Fig. 2. Energy bands of ZnO and position of Au Fermi level
comparing to redox potential of $O_2^{\bullet-}/O_2$ and $H_2O/OH^{\bullet}$ (on the basis of [1])

4. CONCLUSIONS

Combination of semiconductor quantum dots and metal nanocrystals into single hybrid heterostructures provides efficient path for electron transfer in the direction of metal which is able to compete with recombination process. The separated charges are ready to support current flow as well as electron- and hole-driven chemical processes, thus opening a wide range of possible optoelectronic applications. Hybrid semiconductor-metal nanosystems have been reported to be successfully applied as current generation networks, power converters in model solar cells and water splitting photocatalysts for production of hydrogen and reactive oxygen species. Their properties may be designed directly for specific applications by choosing a semiconductor with desired energy bandgap as well as suitable composition, sizes and shapes of both semiconductor and metal nanoparticles.

References

[1] Weiwei He et al., *J. Am. Chem. Soc.* 136, 750-757 (2014)

[2] Wood A., Giersig M., Mulvaney P., *J. Phys. Cem. B* 105, 8810-8815 (2001)

[3] Costi R., Saunders A.E., Elmalem E., Salant A., Banin U., *Nano Lett.* 8, 637-641 (2008)

[4] Dana J., Maity P., Ghosh H.N., *Nanoscale* 9, 9723-9731 (2017)

[5] Zhang J. et al., *ACS Nano* 10, 4496-4503 (2016)

[6] Hippargi G., Mangrulkar P., Chilkalwar A., Labhsetwar N., Rayalu S., *Int. J. Hydrogen Energy* 43, 6815-6823 (2018)

[7] Lavieville et al., *ACS Nano* 6, 2940-2947 (2012)

[8] Dhas V., Muduli S., Lee W., Han S.-H., Ogale S., Appl. Phys. Lett. 93, 243108 (2008)

SOL-GEL LAYERS IN MICROELECTRONIC APPLICATIONS

W. Nawrot*, K. Malecha

Faculty of Microsystem Electronics and Photonics, Wrocław University of Science and Technology, Wyb. Stanisława Wyspiańskiego 27, 50-370 Wrocław, Poland
*e-mail: witold.nawrot@pwr.edu.pl

Abstract: *This work mainly regards the modification of sol-gel coatings with nanomaterials and their application in Low Temperature Cofired Ceramic (LTCC) technology. They can be used for surface smoothing for thin film deposition and microfluidics. Moreover, optical waveguides can be composed of this material for interconnections in microdevices. The benefit of doping with different nanomaterials is described with examples. Authors describe i.a. applications in the field of photonics, biosensors and photocatalytic microreactors.*

Keywords: sol-gel, nanocomposites, nanoparticles, ceramics, LTCC, photonics

1. INTRODUCTION

The sol-gel technology can be originated in mid XIX century; however, new materials and applications still emerge. The process is based on metal-organic precursors which hydrolyse and condensate to form a sol. Subsequently, the gelling phase takes place, in which a layer can be deposited on a substrate. This gel layer is densified and fixed to the substrate during sintering. A significant shrinkage occurs, due to evaporation of liquid contents. As a result, mechanical stress may appear which introduces a risk of cracking. The formation of the glass is based on a cross-linking mechanism; therefore, the technique does not require the use of high-temperature processing, in contrast to traditional melting-based glass manufacturing methods. Application methods for sol-gel, such as screen printing, spin coating and dip-coating are cost-efficient and relatively easy. Thus, the process is well suited for integration in thick film and ceramic technologies, highly increasing their abilities, as shown in next chapters.

2. APPLICATION IN SURFACE SMOOTHING

The most common application of sol-gel layers is modification of surface properties, for instance to prevent corrosion. In microelectronics, an important parameter limiting process resolution is surface roughness. It has the biggest impact in Low Temperature Cofired Ceramic (LTCC) technology. Process of producing such substrates starts with mixture of ceramic, glass, organic fillers and a solvent. They are deposited on polymeric film in a process called tape casting. The thickness of resulting so called green tape is guarded by a doctor blade and ranges from 50 μm to 250 μm after drying. Then, a series of treatments can be applied to the tape, including laser cutting and deposition of patterns: conductive, resistive, dielectric, semiconductive, sensoric and biological. Afterwards, a series of layers can be stacked together forming a spatial module, similarly to 3D-printig technology. The tapes are laminated together at high pressure in the range of 10-30 MPa and elevated temperature (50-90 °C) to compose a uniform structure. The last step is firing

with peak temperature at about 850 °C, where the glass is soft and runs around ceramic particles. The surface quality of resulting glass-ceramic composite depends highly on the particle size and the lamination process. Generally though, it is not sufficient for reliable deposition of thin film layers, due to significant waviness and roughness. As shown in fig. 1, the difference between the two is characteristic dimension. Waviness is in scale with deposited patterns and may distort them. On the other hand, roughness is a phenomenon at least 10 times smaller and may entail local discontinuities in deposited patterns, which can result in increase of resistance or even breaks.

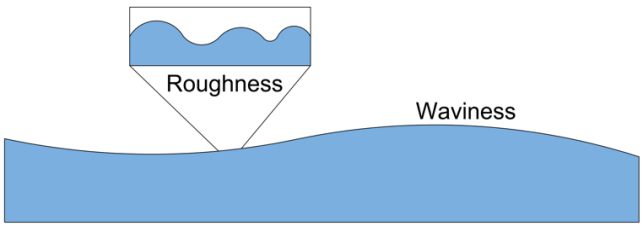

Fig. 1. Diagram of LTCC surface, depicting key parameters

In [1] authors proved that sol-gels can reduce LTCC roughness. Moreover, they indicated that thick layers provide higher improvements, as they better fill in surface valleys (fig. 2). Unfortunately, they found out that upscaling also increases the risk of cracking. They proposed a solution in form of doping with silica nanoparticles (SiO_2 NPs). Such nanocomposite reduces the strain in the structure. The use of suspensions filled with nanoparticles reduces shrinkage and enables formation of thicker layers in one coating step, while decreasing the risk of cracking.

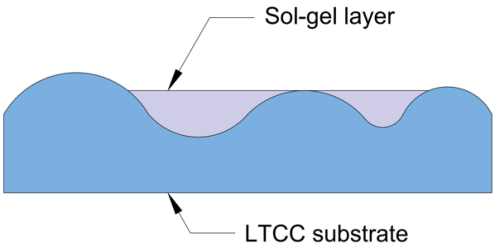

Fig. 2. Sol-gel layer roughness smoothing

Another issue with surface roughness in LTCC technology regards microfluidic devices. Authors in [2] have shown that analysed solution may leave deposit on the channel surface, even after rinsing with deionised water. This causes unrepeatability of results obtained in the microchip in subsequent measurements. It not only restricts multiple use of the device, increasing the cost of use, but also decreases reliability of the results in the first run, as deposition makes the fluid flow not uniform, which is crucial in optical devices. One of possible results may be response increase due to analyte aggregation. It has been shown by the authors that this issue can be remedied by sol-gel coatings which prevent adsorption of

particles. After such surface modification, the measurements have been proven to be repeatable.

3. APPLICATION IN SENSORS AND PACKAGING

Sol-gel layers are commonly transparent: the most popular material, tetraethyl orthosilicate (TEOS), forms in to SiO_2, an optically desirable compound. Therefore, one of appealing applications is in optical planar waveguides. They could be foremost used as interconnections in optoelectronic devices and microfluidic sensors [3]. However though, two basic principles have to be satisfied in order for the light to propagate inside the structure. First, a material with different refractive index has to surround the core sol-gel layer to form a cladding. That could be a glaze layer or another sol-gel, as this parameter can be modified by dopants such as titanium dioxide (TiO_2). Secondly, the core has to be sufficiently thick. As mentioned in previous chapter this could be achieved by addition of nanoparticles. The SiO_2 NPs used in [1] are very suitable in this application as they exhibit exemplary optical performance.

An interesting development of this of this idea is implementation of metallic nanoparticles into a waveguide. Due to plasmon interactions, such layers can be used to inspect substances, as a progression of Surface Enhanced Raman Spectroscopy (SERS). In typical setup, an analyte placed on metallic substrate is irradiated and the amount of Raman scattering is measured, as shown in fig. 3a. In order to increase sensitivity of analysis, metallic nanostructures are used instead of bulk metal, as plasmonic interactions are amplified in nanoscale (fig. 3b). A sol-gel matrix with nanoparticles can further improve the sensitivity as the surface to volume ratio is maximised (fig. 3c). Authors in [4] have proven that it is possible to obtain an even dispersion of gold nanoparticles (Au NPs) in sol-gel matrix by simple method. They further shown that it is possible to use such nanocomposite for SERS and investigate analyte present on the surface in a setup shown in fig 3c. Moreover, such photonic waveguide allows simplification in measurement setup, where an increase in absorbance (fig. 3d) due to interaction of analyte with evanescent field is being measured. Such photonics waveguide can be used in microfluidic systems, as shown by authors in [5]. In LTCC devices the sol-gel would have two functions: one, as smoothing layer for good repeatability and second, as a photonic waveguide. LTCC microchips have already been proven to be more than suitable for microfluidics [6-8].

Metallic nanoparticles can also have other applications in sol gel layers. Some of them, such as gold, exhibit high affinity to wide variety of substances and can be used as attachment centres for enzymes or other biologically active layers for biosensor manufacturing. In [9] an AuNP-doped zinc oxide (ZnO) based sol-gel layer has been used to attach bovine serum albumin (BSA) protein and form an electrochemical erythropoietin (EPO) hormone sensor. Zinc oxide sol-gel nanocomposites can also be used for gas sensing with great results, as shown in [10-12]. This material is also known for photocatalytic properties, which can be used for water purifying and antibacterial purposes [13] and even hydrogen generation [14]. A photocatalytic microreactor based have been already shown [15]. The photocatalytic properties have been also proven in sol-gel embedded ZnO NPs [16, 17]. All presented examples prove that original properties of material stay intact after incorporation in sol-gel matrix.

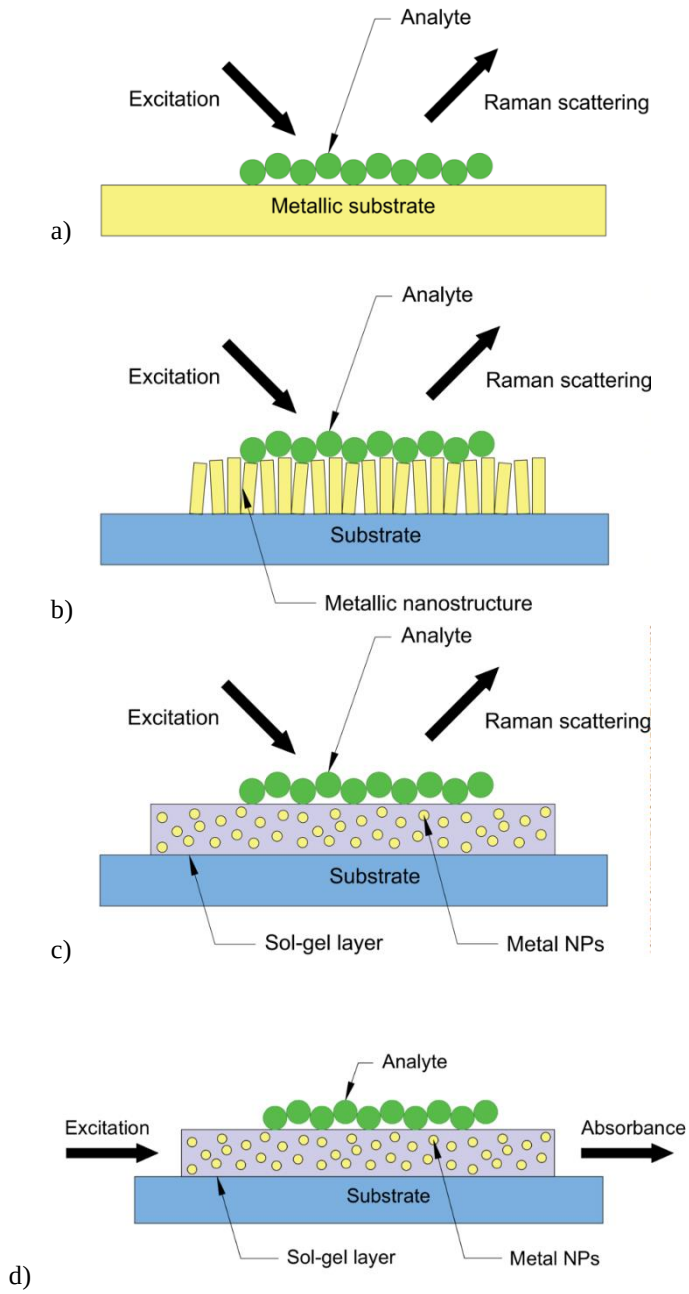

Fig. 3. Surface Enhanced Raman Spectroscopy setups: a) original, with metallic substrate, b) with improved sensitivity by metallic nanostructures, c) with sol-gel embedded nanostructures for higher interaction volume, d) with nanocomposite and simplified measurement

4. SUMMARY

Applications presented in this paper show that sol-gel layers present great possibilities. Especially interesting is combination with thick film and ceramic technologies, into which it can seamlessly integrate. On one hand the sol-gel improves quality of ceramic devices, on the other LTCC can provide a perfect packaging for photonic structures, with microfluidic canals and optoelectronic devices onboard. The manufacturing processes are already compatible, which is a further benefit. Moreover sol-gel layers can replace thick film in certain application with great result. It could increase system durability for wide range of sensors and active devices.

Acknowledgement

This work has been supported by statutory funds of Faculty of Microsystem Electronics and Photonics, Wrocław University of Science and Technology.

References

[1] H. Bartsch, U. Brokmann, B. Goj, R. Weiss, E. Rädlein, J. Müller, In *Proceedings of 2015 European Microelectronics Packaging Conference (EMPC)*, Friedrichshafen, Germany, pp. 1–6 (2015)

[2] M. Czok, L. Golonka, In *Proc. SPIE 10161, 14th International Conference on Optical and Electronic Sensors* (2016)

[3] R. J. Tadaszak, A. Łukowiak, L. J. Golonka, S. Patela, *Optica Applicata* 41, 493-500 (2011)

[4] A. P. Budnyk, S. O. Cherkasova, A. Damin, *Mendeleev Communications* 27(5), 531-534 (2017)

[5] S. Elmaghrum, A. Gorin, R. K. Kribich, B. Corcoran, R. Copperwhite, C. McDonagh, M. Oubaha, *Sensors and Actuators B: Chemical* 177, 357-363 (2013)

[6] K. Malecha, L. J. Golonka, *Microelectronics Reliability* 48(6), 866-871 (2008)

[7] K. Malecha, L. J. Golonka, *Microelectronics Reliability* 49(6), 585-591 (2009)

[8] K. Malecha, T. Maeder, C. Jacq, *Journal of the European Ceramic Society* 32(12), 3277-3286 (2012)

[9] L. Zhang, Y. Wang, J. Wang, J. Shi, K. Deng, W. Fu, *Biosensors and Bioelectronics* 50, 217-223 (2013)

[10] D. Nesheva, V. Dzhurkov, I. Stambolova, V. Blaskov, I. Bineva, J. M. Calderon Moreno, S. Preda, M. Gartner, T. Hristova-Vasileva, M. Shipochka *Materials Chemistry and Physics* 209, 165-171 (2018)

[11] A. R. Nimbalkar, M.G. Patil, *Physica B: Condensed Matter* 527, 7-15 (2017)

[12] H. J. Al-Asedy, N. Bidin, S. A. Al-khafaji, H. Bakhtiar, *Materials Science in Semiconductor Processing* 77, 50-57 (2018)

[13] M. Fiedot-Toboła, I. Maliszewska, O. Rac-Rumijowska, P. Suchorska-Woźniak, A. Lewińska, H. Teterycz, *Materials* 10(4), 353 (2017)

[14] X. Wang, C. Zhou, W. Wang, B. Du, J. Cai, G. Feng, R. Zhang, *Journal of Alloys and Compounds* 747, 826-833 (2018)

[15] W. Nawrot, M. Fiedot-Toboła, K. Malecha, *IEEE Proc. of 21st European Microelectronics and Packaging Conference (EMPC), Warsaw, Poland (2017)*

[16] D. Heggo, S. Ookawara, *Chemical Engineering Science* 169, 67-77 (2017)

[17] M. L. Satuf, J. Macagno, A. Manassero, G. Bernal, P. A. Kler, C. L. A. Berli, *Applied Catalysis B: Environmental* 241, 8-17 (2019)

Study of the etched pattern geometry change during RIE of nitrides

S. Owczarzak*, A. Stafiniak, R. Paszkiewicz

Faculty of Microsystem Electronics and Photonics, Wrocław University of Science and Technology, Janiszewskiego 11/17, 50-372 Wrocław, Poland

*e-mail: Slawomir.Owczarzak@pwr.edu.pl

Abstract: *Design of semiconductor devices requires accurate prediction of etched mesa structures planar dimensions. For fabrication of GaN electronic devices, the reactive ion etching process in capacity coupled plasma is typically applied using chlorine plasma. The planar dimensions of etched GaN mesas obtained after reactive ion etching process differ from the dimensions of mesas defined by photolithography mask. Therefore for the improvement of design devices shape and dimensions accuracy, the calculation of the influence of pattern dimensions on etched mesas dimensions is critical. In this article the results of the research on influence of the photolithography pattern dimensions on GaN mesas planar dimensions, obtained after reactive ion etching in chlorine based plasma using hard SiO_2 masks are presented and discussed.*

Keywords: RIE, chlorine plasma, GaN

1. INTRODUCTION

Design of semiconductor devices requires taking into consideration of the influence of technological issues that are present during fabrication of structures. One of the technological processes that has significant impact on geometry of obtained structures is reactive ion etching (RIE). Obtaining of the structures with designed geometry requires, during RIE process, taking into consideration the effects such as: micro-loading [1, 2, 3], RIE-lag [4], ARDE (Aspect Ratio Dependent Etching) [5, 6, 7]. The RIE process is applied for transistors fabrication [8, 9], therefore the control of the obtained structures geometry is the important factor of the fabrication process of the transistor [10, 11].

2. EXPERIMENT

The subject of study were GaN structures on which 300 nm SiO_2 layers were deposited using Plasma Enhanced Chemical Vapour Deposition (PECVD), then patterned using photolithography technique with positive resist, and submitted to the RIE process in chamber equipped in chlorine, Capacity Coupled Plasma. In Table 1 the studied RIE recipes are presented. In case of recipe number 1, total flow of reactive gases was 15 sccm, and RF power was 170 W. In case of recipe number 2, total flow of reactive gases was 25 sccm and RF power was 250 W. All studied RIE processes were conducted at temperature 7 ^{o}C and pressure 15 mTorr. The GaN structures were measured using Scanning Electron Microscopy (SEM) HITACHI. The SEM images of obtained structures are presented in

Figure 1, structures etched using recipe no. 1 a) and using recipe no. 2 b) c) d), processed during 12 min b) and during 18 min a) c) d).

Table 1.				
Recipe no.	Temperature [^{o}C]	Pressure [mTorr]	$Ar/BCl_3/Cl_2$ [sccm]	RF Power [W]
1	7	15	5/5/5	170
2	7	15	5/4/16	250

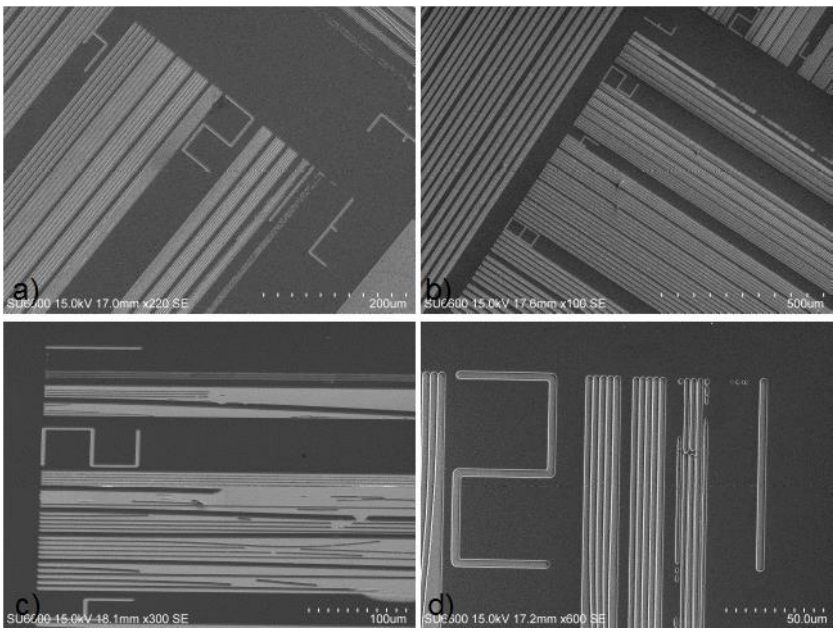

Fig. 1. SEM images of structures etched using recipe no. 1 a) and no. 2 b) c) d) structures etched during 12 min b) and 18 min a) c) d)

In Figure 2 a) the influence of pattern width on structures width, obtained after RIE process during 18 min using recipe number 1 is presented. Dependence in Figure 2 a) is descried by polynomial Eq. (1). In the Figure 2 b) is presented variation of structures width in function on pattern width. The most increased structures width cover the range of 2 to 4 μm pattern width. The biggest variation of obtained trenches width was 1.1 μm. In the Figure 3 a) is presented the influence of pattern width on structures width, obtained after RIE process during 12 min using recipe number 2. Dependence in Figure 3 a) is descried by polynomial Eq. (2). Dependence of structures width from pattern width in this case is the most linear. In the Figure 3 b) is presented the variation of structures width in function of pattern width. The variation of trenches width increased with the etched pattern width, and the biggest variation of obtained structures width was 1.1 μm.

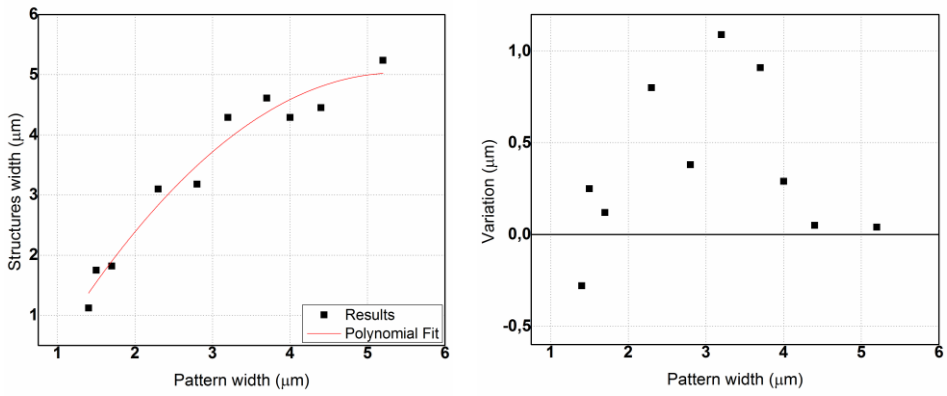

a) b)

Fig. 2. Structures width a) and variation of structures width b) in function of pattern width obtained using recipe no. 1 during 18 min

$$Y=-0.23x^2+2.48x-1.65 \quad (1)$$

Where *Y* is trenches width and *x* is pattern width.

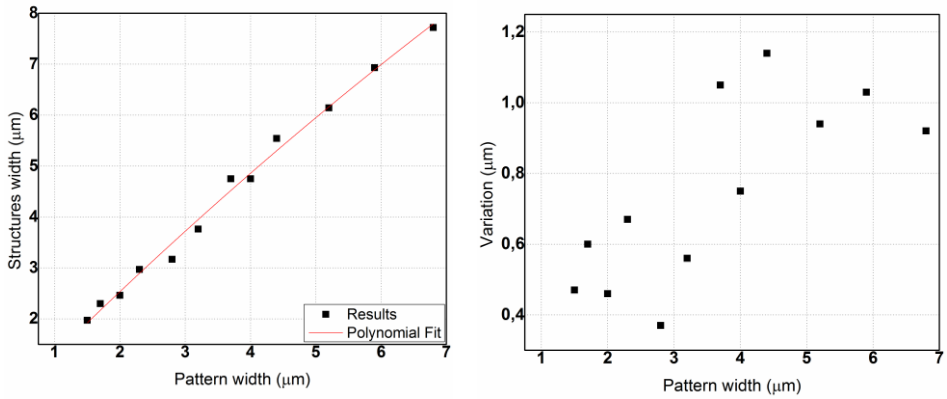

a)

Fig. 3. Structures width a) and variation of structures width b) in function of pattern width obtained using recipe no. 2 during 12 min

$$Y=-0.02x^2+1.3x+0.02 \quad (2)$$

In Figure 4 a) the influence of pattern width on structures width, obtained after RIE process during 18 min using recipe number 2 is presented. Dependence in Figure 4 a) is descried by polynomial Eq. (3). In the figure 4 b) is presented variation of obtained trenches width in function on pattern width. The width of trenches etched via pattern with a width of less than 3.5 μm were increased, but the width of trenches etched via pattern with a width of wider than 3.5 μm were decreased.

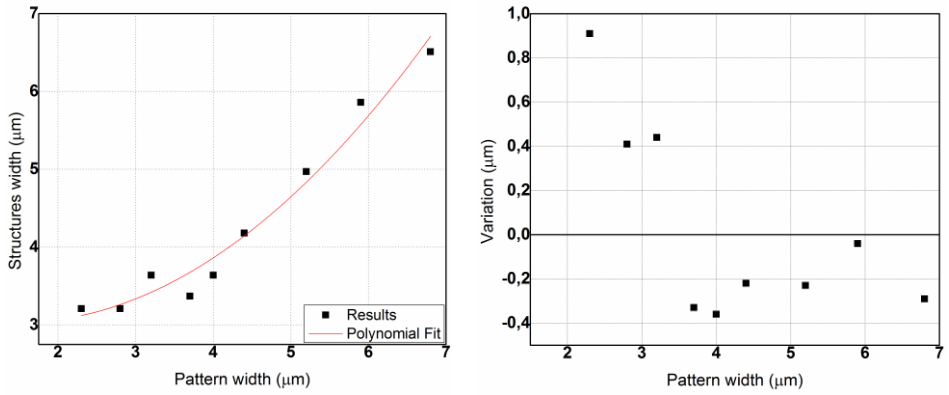

a)

Fig. 4. Structures width a) and variation of structures width b) in function of pattern width obtained using recipe no. 2 during 18 min

$$Y=0.12x^2-0.37x+3.3 \quad (3)$$

3. CONCLUSIONS

The function of structures width and pattern width, in case of trenches obtained during RIE process equipped in Capacity Coupled Plasma module depend from used recipe and designed etch depth of structures. Design of the mask for RIE process requires determination of separate function for each case of RIE recipes and process duration. In the presented study, polynomial equation were appointed for two recipes, and for two different duration of RIE process. It was observed that the function of trenches width and pattern width was most linear after RIE process during 12 min at conditions 7 ºC, 15 mTorr, 5/4/16 sccm of Ar/BCl_3/Cl_2 flow and 250 W of RF power. However, in this case the difference between trenches and pattern width was increased with the etched pattern width.

Acknowledgement

This work was co-financed by the National Centre for Research and Development grants TECHMATSTRATEG No.1/346922/4/NCBR/2017, the National Science Centre grant No. DEC-2015/19/B/ST7/02494, Wroclaw University of Technology statutory grants and by the Slovak-Polish International Cooperation Program. This work was accomplished thanks to the product indicators and result indicators achieved within the projects co-financed by the European Union within the European Regional Development Fund, through a grant from the Innovative Economy (POIG.01.01.02-00-008/08-05) and by the National Centre for Research and Development through the Applied Research Program Grant No. 178782 and Grant LIDER No. 027/533/L-5/13/NCBR/2014.

References

[1] [1] H. Jansen, M. de Boer, J. Burger, R. Legtenberg, and M. Elwenspoek, Microelectronic Engineering 27 (1095) 475-480
[2] [2] C. Hedlund, H. O. Blom, and S. Berg, J. Vac. Sci. Technol. A 12, 1962 (1994)
[3] [3] S.-i. Kato, M. Sato, and Y. Arita, J. Vac. Sci. Technol. A 12, 1204 (1994)
[4] [4] Y. H. Lee and Z. H. Zhou, J. Electrochem. Soc., Vol. 138, No. 8, August 1991
[5] [5] R. J. Xie, J. D. Kava, and M. Siegel, J. Vac. Sci. Technol. A 14, 1067 (1996)
[6] [6] R. A. Gottscho, C. W. Jurgensen, and D. J. Vitkavage, J. Vac. Sci. Technol. B 10, 2133 (1992)
[7] [7] D. S. Tezcan, K. De Munck, Nga Pham, Ole Luhn, Arno Aarts, Piet De Moor, Kris Baert and Chris Van Hoof, Proc. of 2006 Electronics Packaging Technology Conference 22-28
[8] [8] W. Zhang, S. Y. Chou, Appl. Phys. Lett. 83, 1632 (2003)
[9] [9] L. Guo, P. R. Krauss, and S. Y. Chou, Appl. Phys. Lett. 71, 1881 (1997)
[10] [10] V. Kumar, W. Lu, F.A. Khan, R. Schwindt, E, Piner, I. Adesida, ELECTRONICS LETTERS 22nd November 2001 Vol. 37 No. 24
[11] [11] W. B. Lanford, T. Tanaka, Y. Otoki, I. Adesida, ELECTRONICS LETTERS 31st March 2005 Vol. 41 No. 7

LAB-ON-CHIP PLATFORM FOR CULTURING AND INVESTIGATION OF CELLS BEHAVIOUR

A. Podwin*, D. Lizanets, W. Kubicki, P. Śniadek, R. Walczak, J. Dziuban

Faculty of Microsystem Electronics and Photonics, Wrocław University of Science and Technology, Janiszewskiego 11/17, 50-372 Wrocław, Poland
e-mail: a.podwin@pwr.edu.pl

Abstract: *The work presents universal microfluidic lab-on-chip platform dedicated to long-term culturing and investigation of microbial objects different taxis effects. The platform integrates mostly authorial solutions including lab-on-chip devices, microflow regulator for delivery of fresh nourishment and real-time tracking software, ensuring parametric evaluation of the cultures. All-glass lab-on-chip – a key element of the platform, has been fabricated utilizing innovative techniques of xurography and low-temperature (80 ºC) fusion bonding. Experiments conducted on the platform demonstrated a suitable – consistent with the literature data – development of the microbial objects cultures (microorganisms, cells, oocytes). Moreover, interesting chemotaxis and phototaxis phenomena have been investigated, revealing, e.g. euglena positive taxis towards air, instead of N_2. OLED illuminated sample in turn, has shown euglena notable degradation during blue light illumination (470 nm). The results of the tests confirm high platform utility and suggest its further applications.*

Keywords: lab-on-chip, microfluidics, cell culture

1. INTRODUCTION

The popularity of lab-on-chip devices in the biomedical study has recently significantly grown. Due to several important features of these microfluidic systems, i.e. high throughput process control and automation, fast analysis and response time or possibilities to apply innovative methods enabling reliable cells screening and evaluation (e.g.: LIF – *laser induced fluorescence*, FACS – *fluorescence activated cells sorting*), lab-on-chips become especially useful tools for the fields of cell culturing and cytometry [1-3].

Typically, cell cultures are established in a microscale, stationary containers – Petri dishes or culture flasks [4-5]. Nevertheless, these tools apart from being traditional and well-standardized solutions, do not constitute appropriate *in vitro* model. Cultures conducted in the aforementioned containers are of two-dimensional (2D) character, which do not imitate natural cells *in vivo* environment. Cells in the human body are subjected constantly to various environmental factors. Their development is strictly determined by cell-to-cell contact, omnipresent biochemical substances, hormones or oxygen. In the case of 2D substrates, the cells are grown basically as a monolayer, thus from the definition are slightly degraded [6-8].

Based on that, the lab-on-chips application in cellular research is of high importance. Due to possible ensurance of on-chip constant perfusion, precise and controllable stimulation with different external factors, also low contamination risks, such cell cultures are close to imitate 3D natural habitat character [9-10]. These features imply the further development of miniaturized microfluidic systems which are increasingly encountered in the literature as

a multi-function universal platforms, being able to provide simultaneously cell culturing, stimulation, manipulation, immobilization and detection of a single biological objects [11-15].

This work presents the preliminary results towards elaboration of a fully autonomous lab-on-chip platform intended for long-term culturing and investigation of different microbial objects. Dedicated lab-chip solutions and other culture life-supporting elements have been developed and tested. To date, the platform has been found useful for in-depth *Euglena gracilis* study and *in vitro* maturation of porcine cumulus-oocyte complexes (COC).

2. MATERIALS AND METHODS

The microfluidic platform, referred here, integrates all-glass lab-on-chip device, 3D printed microflow regulator, OLED display, heating module, optical detection system for constant culture observation and dedicated tracking software ensuring real-time image (video) processing and metrological characterization of the biological samples. The block diagram of the platform is shown in the Fig. 1.

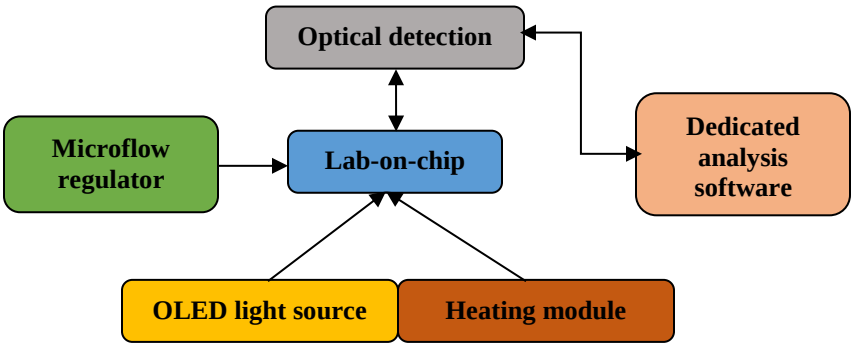

Fig. 1. Block diagram of the lab-on-chip platform dedicated to cells culturing and behavioral investigation

The chip is a main element of the platform, in which cell culturing is conducted. It has been fabricated utilizing glass micromachining processes, enclosing xurography, wet chemical etching and novel method of low-temperature (80 ºC) fusion bonding [16]. Few structures of the chips have been manufactured to match the features of the investigated cells (euglena, oocytes), differing notably in size, shape or surface adhesion. View of the chips are presented in the figure 2.

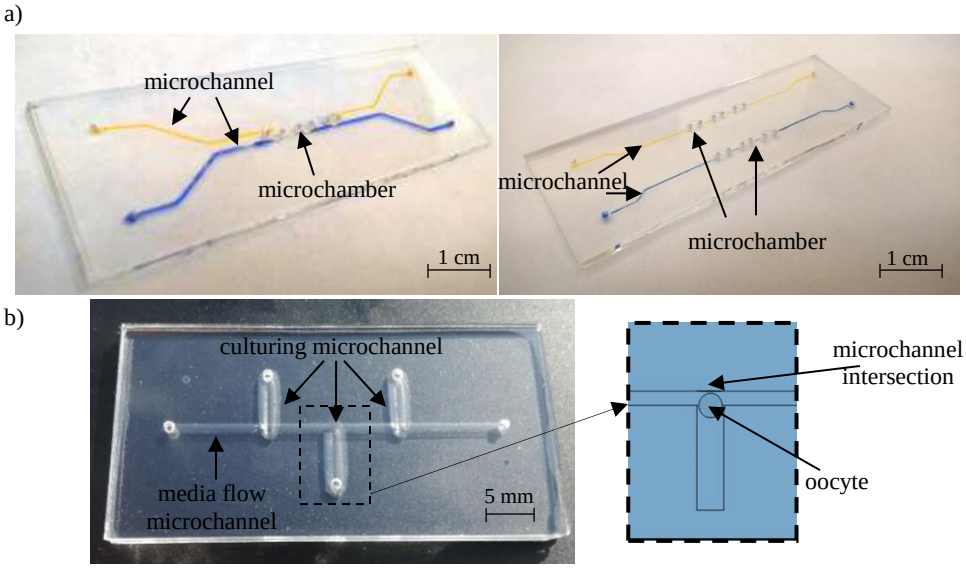

Fig. 2. All-glass lab-on-chips for culturing of: a) *Euglena gracilis, on the left* – double supply variant, on the right – single supply variant [based on 16], b) porcine oocytes

In order to constantly deliver fresh nourishment to the cultures, a microflow regulator has been fabricated utilizing the technique of 3D printing [17]. A PDMS membrane has been used in its structure to repeatably diffuse small portion of life-supporting medium (circa 0.3 µL/min) to the lab-chip chamber. OLED display (model: µOLED-160-G2, 4D Systems, Australia) has been applied as a light source ensuring selective and precise irradiation of cells in wide emission spectra [18]. A heating unit, based on Peltier module, has been developed to enhance appropriate on-chip oocytes growth, which requires a stable temperature of 38 ^{0}C. Digital microscope (model: Smart 5MP Pro, Delta Optical, Poland) observes the culture constantly. Based on the acquired image sequence, a dedicated tracking software [19] provides parametric evaluation of the cultures, enclosing qualitative and quantitative analysis of cells number, size, mobility, path length and movement trajectories time-dependently. A view of the overall platform is shown in the figure below (Fig. 3).

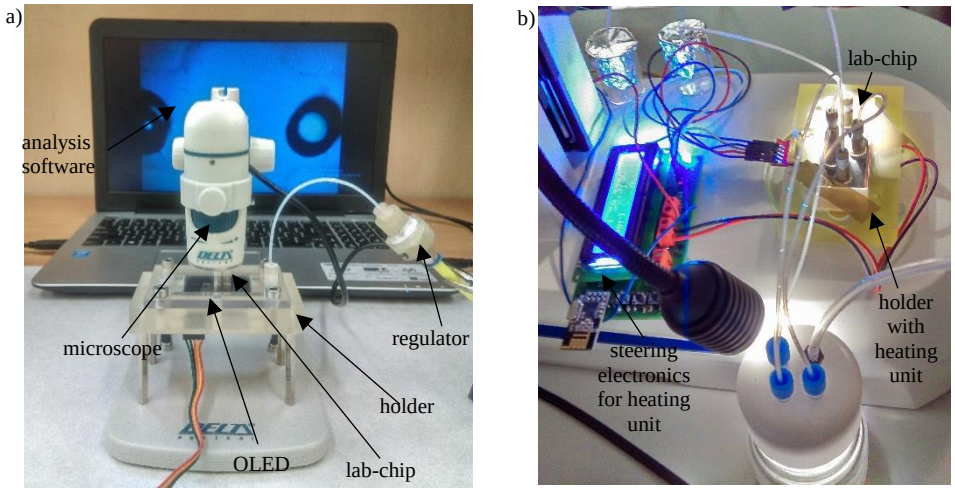

Fig. 3. Lab-on-chip platform for culturing and investigation of cells behaviour: a) study of *E. gracilis*, b) oocytes maturation

3. RESULTS AND DISCUSSION

The experiments on the platform have shown a notable, long-term photosynthesis-based growth of *Euglena gracilis* on-chip, resulting in its population change from 8 to 44 cells in a two-week period [17]. The possibility to simultaneously and selectively deliver different media to the microfluidic system has demonstrated repeatable chemotaxis of euglena towards air instead of N_2 (Fig. 4a) [16]. The tests on *E. gracilis* photosensitivity have revealed a noticeable degradation of these creatures during the blue light irradiation (470 nm) and significant increase in cells mobility (by 34 %) in the case of red color illumination (615 nm) [18]. The process of porcine oocytes *in vitro* maturation have shown the chip high reliability, resulting in a notable oocytes expansion. The surface area of cultured biological objects have grown by nearly 100 %, indicating suitable maturation conditions (Fig. 4b).

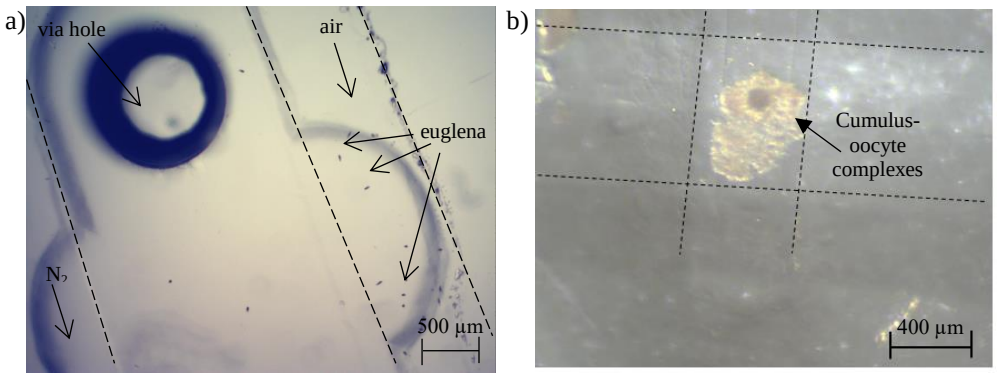

Fig. 4. Cells cultured on-chip: a) chemotaxis of *Euglena gracilis* towards air instead of N_2, based on [16], b) notable expansion of porcine oocyte during maturation process

4. CONCLUSION

Universal lab-on-chip platform for culturing and behavioral investigation of cells has been shown. The platform integrates all-glass lab-on-chips, 3D printed microflow regulator, OLED display, heating unit, optical detection system and real-time tracking software enabling long-term culturing and constant cells analysis. To date, the platform has been successfully applied for extensive research of single cell microorganisms and porcine oocytes. Currently, the platform is being adapted to ensure culturing and analysis of cancer ovarian cells, in close cooperation with Wrocław Medical University.

Acknowledgement

The work has been financed by the NCN OPUS 10, project no 2015/19/BST8/01110.

References

[1] M. A. Khorshidi, P. K. P. Rajeswari, C. Wählby, H. N. Joensson, H. A. Svahn, "Automated analysis of dynamic behavior of single cells in picoliter droplets", *Lab on a Chip*, vol. 17, pp. 931-37, 2014.

[2] K. Ozasa, J. Won, S. Song, S. Tamaki, T. Ishikawa, M. Maeda, "Temporal change of photophobic step-up responses of Euglena gracilis investigated through motion analysis", *PLoS ONE*, vol. 12, no. 2, pp. e0172813.

[3] P. J Hung, P. J. Lee, P. Sabounchi, R. Lin, L. P. Lee, "Continuous Perfusion Microfluidic Cell Culture Array for High-Throughput Cell-Based Assays", *Biotechnol. Bioeng.*, vol. 89, pp. 1-8, 2004.

[4] B. M. Carlson, *Stem Cell Anthology*, 1st edn., Elsevier, Canada, 2010.

[5] R. I. Freshney, *Culture on animal cells. A manual of basic technique and specialized applications*, 7th edn., John Wiley & Sons, USA, 2016.

[6] L. Richard *et al*, "Maturation of Induced Pluripotent Stem Cell Derived Hepatocytes by 3D-Culture", *PLoS ONE*, vol. 9, e86372, https://doi.org/10.1371/journal.pone.0086372, 2014.

[7] Y. Imamura *et al*, "Comparison of 2D- and 3D-culture models as drug-testing platforms in breast cancer", *Oncology Reports*, vol. 33, no. 4, pp. 1837-43, 2015.

[8] K. M. Mabrya, S. Z. Paynea, K. S. Anseth, "Microarray analyses to quantify advantages of 2D and 3D hydrogel culture systems in maintaining the native valvular interstitial cell phenotype", *Biomaterials*, vol. 74, pp. 31-41, 2016.

[9] S. Sart, R. F.-X. Tomasi, G. Amselem, C. N. Baroud, "Multiscale cytometry and regulation of 3D cell cultures on a chip", *Nature Communications*, vol. 8, 2017.

[10] H. J. Chen, P. Miller, M. L. Shuler, "A pumpless body-on-a-chip model using a primary culture of human intestinal cells and a 3D culture of liver cells", *Lab Chip*, vol. 18, pp. 2036-46, 2018.

[11] K. Chawla, S. Bürgel, G. Schmidt, F. Rudolf, O. Frey, A. Hierlemann, "Microfluidic cell culturing platform combining long-term, high-resolution imaging with impedance spectroscopy", *Procedia Engineering*, vol. **120**, pp. 154–57, 2015.

[12] T. Reinecke, P. Biechele, V. Schulte, T. Scheper, S. Zimmermann, “Low-cost sensor system for non-invasive monitoring of cell growth in disposable bioreactors”, *Procedia Engineering*, vol. 120, pp. 548–551, 2015.

[13] K. Woodruff, S.J. Maerkl, “A high-throughput microfluidic platform for mammalian cell transfection and culturing”, *Nature: Scientific Reports***, vol. 6**, 2016.

[14] F. Alexander, S. Eggert, J. Wiest, “A novel lab-on-a-chip platform for spheroid metabolism monitoring”, *Cytotechnology*, vol. 70, pp. 375–86, 2017.

[15] R. Gomez-Sjoberg, A. A. Leyrat, D. M. Pirone, C. S. Chen, S. R. Quake, “Versatile, Fully Automated, Microfluidic Cell Culture System”, *Anal. Chem.*, vol. 79, pp. 8557–63, 2007.

[16] A. Podwin, W. Kubicki, J. A. Dziuban, “Study of the behavior of *Euglena viridis*, *Euglena gracilis* and *Lepadella patella* cultured in all-glass microaquarium”, *Biomed. Microdevices*, vol. 19, 2017.

[17] A. Podwin, R. Walczak, J. A. Dziuban, “A 3D Printed Membrane-Based Gas Microflow Regulator for On-Chip Cell Culture”, *Applied Sciences*, vol. 8, 2018.

[18] A. Podwin, D. Lizanets, “OLED Display as a Useful Tool Towards Real-Time On-Chip Photosensitivity Investigation of Microorganisms”, Proceedings of the 2018 XV International Scientific Conference on Optoelectronic and Electronic Sensors (COE), 17-20 June 2018, Warsaw, Poland, *IEEE Xplore*, 2018.

[19] D. Lizanets, J.A. Dziuban, R. Walczak, "Comparison of algorithms for detection and real-time tracking of living microorganisms in lab-on-a-chip devices", *Mixed Design of Integrated Circuits and Systems 2017 MIXDES - 24th International Conference*, available: 10.23919/MIXDES.2017.8005280.

NUMERICAL ANALYSIS OF THE INFLUENCE OF TECHNOLOGY-RELATED ERRORS ON OPTICAL PARAMETERS OF TWO-DIMENSIONAL PHOTONIC CRYSTALS

D. Przybylski[1*], A. Zięba[1,2], S. Patela[1]

[1]Faculty of Microsystem Electronics and Photonics, Wrocław University of Science and Technology, Janiszewskiego 11/17, 50-372 Wrocław, Poland
Nanores Company, Bierutowska 57-59, 51-317 Wrocław, Poland
*e-mail: dariusz.przybylski@pwr.edu.pl

Abstract: *In this paper, we present results of numerical analysis of light transmission and reflection of two-dimensional photonic crystal (PhC), with particular attention given to issues related to errors inducted by fabrication methods. The PhC was composed of nanocylinders forming a rectangular lattice and was fabricated by the FIB (focused ion beam) technique on the top of the silicon wafer. In our analysis, we considered the PhC with two types of technology-related deviations from the nominal "ideal" shape: the imperfections of the form of nanocylinders and redeposition of the etched material on the top of them. The actual shape of the cylinders was obtained from the scanning electron microscope (SEM) image of a cross-section of the prepared PhC. The light reflection and transmission were compared with the ones obtained for the ideal structure of the PhC. It is shown, that the reflection and transmission are influenced differently by different technological imperfections. It is also shown, that the reflection characteristics of the p-polarized light are the most sensitive to the shape changes.*

Keywords: photonic crystal, focused ion beam, numerical analysis

1. INTRODUCTION

By definition, photonic crystal (PhC) is an optical nanostructure with periodicity in dielectric constant ε. PhCs can affect properties of photons, just like semiconductors affect the properties of electrons. Depending on the ε periodicity distribution, one can distinguish three types of photonic crystals: 1-, 2- or 3-dimensional. The 1- and 2-dimensional PhCs can be fabricated with relative ease within minutes or hours; 3-dimensional PhCs are more complex, and their fabrication could last for hours. In general, the fabrication methods of photonic structures are divided into two groups: bottom-up and top-down [1,2]. One of top-down method is Focused Ion Beam (FIB) technology. The FIB milling uses the ion beam to sputter material. Since the volume of the removed material is defined by a few well-controlled parameters, like the processing time or ion dose, the material removal is very precise. For example, with the FIB microscope, it is possible to prepare a matrix of holes with diameters about 50 nm with the accuracy of 10 nm. FIB processing allows for material modification in nano- and microscale. Therefore, FIB milling is a popular method for prototyping and manufacturing of photonic structures [3,4]. By the nature of the process, structuring by the ion beam is relatively slow: depending on the beam current, the milling rate varies from 0,01 μm3/s to 20 μm3/s. However, increasing the beam current lowers accuracy of the fabrication. With the FIB microscope, it is possible to prepare different

photonic structures in a reasonable time. However, there are three challenges. First, the possibility of mass production is limited. Currently, the FIB technology in photonics is used mainly for prototyping, as only a few photonic structures can be fabricated in one run. Secondly, the intensity of ion beam has Gaussian cross-section, which results in bending of the side walls of the etched patterns. Thirdly, the material removed (atomized) by the ion beam is redeposited, mostly at the edges of the etched pattern (Fig.2). This phenomenon can affect the shape of the prepared structure [5].

This paper aims to evaluate numerically the influence of technology-induced errors on the performance of the antireflective coating made of 2D photonic crystals. Photonic crystals have been fabricated and their shapes measured. Numerical models based on the measured profiles have been created. We have shown the influence of technology-induced errors on the optical parameters: reflection and transmission. Moreover, we have analyzed the impact of a single technology defect: redeposition of the etched materials and the imperfections of the form of nanocylinders on the optical properties of PhCs.

2. EXPERIMENT

As a part of our research, the photonic structure was fabricated on a silicon substrate. The process was carried out with the 30 kV Ga+ Helios NanoLab 600i FIB/SEM microscope, form FEI Co. Schematic diagram of the assumed structure is presented in Fig.1.

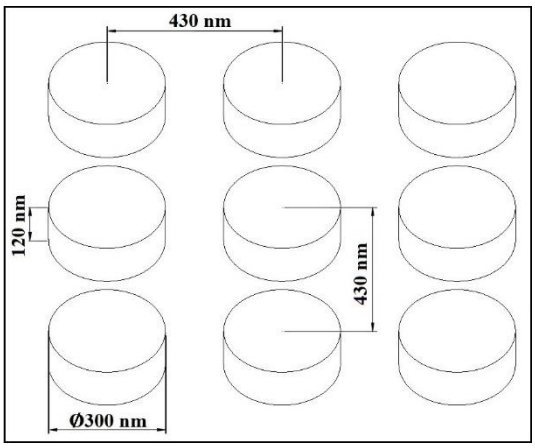

Fig. 1. Schematic diagram of the fabricated photonic crystal

Target parameters of the structure were: 120 nm height of the cylinders, 300 nm diameter, 430 nm period and 3 x 5 μm size of the whole structure. Ion beam current was set to 83 pA, which corresponded to the dose of 1,8 nC/μm2. The dwell time was set to 1 μs, and the overlap was set to 50% [5]. The last two parameters were defined in FIB microscope using nominal beam diameters provided by the microscope manufacturer.

Figure 2 shows the prepared photonic crystal: A) presents a top view and B) oblique view. Fig. 2B displays imperfections induced by the technology. Rods are not perfectly cylindrical; this is due to the Gaussian distribution of the ion beam.

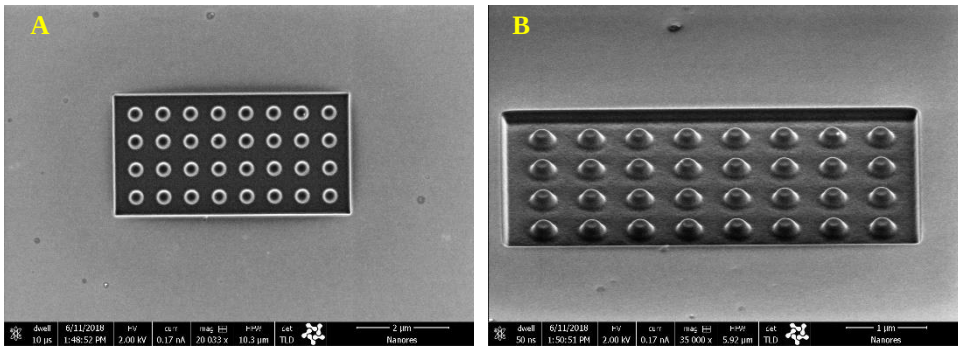

Fig. 2. SEM images of prepared photonic structure: A) top view, B) angular view from 52 degrees

Subsequently, the cross-section of the PhC was made, the result is presented in Fig. 3. During this process the area of interest was chosen, then the surface was protected with a platinum layer, and then the wall polished by the ion-beam was created; the wall is presented in Fig. 3. The actual parameters of the fabricated structure were as follows: 113 nm depth, 200 nm diameter of a single rod (measured from the top view) and 429 nm period.

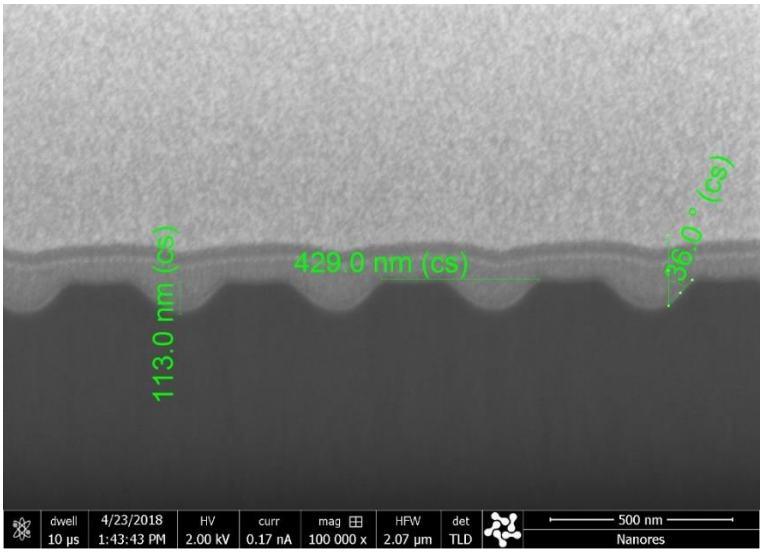

Fig. 3. SEM image of a cross-section of the prepared photonic crystal

3. INFLUENCE OF TECHNOLOGY-RELATED ERRORS ON PROPERTIES OF PHOTONIC CRYSTALS

Each 2D photonic crystal is built of "atoms," which usually are cylinders or holes of nanometer sizes. Modeling usually assumes the perfect shape of the nanocylinders (or nanoholes) [6]. To analyze errors introduced during FIB fabrication of a photonic structure, we modified photonic crystal's model, by introducing more realistic shapes of the "atoms."

Based on the cross-section obtained with SEM (Fig.3), we created four models of such "atoms" (Fig.4). To determine the influence of technology-related errors on optical parameters of PhC, we built the following models: ideal structure (Fig.4a) without any technology-related errors, structure with redeposited etched material (Fig.4b, called PhC's model with a 'crown'), with the inclined side walls of nanocylinders (Fig.4c) and the most realistic model, resembling the fabricated PhC (Fig.4d). The model from Fig.4d has been created based on the measured profile obtained from the SEM image of a cross-section of the prepared photonic crystal (Fig. 3). For all of the models, transmission and reflection were calculated, and the results were compared with those obtained for the unstructured silicon layer of the same thickness as the height of PhC's nanocylinders.

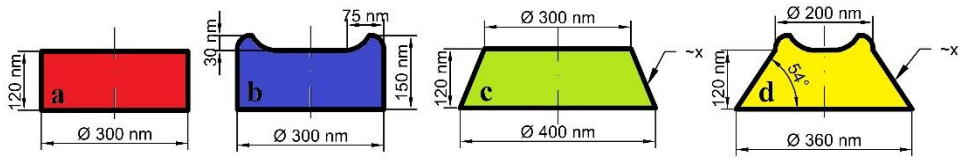

Fig. 4. The profiles of cylinders of modeled photonic crystal: ideal structure (a), with technology-related errors: redeposited etched material (b), inclined side walls of nanocylinders (c) and real structure (d)

Modeling was done with the FDTD method. The influence of the defects on transmission and reflection of photonic crystal was analyzed. The modeled photonic crystals were illuminated by plane wave sources of 900 nm wavelength; calculations were performed for two polarizations: S and P. The 900 nm wavelength was selected as as the maximum sensitivity wavelength for silicon detectors [7].

For the light beam of S polarization, the reflection increases monotonically with the angle of incidence [8]. For the P polarization, the reflection decreases up to the Brewster angle, then increases as the angle of incidence increases. In theory, for the Brewster angle, the reflection of P wave should be zero [8]. However, the non-zero value of a minimum of reflectance of P wave for the thin-films dielectrics is named the pseudo-Brewster angle. The pseudo-Brewster angle depends on the thickness of dielectrics' layer, the refractive index of layer and substrate [9]. Therefore, the position of the minimum of the reflection changes.

The modeling has been carried out with changing the angle of incidence from -85° to 85° by 5°.

3.1. Modeling of a photonic crystal for the S polarized incident beam

In this chapter, we present calculated reflection and transmission coefficients as a function of the angle of incidence for the S polarization of the incident light. Figure 5 shows the

reflection obtained for the ideal structure of PhC, bare sample of Si, two models with different errors and the real structure of PhC.

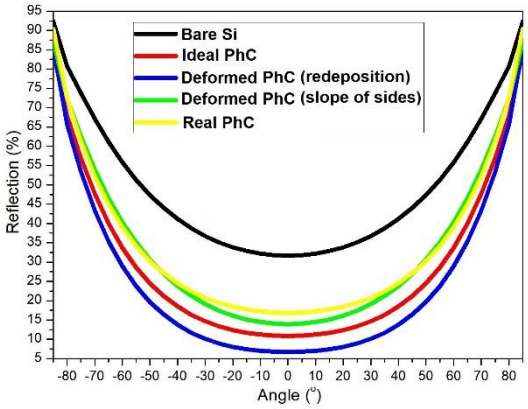

Fig. 5. Reflection as the function of the angle of incidence, for 900 nm wavelength for the S polarization, for technology-related errors' models of PhC and a bare silicon layer

Analyzing the data from Fig.5, we notice that the reflection is the highest for a bare sample of silicon. The reflection of PhC's models is the highest for the real structure (Fig.4d) and PhC's model with an inclined side of cylinders (Fig.4c). However, in the range of -30 to 30 degrees, the reflection for real's model of PhC gets the highest results of all presented PhC's models. Unfortunately, these models of PhC show that they decrease the reflection of PhC in comparison to ideal structure's model of PhC (Fig.4a). The 'crown' error (Fig.4b) increase the reflection in comparison to the ideal model of PhC. The shapes of reflection's functions for the S polarization are compatible with the theory [8].

Figure 6 shows the transmission as the function of the angle of the incidence for the S polarization.

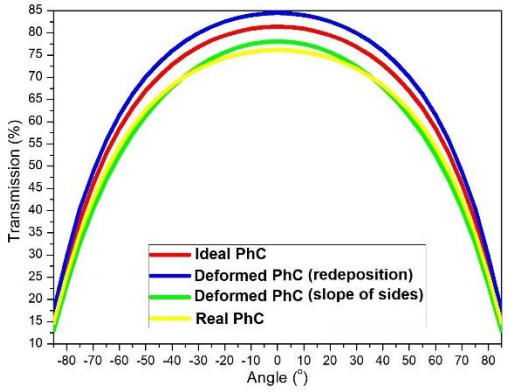

Fig. 6. Transmission as the function of the angle of incidence for 900 nm wavelength for the S polarization, for technology-related errors' models of PhC

The transmission confirms that the model of a photonic crystal with 'crown' error gets the increase of optical parameters in comparison to the ideal model of PhC. Moreover, for the real model of PhC, the transmission is the lowest in the range of -30 to 30 degrees. However, outside of this range, the lowest transmission is for a model of PhC with a slope of the sides.

3.2. Modeling of a photonic crystal for the P polarized incident beam

In this chapter, we analyze the reflection and transmission as a function of the angle of incidence for the for the P polarization of the incident beam. The results of the modeling process were presented in Figure 7 – for reflection and Figure 8 – for transmission.

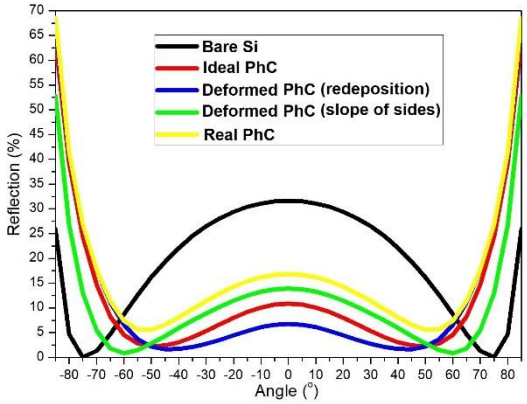

Fig. 7. Reflection as the function of the angle of incidence for 900 nm wavelength for the P polarization, for technology-related errors' models of PhC and the bare silicon layer

Analyzing the data from Fig. 7, we notice that for different models, the angles of the minimum of the reflection are different. The Brewster angle for a silicon layer is equal to 75° and -75°, as should be expected [8]. The position of the minimums of the pseudo-Brewster angles for different models of PhC vary. The lowest value of the reflectance is for the PhC with an inclined side of cylinders. In this case, the pseudo-Brewster angle is 60° and -60°. The models of PhC: ideal and with 'crown,' have the value of the reflectance approximately at the same level. However, the pseudo-Brewster angles: for the ideal model of PhC is equal to 50° and -50°, and for the model of PhC with 'crown' is equal 45° and -45°. For the real model of PhC, the pseudo-Brewster angle is equal to 55° and -55°. It also has the highest level of reflectance of all analyzed models.

In the range of angles from -60° to 60°, the highest reflection is for the bare silicon. In the same range of angles, the realistic model of PhC gets the highest values of reflection from all analyzed models. The model of PhC with an inclined side of cylinders increase the reflection in comparison to real structure. But, in comparison to the model of the ideal structure of PhC, both models decrease the reflection. The lowest reflection in the range of angles from -40° to 40° for a model of a photonic crystal with 'crown' error. The reflection for all of the models of PhC, approximately outside of the range from -65 to 65 degree is increased to 50-70%.

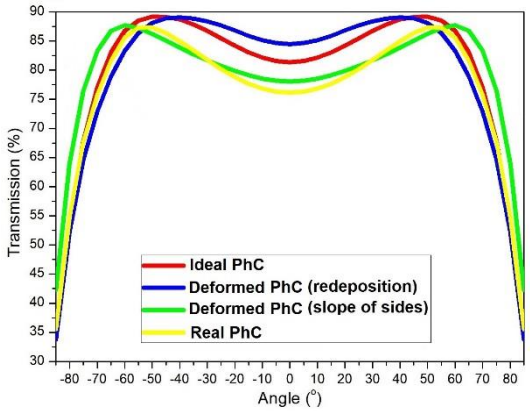

Fig. 8. Transmission as the function of the angle of incidence for 900 nm wavelength for the P polarization, for technology-related errors' models of PhC

The transmission from the Figure 8, confirm the results of PhC's models as the reflection.

4. CONCLUSION

In this work, we presented the numerical analysis of the influence of technology-induced errors on the reflectance and transmittance of 2D photonic crystals, fabricated with FIB technology. The shape of elements of the PhC was obtained from the measurement of the fabricated sample. All of the analyzed models of PhC reduced the reflection and increased the transmission of the 900 nm wavelength in comparison to a bare layer of silicon. For devices like solar cells or photodetectors, this should be regarded as an advantage.

The analysis shows that the "crown" created by the redeposition of material during FIB etching, enhanced both reflectance and transmittance, even beyond the values obtained for the "ideal" photonic crystal. The model of real photonic crystal structure produced worse results than other analyzed models.

The figures 5 and 6 for the S polarization give us information only about the intensity of the reflection and transmission. The shapes of the functions are symmetric and monotonic in the range 0° to 90° and 0° to –90°. Therefore, it is hard to analyze the influence of technology-inducted errors on the parameters of the photonic crystal. The P polarization's figures show the intensity of the reflection too, but also, we notice a different position of the minimum of the pseudo-Brewster angle for the other technology-related errors of PhC.

In the case of S polarization (Fig.5 and 6), the most realistic model of photonic crystal shows that the effect of the redeposited etched material ('crown' error) doesn't eliminate the influence of the slope of the side. Nevertheless, in the case of P polarization (Fig.7 and 8), we observed that the effect of redeposited etched material compensates some deterioration from the slope of the side for the real model of PhC.

We have shown, that technology-induced errors affect transmission and reflection of surfaces covered with 2D photonic crystals. The inclined side-walls lower the transmission and increase reflection. If the layer is to be used as an antireflection coating, that would mean lowering performance of the devices such as solar cells or photodetectors. On the

other hand, modification of the top surface of nano-cylinders can improve the performance of the PhC layer. Here, this was a side effect of the FIB technology. However, with the FIB technology, this can be done intentionally, improving the performance of the PhC structure.

The results have to be verified by experiment to confirm the relation between technology-indicated errors.

Acknowledgement

This research was supported by the Statutory Grant of the Faculty of Microsystem Electronics and Photonics, Wrocław University of Science and Technology.

The coating, SEM, and FIB etching equipment were provided by Nanores company.

References

[1] INOUE K., OHTAKA K., Photonic Crystals, Springer-Verlag Berlin Heidelberg, 2004.

[2] SOUKOULIS C.M., Photonic Crystals and Light Localization in the 21st Century, Springer Netherlands, 2001.

[3] NELLEN P.M., CALLEGARI V., BRONNIMANN R., Microelectron. Eng., 83 (2006), 1805-1808.

[4] GIERAK J., et al., Microelectron. Eng., 57-58 (2001), 865-875.

[5] GIANNUZZI L.A., Introduction to Focused Ion Beams, Springer US, 2005.

[6] ANAMORADI A., FASIHI K., Superlattice. Microst., 125 (2019), 302-309.

[7] ZIĘTEK B., Optoelektronika, Wydawnictwo Naukowe Uniwersytetu Mikołaja Kopernika, Toruń, 2005.

[8] BORN M., WOLF E., Principles of optics, Cambridge University Press, Cambridge, 1999.

[9] ALSAMMAN A., AZZAM R.M.A., J. Opt. Soc. Am. A, 27 no. 5 (2010).

GOLD NANOTRIANGLES FOR APPLICATIONS IN ORGANIC PHOTOVOLTAICS

N. Tarnowicz[1], L.K. Jagadamma[2], I.D.W. Samuel[2*], K. Matczyszyn[1]

[1]Advanced Materials Engineering and Modelling Group, Faculty of Chemistry,
Wrocław University of Science and Technology,
Wybrzeże Wyspiańskiego 27, 50-370 Wrocław, Poland
[2]Organic Semiconductor Centre, SUPA, School of Physics and Astronomy,
University of St Andrews, St Andrews, KY16 9SS, United Kingdom
e-mail: idws@st-andrews.ac.uk

Abstract: *Organic solar cells (OPVs) are a promising solar technology because of their potential to be made over large areas at low cost and with low energy of manufacture. However, to date their efficiency is lower than the best inorganic materials. One possible way of increasing their efficiency is by enhancing absorption by incorporating plasmonic nanoparticles into the active layer. This paper presents an approach to preparation of plasmonic organic solar cells, based on the inclusion of triangular gold nanoparticles in the hole transport layer. The main focus is to review protocols for synthesis and post-synthetic treatment of the samples, which is necessary to optimize their concentration.*

Keywords: nanoparticles, gold, plasmonics, photovoltaics

1. INTRODUCTION

Many factors drive the world's current need for "green energy," notably economic and energy crisis, the limited character of natural sources, and increasing ecological problems. The U.S. Energy Information Administration emphasizes that by 2040 world energy consumption will increase by 28% from 575 quad (168500 TWh) to 736 quad (215700 TWh), mostly due to the rapid development of Asian countries [1]. From new energy harvesting technologies low costs and efficient implementation in everyday life are required. Solar power is by far the most abundant renewable energy source. It is estimated that solar irradiation reaching Earth's surface during one day may deliver enough energy for the humanity for the next 27 years (assuming the same energy consumption level) [2]. Taking into consideration that industrial development impacts the natural environment significantly and the amount of fossil fuel is constantly decreasing, solar energy as entirely environmentally-friendly and coming from the unlimited source appears to be the purest renewable form of energy.

Conversion of the solar irradiation into electricity is the main focus of photovoltaics. However, despite high efficiency of inorganic solar cells the main factors limiting their common usage are costs of production, installation, and maintenance. Moreover, photovoltaics and microelectronic industry compete for materials. Subsequent disadvantages of inorganic solar cells are rigidity and hazardous byproducts of the production process [2,3] and high energy of manufacture. Competitiveness of photovoltaic technologies demands reduction of total costs by the factor of 5 [4]. This makes it important to explore less energy intensive and potentially more cost-effective materials for solar power.

2. ORGANIC SOLAR CELLS

Organic photovoltaic devices are based on organic semiconductors – compounds which backbone consists of alternate σ (C-C) and π (C=C) bonds [5]. Conjugation of chemical bonds enables delocalization of π electrons and semiconducting properties [6]. OPVs based on polymers and low molecular weight organic compounds can be distinguished.

Low production costs and energy of manufacture are not the only reasons of the in-depth research on this technology. Polymers can be easily designed and chemically manipulated to obtain the most suitable structures. Devices can be fabricated at the low temperature conditions and are characterized by low weight and flexibility which enables to use them in wearable and portable electronics. However, organic solar cells face major problems, such as short lifetime, low efficiency and stability. Those obstacles along with problems with commercial large-scale production are essential to overcome in the impending future.

The efficiency of the solar cell is required to be possibly high and cover costs of the materials, their processing and encapsulation, exceeding 5% [7]. The most promising and emerging technologies (Table 1), for instance dye-sensitized solar cells or quantum dot solar cells barely reach power conversion efficiency of 10%, except for not stabilized Perovskite solar cells that are able to reach the benchmark of 20% [8] and a solution processed 2-terminal monolithic tandem organic solar cell with a new record power conversion efficiency (PCE) of 17% [9].

Table 1. Power conversion efficiencies of some photovoltaic technologies. [8, 9]

Photovoltaic technology	Power Conversion Efficiency (%)
Multijunction cells (four-junction, concentrator)	46.0
Multijunction cells (two-junction, concentrator)	35.5
Single junction GaAs (thin-film crystal)	28.9
Crystalline Si Cells (single crystal, non-concentrator)	26.6
Perovskite cells (not stabilized)	23.3
Thin-Film Technologies (CIGS)	22.9
Crystalline Si Cells (multicrystalline)	22.3
Tandem organic solar cells	17.4
Quantum dot cells (various types)	13.4
Dye-sensitized cells	11.9
Organic tandem cells	11.5

The Power Conversion Efficiency (PCE) of the device is defined as the maximum power generated in the solar cell P_{max} divided by the power of the incident solar light P_{solar} (eq.1).

$$PCE = \frac{P_{max}}{P_{solar}} \cdot 100\% \quad (1)$$

2.1. Operating mechanism of OPVs

Conversion of solar energy into electrical energy in OPVs consists of four subsequent stages (Fig. 1) [3, 5, 10]:

(1) photon absorption

The absorption of the photons occurs in the photoactive layer; as a result electron is excited from HOMO level of the donor to its LUMO level. A bound state of an electron and an electron hole, namely exciton, is formed.

(2) exciton diffusion

During the lifetime of the exciton it must diffuse (or energy transfer) to the donor/acceptor interface. Exciton diffusion is a complicated subject, but typically occurs over distances of 5-10 nm.

(3) charge separation

At the interface of donor/acceptor materials an electron is transferred to the LUMO level of the acceptor and a charge transfer (CT) complex is formed. The process is favorable when energy difference between LUMO levels of donor and acceptor exceeds the exciton binding energy. CT state becomes charge separated state when distance between charge carriers is greater than the coulomb capture radius of exciton.

(4) charge transport

Dissociated charges are subsequently transported via other elements of the device architecture to the electrodes (holes are collected at the anode and electrons at the cathode).

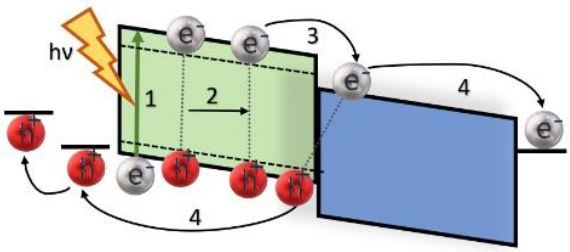

Fig. 1 Schematic illustration of the photophysical process in the organic solar cell.

There are several losses mechanisms that as a consequence lead to the PCE of OPVs lower than 100%. Firstly, excess energy (exceeding the exciton formation energy) photoabsorbed in the first stage of the process is lost. Secondly, exciton unable to dissociate within the lifetime decays to its ground state contributing to subsequent losses of the absorbed energy. The next loss mechanism is geminate recombination of charges which competes with free charge carriers generation. The last mechanism is related to the carrier recombination within the architecture of the device.

The External Quantum Efficiency (eq. 2) of the device specifies total efficiency in relation to the absorbed wavelength and can be thus described with efficiencies of the processes occurring in the OPVs as follows [5]:

$$EQE(\lambda) = \eta_{abs}(\lambda) \cdot \eta_{diff}(\lambda) \cdot \eta_{CT}(\lambda) \cdot \eta_{coll}(\lambda) \quad (2)$$

Where: η_{abs} is fraction of photons absorbed; η_{diff} is fraction of excitons that reach the donor/acceptor heterojunction; η_{CT} is fraction of excitons effectively separated; η_{coll} is fraction of charges collected by the electrodes.

There have been several attempts to increase PCE of OPVs including new materials development, new preparation approaches (to control morphology), architecture changes of the devices (introducing new layers, e.g. hole/electron transport layer; preparation of tandem solar cells) and implementation of other technologies. One of the examples of the latter approach is incorporation of plasmonic nanoparticles into OPVs.

2.2. Plasmonics for photovoltaics

Plasmonic nanoparticles are made of metals e.g. Cu, Ag, Au and are structures of sizes in the range from 1 to approximately 100 nm. Their size being comparable with the wavelength of incident light is the main reason for their specific interactions with electromagnetic waves (Fig. 2). Incident light causes collective oscillations of free metal electrons which leads to charge redistribution on the surface of nanoparticle and dipole generation. Those oscillations are called plasmons and upon the specific resonant conditions when light frequency matches the frequency of oscillating electrons the phenomenon is called localized surface plasmon resonance (LSPR). LSPR depends on shape, size, and material nanoparticle is composed of along with the properties of the medium surrounding nanostructure.

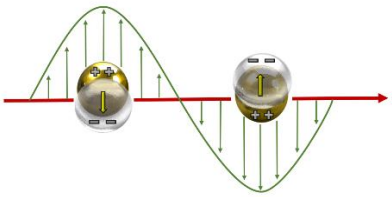

Fig. 2. Schematic representation of Localized Surface Plasmon Resonance

Specific nature of those interactions leads to strong local electric field enhancement in the nearest surrounding of nanoparticle, improving the absorption of light. Hence, the nanoparticles of sizes ranging from 5 to 20 or 50 nm can act as antennas (Fig. 3), storing energy in their localized surface plasmon modes, increasing local electric field by the factor of 100 [11]. This phenomenon may contribute to the PCE enhancement of the plasmonic OPVs. On the other hand bigger nanoparticles are characterized by substantial scattering cross-sections, regularly bigger than their geometrical cross-sections [11]. Thence, incident light is scattered at different angles which leads to its trapping in the architecture of the device [11]. Due to this fact the optical pathlength of light and subsequently PCE of the device may be significantly improved (Fig. 3).

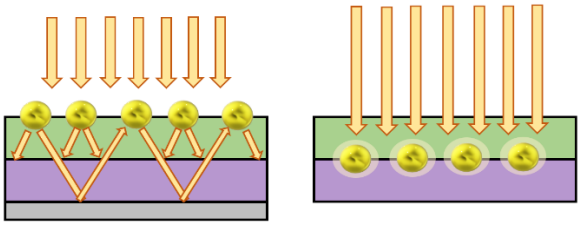

Fig. 3. Effects of incorporation of plasmonic nanoparticles in OPVs: light multiple penetration of the active layer and local electric field enhancement (from the left to the right respectively)

Plasmonic nanoparticles can be doped into different layers in the architecture of OPV device. Bigger nanoparticles will be specially beneficial in the hole transport layer, whereas smaller nanostructures can contribute significantly to the PCE increase after incorporation in the photoactive layer. The literature essentially focuses on usage of spherical gold nanoparticles. Presented study focuses on anisotropic, triangular nanoparticles instead. Gold nanoparticles are highly stable, well-researched and easily scalable in terms of size and synthesis yield. Additionally, implementation of nanotriangles in OPVs is justified by their ability to focus and concentrate optical radiative energy at the nanoscale and in three dimensions without significant losses [12]. Due to their sharp tips nanotriangles are able to act as plasmonic waveguides [12].

3. GOLD NANOTRIANGLES

3.1. Synthesis

Seeded growth method is considered as one of the most efficient means to synthesize anisotropic nanoparticles [13]. First stage of the synthesis requires reduction of the gold precursor ($HAuCl_4$) with strong reducing agent (e.g. $NaBH_4$) which leads to the synthesis of spherical nanoparticles (seeds) [13]. Overgrowth of those seeds into proper anisotropic structures requires presence of additional amount of metal precursor ($HAuCl_4$) at certain pH, soft reducing agent (e.g. ascorbic acid), shape-directing agent (iodine anions I^- in case of gold nanotriangles), and stabilizing agent (surface active agent such as CTAB or CTAC) [13]. Presence of shape-directing agent due to its adsorption/desorption balance on the metal surface breaks the symmetry leading to the preferential anisotropic growth [13]. On the other hand variations of its concentration lead to the nanoparticles of different sizes. Surfactants may also influence the growth process, however the proper mechanism has not been established yet.

In the frame of the study several chemical protocols have been tested. Here, we report one of them (Fig. 4) [14].

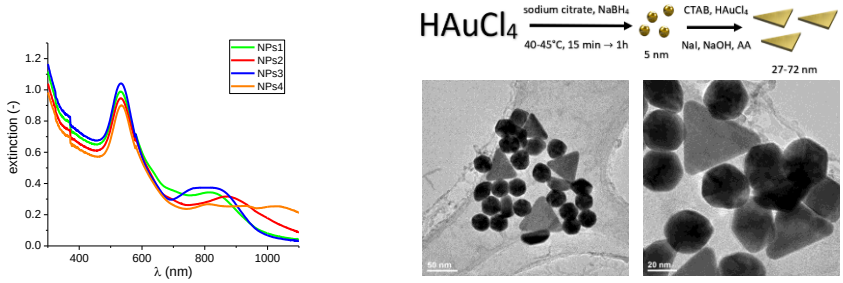

Fig. 4. UV-Vis extinction spectra, synthesis protocol and TEM image of the nanostructures prepared according to the literature [14] (from the left to the right respectively)

There are also several different approaches to the fabrication of gold nanotriangles, including lithography, physical synthesis by irradiation or chemical seedless synthesis. Syntheses using biological molecules as reducing, shape-directing and stabilizing agents are also possible. Here, we report one of them based on the literature protocol (Fig. 5) [15].

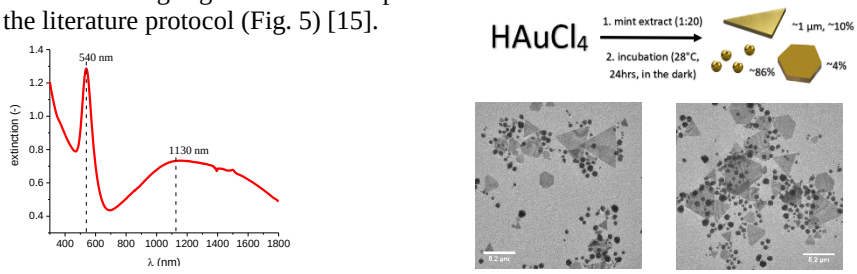

Fig. 5. UV-Vis extinction spectra, synthesis protocol and TEM image of the nanostructures prepared according to the literature [15] (from the left to the right respectively)

3.2. Post-synthetic treatment

As-synthesised gold nanotriangles are in the form of a water dispersion that enables their direct mixing with water dispersion of PEDOT:PSS – polyelectrolyte used subsequently as a hole transport layer in the architecture of OPVs. However, depending on the synthesis protocol different post-synthetic treatment needs to be applied in order to purify obtained nanostructures and optimize their concentration. In the case of chemical synthesis the most crucial step is the removal of surfactants. Hence the most promising approaches are centrifugation, functionalization with PEDOT:PSS or depletion flocculation. On the contrary, biologically synthesized nanoparticles can only be centrifuged to remove the byproducts and other synthesized shapes (spheres and hexagonal nanoplates).

4. CONCLUSIONS

Organic solar cells as an emerging photovoltaic technology still need improvement in several aspects. One of the promising approaches is incorporation of plasmonic nanoparticles in the architecture of the devices. Triangular gold nanoparticles acting as nanoconcentrators of the optical energy can be an appropriate replacement for

spherical nanostructures. Synthetic procedures have to be carefully chosen based on the desired parameters of the nanotriangles including size, monodispersity and yield. In order to purify and optimize the concentration of nanoparticles customized post-synthetic treatment has to be established.

References

[1] U.S. Energy Information Administration, *International Energy Outlook 2017* (2017).
[2] L.G. Li, G.H. Lu, X.N. Yang, E.L. Zhou, *Chin Sci Bull* 52 (2), 145-158 (2007).
[3] K.A. Mazzio, C.K. Luscombe, *Chem. Soc. Rev.* 44, 78-90 (2015).
[4] H.A. Atwater, A. Polman, *Nature Materials* 9, 205-213 (2010).
[5] G. Li, R. Zhu, Y. Yang, *Nature photonics* 6, 153-161 (2012).
[6] K.A. Vivek, G.D. Agrawal, *Int J Res Eng Technol* 3 (9), 338-341 (2014).
[7] G.A. Chamberlain, *Solar Cells* 8, 47-83 (1983).
[8] *Best Research-Cell Efficiencies Chart*, *NREL*, 17/7/2018.
[9] L. Meng *et al.*, *Science* 361, 1094-1098 (2018).
[10] G.J. Hedley, A. Ruseckas, I.D.W. Samuel, *Chem. Rev.* 117 (2), 796-837 (2017).
[11] M. Notarianni *et al.*, *Solar Energy* 106, 23-37 (2014).
[12] M.I. Stockman, *Physical Review Letters* 93, 13 (2004).
[13] M. Grzelczak, J. Pérez-Juste, P. Mulvaney, L.M. Liz-Marzán, *Chem. Soc. Rev.* 37, 1783-1791 (2008).
[14] M.R. Jones, C.A. Mirkin, *Angew. Chem. Int. Ed.* 52, 2886-2891 (2013).
[15] M. Klekotko *et al.*, *Phys. Chem. Chem. Phys.* 17, 29014-29019 (2015).

THERMOELECTRIC PROPERTIES OF SEMICONDUCTOR THIN FILMS OBTAINED BY MAGNETRON SPUTTERING

M. Turkiewicz*, W. Wasyluk, D. Nowak

Faculty of Microsystem Electronics and Photonics, Wrocław University of Science and Technology, Janiszewskiego 11/17, 50-372 Wrocław, Poland
e-mail: marta.turkiewicz@pwr.edu.pl

Abstract: *In this paper, the electric and thermoelectric properties of selected semiconductor thin films are discussed in terms of choosing the best deposition process and post processing conditions to obtain layers which exhibit the best thermoelectric properties. Presented studies are a general overview of the exemplary semiconductor material compositions used in thermoelectric applications – germanium doped with antimony or gold. The layers were fabricated by magnetron sputtering using the Ge:Au and the Ge:Sb alloy targets onto glass substrates. After deposition structures were annealed in the atmosphere of N_2 at three different temperatures (at 180°C, 200°C and 230°C). Afterwards, the thermocouples were created by deposition the Ag contact pads onto germanium films. In this work, particular attention has been paid to thermoelectric properties of fabricated thin films – the thermoelectric voltage, the Seebeck coefficient, the power factor PF and the dimensionless figure of merit ZT were determined.*

Keywords: *thermoelectricity, thin films, magnetron sputtering*

1. INTRODUCTION

The search for alternative electric energy sources becomes one of the most important issues of modern science and technology, mainly due to the fact that non-renewable energy sources are slowly running out [1]. One of the new idea for sourcing electric energy is the use of waste heat – heat which is lost, among other things, in high-energy industrial processes. It is estimated, that about 66% of the generated heat is not used in any way and the ability to convert even a fraction of this heat into electricity could be one of solutions for modern economy and policy aimed at the use of alternative and renewable energy sources [2, 3]. On the other hand, it can become a form of powering the microelectronic components and MEMS and NEMS in IoT networks [4]. Thermoelectricity is one of the simplest method for thermal energy conversions – thermoelectric generators (TEGs) can be easily integrated into existing industrial equipment and processes, they have no movable parts, they exhibit direct thermal-to-electric energy conversion mechanism and are easily scalable from milliwatts to kilowatts [5, 6]. Also thermoelectric generators can work in harsh environments (e.g. high temperature, mechanical shock, radiation or big pressure) while maintaining good degradation characteristic [7]. Moreover TEGs can be considered as one of the ways for producing electricity from waste heat.

Microgenerators are built from a series connection of several (or several dozen) thermocouples. A single thermocouple consist of two materials – of which at least one should exhibit very good thermoelectric parameters. Therefore, the search for alternative

thermoelectric materials is crucial for the production of microgenerators and the development of microelectronics and small size energy. The search for new materials is also supported by the development of material sciences and techniques for producing materials with desirable properties [8-9].

One of the new ways of developing thermoelectricity is the fabrication of thick and thin films thermoelectric materials. Such materials, after optimization, may have the properties similar to commercially used bulk materials. Also, the reduction of the characteristic dimensions of the designed structures leads to using less material, which in turn directly reduces the costs of microgenerators, as well as leads to their miniaturization [10].

This paper presents research on electric and thermoelectric properties of one of the promising thermoelectric materials – semiconductor germanium thin films doped with gold or antimony (5% by weight) obtained by magnetron sputtering.

2. FABRICATION PROCESS

The test structures were fabricated by magnetron sputtering using the circular alloy targets (Ge:Au and Ge:Sb) using the Pfeiffer Classic 570 magnetron sputtering system. In targets, both the gold and the antimony content was 5% by weight. All of the layers were deposited under Ar pressure of $5 \cdot 10^{-3}$ mbar and the applied constant power 350 W. The Ge:Au films were sputtered at a rate of ca. 1.3 nm/s and the Ge:Sb films at at rate ca. 2.2 nm/s. Germanium-based thin films were deposited onto glass substrates (Corning 7059) with dimensions of 30 mm x 20 mm. Before sputtering substrates were cleaned in a solution of perhydrol, deionized water and isopropanol to remove possible organic impurities from their surface. Then, metal masks with pre-cut patterns were attached to the substrates, which allowed to fabricate test structures with various shapes. After deposition selected layers were annealed for 30 minutes at several temperatures: 180°C, 200°C and 230°C using the BTU belt furnace. To describe thermoelectric properties of structures it was necessary to form the thermocouples containing germanium films, so on the top of all the considered layers the Ag contact pads were deposited (also by magnetron sputtering under the constant power 330 W, using the gold sputtering target). Figure 1 shows a photo of the exemplary Ge:Sb/Ag structures. As shown in Figure 1a, five structures were deposited onto one glass substrate, which was then divided into single thermocouples with dimensions of 15 mm x 3,5 mm.

The Talysurf CCI optical profilometer was used to measure the thickness of the deposited films. The average thickness of the Ge:Au films was 1.6 μm and the Ge:Sb films was 2.6 μm. Afterwards, the results obtained were used to calculate the electrical conductivity of the layers.

(a) (b)

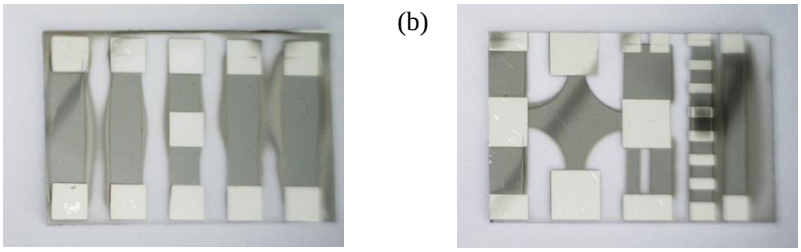

Fig. 1. Ge:Sb/Ag test structures: (a) structures for thermoelectrical measurements, (b) structure for electrical measurements (van der Pauw method)

3. RESULTS

After the deposition and annealing processes, four types of structures of both gold- and antimony-doped germanium thin films were obtained. In each group, the electric and thermoelectric properties of three annealed structures and one as-made were investigated.

3.1. Electric properties of the Ge:Au/Ag and Ge:Sb/Ag test structures

The most important electric parameters of tested thin films were the characteristic of resistance as the function of structure temperature $R = f(T)$ and electrical conductivity of layers and its temperature dependence. The resistance measurements were performed in the temperature range from *320 K* up to *495 K* (Figure 2). As shown in the Figure 2a, the Ge:Au/Ag thin films resistance decreased roughly linear within temperature and was higher for the annealed structures. For Ge:Sb/Ag layers, the resistance change was typical for semiconductors materials (Fig. 2b).

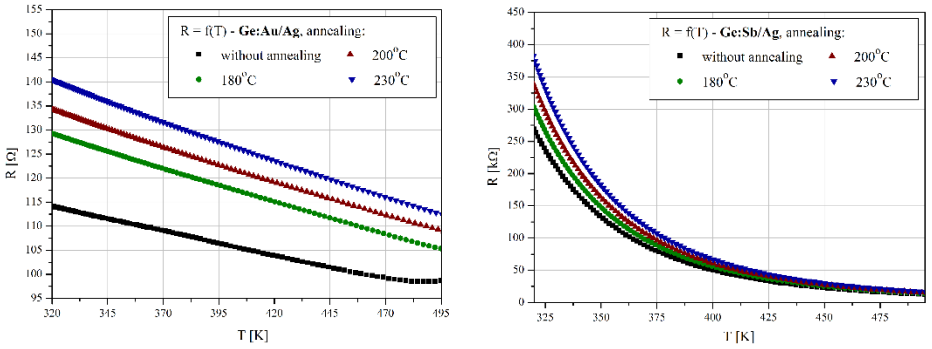

Fig. 2. The resistance *R* as a function of the structures' temperature *T* before and after annealing: (a) the Ge:Au/Ag test structures, (b) the Ge:Sb/Ag test structures

In addition, for the more detailed characterization of the properties of the investigated layers, changes in electrical conductivity as a function of temperature were determined (Fig. 3).

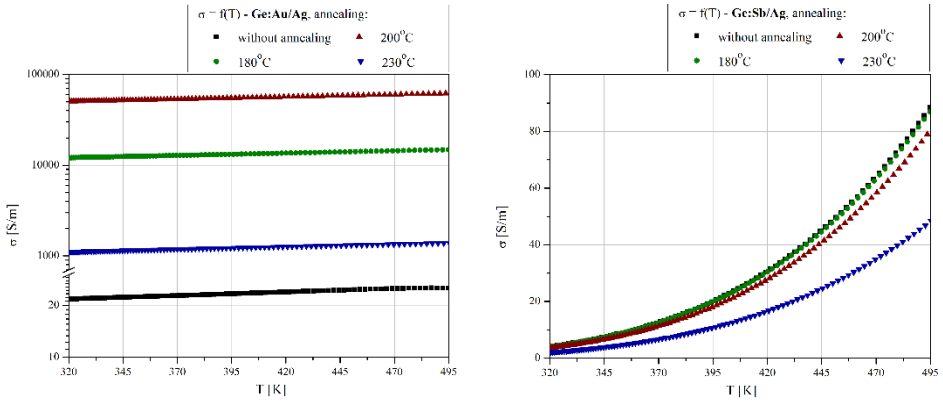

Fig. 3. The electrical conductivity σ as a function of the structures' temperature T before and after annealing: (a) the Ge:Au/Ag test structures, (b) the Ge:Sb/Ag test structures

The resistivity ρ and electrical conductivity σ at a room temperature (approx. *300 K*) was determined by the van der Pauw method. The results obtained are presented in the Table 1. The resistivity of Ge:Au/Ag layers was considerably smaller than Ge:Sb/Ag layers. Also, the conductivity of Ge:Au/Ag thin films was higher for the annealed structures, however for layers annealed at 230°C the large decrease in conductivity was observed. For Ge:Sb/Ag thin films the conductivity decreased with annealing temperature.

Table 1. Electric properties of the Ge:Au/Ag and Ge:Sb/Ag test structures: resistivity ρ and conductivity σ at *300 K*

Test structure	**T [°C]**	**ρ [Ω·m]**	**σ [S/m]**
Ge:Au/Ag	without annealing	0,046	21,6
	180	$8.4 \cdot 10^{-5}$	$1.2 \cdot 10^{4}$
	200	$2.0 \cdot 10^{-5}$	$5.0 \cdot 10^{4}$
	230	$8.9 \cdot 10^{-4}$	$1.1 \cdot 10^{3}$
Ge:Sb/Ag	without annealing	0.29	3.42
	180	0.29	3.34
	200	0.34	2.94
	230	0.57	1.72

3.2. Thermoelectric properties of the Ge:Au/Ag and Ge:Sb/Ag test structures

One of the most important parameter describing the performance of thermoelectric generators is the thermoelectric voltage. The thermoelectric voltage U generated in the Ge:Au/Ag and Ge:Sb/Ag structures as a function of the temperature difference between hot and cold junction of thermocouples ΔT was determined. In presented tests, the cold junction temperature was approximately constant ($T_c \approx 296\ K$) and the hot junction temperature increased from the room temperature up to 490 K. The results are shown in Figure 4. Both gold- and antimony-doped germanium films were *n-type* semiconductor materials, which is why the thermoelectric voltage values were negative. As shown in Figure 4a, for the Ge:Au/Ag structures the generated thermoelectric voltage increased roughly linearly within increasing temperature difference ΔT with rising slopes of $U = f(T)$ curves. For the Ge:Sb/Ag structures the generated thermoelectric voltage also increased within temperature difference between opposite ends of thermocouples, but in this case with slightly decreasing slopes of $U = f(T)$ curves (Fig. 4b).

On the basis of $U = f(T)$ curves, the temperature dependence of Seebeck coefficient for each layer was determined using the equation (1). The results are shown in Figure 5.

$$S = \frac{\Delta U_T}{\Delta T} = \frac{U_{T2} - U_{T1}}{T_2 - T_1} \tag{1}$$

The Seebeck coefficient for the Ge:Sb/Ag test structures reached values approximately ten times higher than for the Ge:Au/Ag thin films, however it fluctuated in the range of low temperatures and decreased within increasing structure temperature.

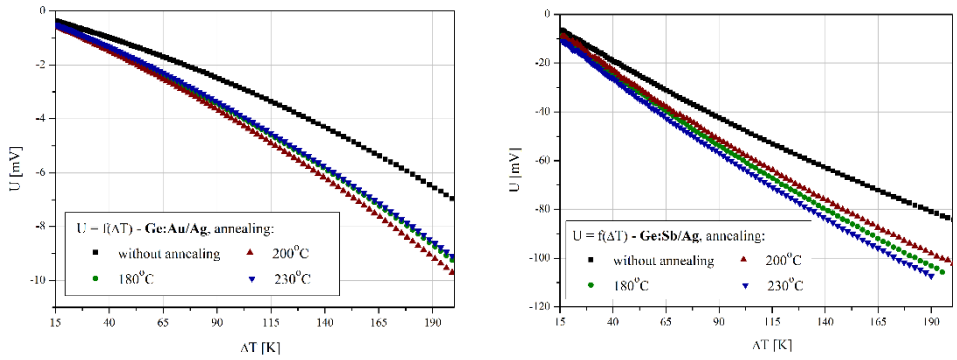

Fig. 4. Thermoelectric voltage U as a function of temperature difference ΔT between the opposite sites of the investigated thermocouples before and after annealing: (a) the Ge:Au/Ag test structures, (b) the Ge:Ab/Ag test structures

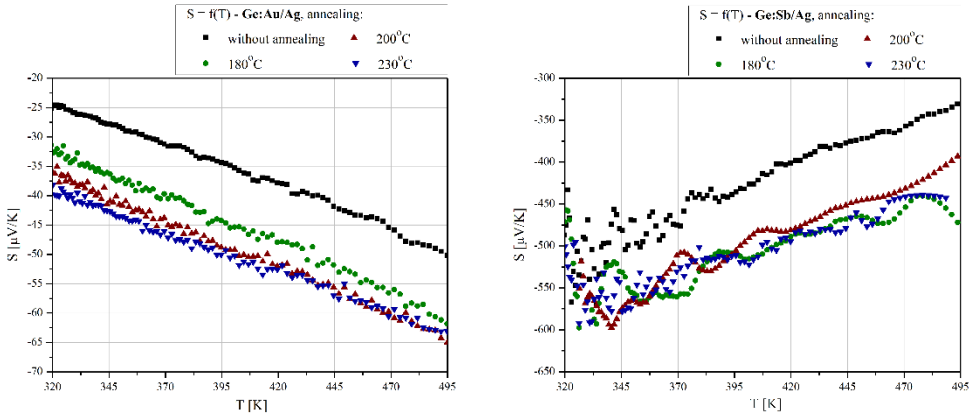

Fig. 5. The Seebeck coefficient *S* as a function of the temperature *T* before and after annealing: (a) the Ge:Au/Ag test structures, (b) the Ge:Sb/Ag test structures

To compare thermoelectric materials among each other, the power factor PF (Equation 2) and dimensionless figure of merit *ZT* (Equation 3) were defined. *PF* and *ZT* are the combinations of the three most important parameters describing the thermoelectric materials – the Seebeck coefficient *S (V/K)*, the electrical conductivity *σ (S/m)* and the thermal conductivity *κ (W/m·K)*. In addition, *ZT* is determined at absolute temperature *T*.

$$PF = S^2 \cdot \sigma \tag{2}$$

$$ZT = \frac{S^2 \cdot \sigma}{\kappa} \cdot T \tag{3}$$

On the basis of the results of Seebeck coefficient and electrical conductivity measurements, the temperature dependence of power factor was determined (Fig. 6). As shown in the Figure 6a, the higher power factors of Ge:Au/Ag structures were calculated for structures annealed at *230°C* – the maximum *PF* reached $2.7 \cdot 10^{-4}$ *W/m·K²*. For Ge:Sb/Ag test structures the maximum *PF* reached $1.8 \cdot 10^{-5}$ *W/m·K²* at was obtained for thin films annealed at 180°C. In addition, it can be seen that in the case of Ge:Au/Ag structures pos-process annealing significantly influenced the value of the power factor. However, the highest annealing temperature led to a significant decrease in PF – which is directly related to the decrease in electrical conductivity. Such a clear effect of the annealing temperature on the properties of the films is not observed for Ge:Sb/Ag structures.

The major electric and thermoelectric parameters of investigated gold- and antimony-doped germanium thin films were determined as a function of structure temperature in the range form *320 K* to *495 K*. In the Table 2, the electrical conductivity, Seebeck coefficient and power factor at *400 K* are presented. Also, on the basis of the power factor measurements, the dimensionless figure of merit ZT was estimated (Equation 3). In the described studies, the thermal conductivity value was assumed to be equal *1 W/m·K*. Such an assumption was

made on the basis of the previous results presented in the literature describing thin film thermoelectric materials, as well as the studies in which the thermal conductivity of the substrate was assumed for the thermal conductivity of the layer.

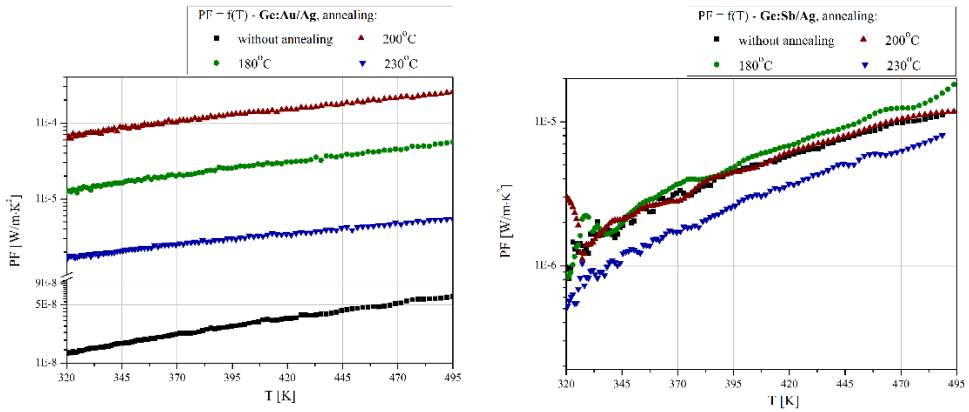

Fig. 6. The power factor *PF* as a function of the temperature *T* before and after annealing: (a) the Ge:Au/Ag test structures, (b) the Ge:Sb/Ag test structures

Table 2. Electric and thermoelectric properties of the selected Ge:Au/Ag and Ge:Sb/Ag test structures at *400 K*: electrical conductivity *σ*, Seebeck coefficient *S*, power factor *PF* and dimensionless figure of merit *ZT*

Test structure	**T [°C]**	**σ [S/m]**	**S [μV/K]**	**PF [W/m·K²]**	**ZT**
Ge:Au/Ag	without annealing	23.5	-35.2	$2.9 \cdot 10^{-8}$	$11.7 \cdot 10^{-6}$
	180	$1.3 \cdot 10^{4}$	-45.3	$2.7 \cdot 10^{-5}$	$10.8 \cdot 10^{-3}$
	200	$5.5 \cdot 10^{4}$	-49.2	$1.3 \cdot 10^{-4}$	$5.3 \cdot 10^{-2}$
	230	$1.2 \cdot 10^{3}$	-50.3	$3.1 \cdot 10^{-6}$	$12.3 \cdot 10^{-4}$
Ge:Sb/Ag	without annealing	25.4	-432.0	$4.7 \cdot 10^{-6}$	$19.0 \cdot 10^{-4}$
	180	20.2	-515.7	$5.4 \cdot 10^{-6}$	$21.5 \cdot 10^{-4}$
	200	18.7	-495.4	$4.6 \cdot 10^{-6}$	$18.3 \cdot 10^{-4}$
	230	10.7	-518.6	$2.9 \cdot 10^{-6}$	$11.5 \cdot 10^{-4}$

4. SUMMARY

The results showed that germanium-based thin films can be used as potential thermoelectric materials. But, in order to summarize the presented research, it should be mentioned that thermoelectric materials can be used both in micro- and nanogenerators as well as in sensor systems. These materials, which are characterized by a high power factor, mainly related to

high electrical conductivity, may be used in microgenerators. On the other hand, materials with a high Seebeck coefficient are ideal for sensor systems.

For the germanium doped with gold layers much higher values of power factor PF and dimensionless figure of merit ZT were obtained with maximum values for structures annealed at 200°C. Also, gold-doped films showed higher electrical conductivity at room temperature, up to $5.0 \cdot 10^4$ S/m. However, the germanium thin films doped with antimony showed much higher Seebeck coefficients than Ge:Au/Ag layers, which may be very important from the point of their potential application in sensors systems. Post annealing of both Ge:Sb/Ag and Ge:Au/Ag structures resulted in the increase of maximum thermoelectric voltage which caused the increase of the average Seebeck coefficient. For the Ge:Sb/Ag structures annealing caused the decrease in the power factor and *ZT* which results from the decrease in the electrical conductivity.

In conclusion, the investigated layers showed sufficiently good thermoelectric parameters to be considered in further research as thermoelectric materials used in microgenerators or as active layers in sensors. In additions, these layers can be the basis for the next study of complex thermoelectric materials, based on germanium, gold and antimony compounds and alloys.

Acknowledgement

This work was supported by statutory activity of Wrocław University of Science and Technology.

References

[1] H. J. Goldsmid, *Introduction to thermoelectricity*, Springer series in material science 121, Springer, Berlin (2010).

[2] M. H. Elsheikh et al., *A review on thermoelectric renewable energy: Principle parameters that affect their performance*, Renewable and Sustainable Energy Reviews, 30, 2014, pp. 337-355.

[3] S. Priya, D J. Inman, *Energy Harvesting Technologies*, Springer, 2009.

[4] M. Haras ; T. Skotnicki, *Thermoelectricity for IoT – A review*. Nano Energy, 2018, 54, 461-476.

[5] D. M. Rowe, *Thermoelectric Handbook: Macro to Nano*, CRC Press, 2005.

[6] D. Champier, *Thermoelectric generators: A review of applications*. Energy Conversion and Management, 2017, 140, 167-181.

[7] J.-P. Fleurial, *Thermoelectric Power Generation Materials: Technology and Application Opportunities*, Journal of The Minerals, Metals & Materials Society, 2009, 4, 79-85.

[8] Ch. Gayner, K. K. Kar, *Recent advances in thermoelectric materials*, Progress in Material Science, 83, 2016, pp. 330-382.

[9] G. J. Snyder, E. S. Toberer, *Complex thermoelectric materials*, Nature Materials, 7, 2008, pp. 105-114.

[10] M. F. Silva, J. F. Ribeiro, J. P.Carmo, L. M. Goncalves, J. H. Correia, *Thin-films for Thermoelectric Applications*. In Bhushan B. (Ed.) NanoScience and Technology, Springer, 2013, 485-528.

[11] C. Clayes, E. Simoen, *Germanium-based technologies: from materials to devices*, Elsevier, 2007, pp. 11-40.

[12] G. Beensh-Marchwicka, E. Prociów, W.Posadowski, *Preparation of thermosensitive magnetron sputtered thin films*, Vacuum, 53, 1999, pp. 47-52.

[13] P. Markowski, E. Prociów, Ł. Urbaniak, *Thermoelectric properties of thin-film germanium-based layers*, Microelectronics International, 32, 2015, pp. 115-121.

IP-DIP-BASED 3D PHOTONIC CRYSTAL STRUCTURE FOR PHOTONIC DEVICES

P. Urbancová[1*], A. Kuzma[2], D. Pudiš[1], P. Gašo[1], M. Goraus[1], J. Chovan[3]

[1]Dept. of Physics, Faculty of Electrical Engineering and Information Technology, University of Žilina, Univerzitná 1, 01026 Žilina, Slovakia
[2]Institute of Electronics and Photonics, Faculty of Electrical Engineering and Information Technology, Slovak University of Technology in Bratislava, Ilkovičová 3, 81219 Bratislava 1, Slovakia
[3]International Laser Centre, Ilkovičova 3, 841 04 Bratislava 4, Slovakia
e-mail: urbancova@fyzika.uniza.sk

Abstract: *In this paper, we present design, simulation and fabrication of three-dimensional (3D) photonic crystal structure (PhC) in IP-Dip polymer. We are focused on photonic band gap (PBG) effect of this structure for application in photonic devices. We simulated dispersion diagrams with partial PBGs, which are caused by a low refractive index of used polymer. Dispersion diagrams were simulated for woodpile structure with different filling factors using RSoft simulation tool BandSOLVE. The woodpile structure was fabricated by a commercial direct laser writing (DLW) system Nanoscribe with a nonlinear two-photon polymerization (TPP) in the volume of liquid negative IP-Dip polymer. Quality of fabricated structure was analyzed using confocal microscope and scanning electron microscope (SEM). The proposed partial PBG was investigated by transmission measurement.*

Keywords: 3D woodpile structure, photonic crystal, photonic band gap

1. INTRODUCTION

Photonic Crystals (PhCs) have become very popular and important research topic in recent years thank to their unique optical properties and broad technological application possibilities in many photonic devices [1]. PhCs have been intensively studied for use in wide range of technologies, such as semiconductors lasers, optical integrated circuits, solar cells, sensors, light-emitting diodes, optical fibers and telecommunication [2, 3]. PhCs are periodic structures of dielectric materials with alternating high and low refractive indices. The primary considerations in designing PhCs are crystal symmetry and the choice of dielectric materials to increase the index contrast between high- and low-index materials, which is crucial for achieving good photonic properties [2]. There has been significant interest in three-dimensional (3D) PhC structures in recent years aiming to exploit full photonic band gap (PBG) [4]. Among the various examples, polymer-based 3D PhCs have attracted considerable interest because they can be easily fabricated by femto-second ultrafast direct laser writing (DLW) method in single-step process. However, it is difficult to realize complete PBG in polymer PhCs due to the low refractive index contrast between polymers and air [5]. Such a 3D PhC structure fabricated in different materials, which was studied in detail, is the woodpile structure. Woodpile structure is attractive due to its full PBG and easy fabrication using common lithographic techniques [5]. This PhC structure was successfully used in some photonic applications for controlling light emission of light emitting diodes (LEDs), for particle accelerator applications and for 3D guiding of light in waveguides [6-8]. We are especially focused on the applications of polymer-based

woodpile PhC structures. There were studied diffraction properties of these structures prepared from different polymers and PBG effect of polymer woodpile prepared by DLW method [9, 10].

In this paper, we present design, simulation and fabrication of polymer-based 3D woodpile PhC structure. We designed woodpile structure with horizontal period of 500 nm and we simulated dispersion diagrams with partial PBGs for different filling factors of structure. As a fabrication tool we used commercial 3D laser lithogprahy system Photonic Proffesional GT from Nanoscribe GmbH based on DLW method with nonlinear two-photon polymerization (TPP) in the volume of liquid IP-Dip polymer. The PBG of fabricated woodpile structure was investigated by transmission measurement.

2. DESIGN OF A WOODPILE STRUCTURE AND SIMULATION

Woodpile is an important 3D PhC structure, which was introduced by Ho et al [11] and first demonstrated at optical frequencies by Li et al [12]. Here we present detail crystal structure and simulated dispersion diagrams for woodpile structures with different parameters.

2.1. Crystal structure and design

Woodpile is a diamond-like structure formed by a stack of alternating orthogonal oriented dielectric columns with rectangular profile of width w and height $h = c/4$. The stacking sequence of a unit cell consists of four layers. The first and the second layer is created by dielectric columns separated by horizontal period a and oriented perpendicular to one another. The third and the fourth layers are shifted by a half of horizontal period ($a/2$) relative to the first two layers. Vertical period c corresponds to the four-layer sequence. In consideration of the structure parameters a and c, the dielectric columns are generally arranged in body-centered tetragonal (*bct*) lattice. At two special ratios of these parameters, the lattice symmetry of structure becomes cubical. If $c/a = 1$, the dielectric columns are arranged in body-centered cubic (*bcc*) lattice and for $c/a = \sqrt{2}$ structure has the face-centered cubic (*fcc*) lattice symmetry [13, 4].

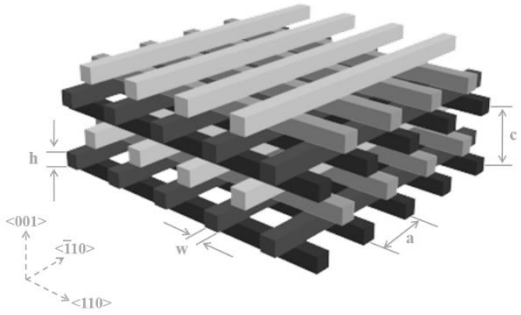

Fig. 1. Design of the woodpile structure with dielectric columns arranged in four-layer sequence

The arrangement of woodpile layers with structure parameters is shown in Fig. 1. It was shown that the woodpile structure produces full PBG if the permittivity of used material is

$\varepsilon \geq 4.6$ [14]. In consideration to the very small dielectric constant of IP-Dip polymer ($\varepsilon = 2.34$) [15], only partial PBGs in some directions are expected.

2.2. Dispersion diagram simulation

We designed the woodpile structure with *fcc* lattice symmetry ($c/a = \sqrt{2}$), considering that the *fcc* lattice has the most spherical Brillouin zone (Fig. 2b) and thus creates the widest PBG [13]. Except the refractive index of IP-Dip polymer, another important parameter for the formation of partial PBG is filling factor (*ff*), which is characterized as a ratio of dielectric column width to horizontal period ($ff = w/a$). The *ff* was changed in range of 10% – 80%. We simulated dispersion diagrams for woodpile structure of *fcc* symmetry with following parameters: $a = 0.500$ μm, $c = 0.705$ μm, $h = 0.250$ μm and values of w was changed from 0.050 μm to 0.400 μm. In Fig. 2a, there is shown a simulation domain of woodpile structure, which is used for viewing the 3D index profile. Simulation domain represent a single unit cell, from which a supercell for calculation of dispersion diagrams is composed. In many cases, the numerical domain does not have the same shape as the physical PhC structure (as we can see the shape and resolution of simulation domain of our woodpile structure in Fig. 2a).

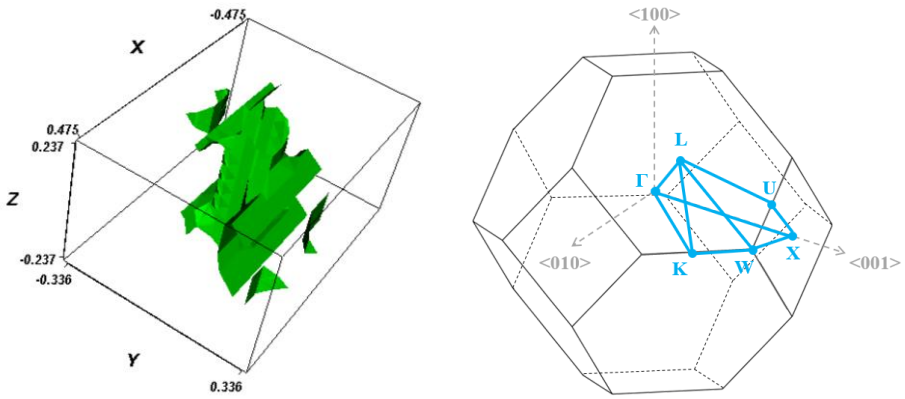

Fig. 2. a) 3D view of the simulation domain, b) the first Brillouin zone of *fcc* lattice

Dispersion diagrams were simulated using RSoft simulation tool BandSOLVE for *fcc* ***k***-path: X – U – L – Γ – X – W – K (Fig. 2b). In dispersion diagrams (Fig. 3) we found the partial PBGs in Γ – X <001> and Γ – L <111> directions. Although the Γ – L direction shows wider PBG, the Γ – X direction is preferred regarding to the simpler surface application of woodpile structure on photonic devices. Dispersion diagrams in Fig. 3 were simulated for different filling factors *ff* = 20 – 70%. There was not found partial PBG in Γ – X direction for *ff* outside this interval. With increasing of *ff*, there is evident decrease of normalized frequency. Dispersion diagrams for *ff* = 20% – 70% are shown in Fig. 2a-f. The widest partial PBG in Γ – X direction is for *ff* = 40% (Fig. 2c) and *ff* = 50% (Fig. 2d). For *ff* = 40% was found the partial PBG at $a/\lambda = 0.55 – 0.59$, what corresponds to the wavelength range $\lambda = 847 – 909$ nm calculated for horizontal period $a = 500$ nm and for *ff* = 50% at $a/\lambda = 0.54 – 0.56$ and wavelength range $\lambda = 893 – 926$ nm. We expect partial PBG around these

wavelength ranges because of the resolution limit of system Nanoscribe, which is 200 nm laterally.

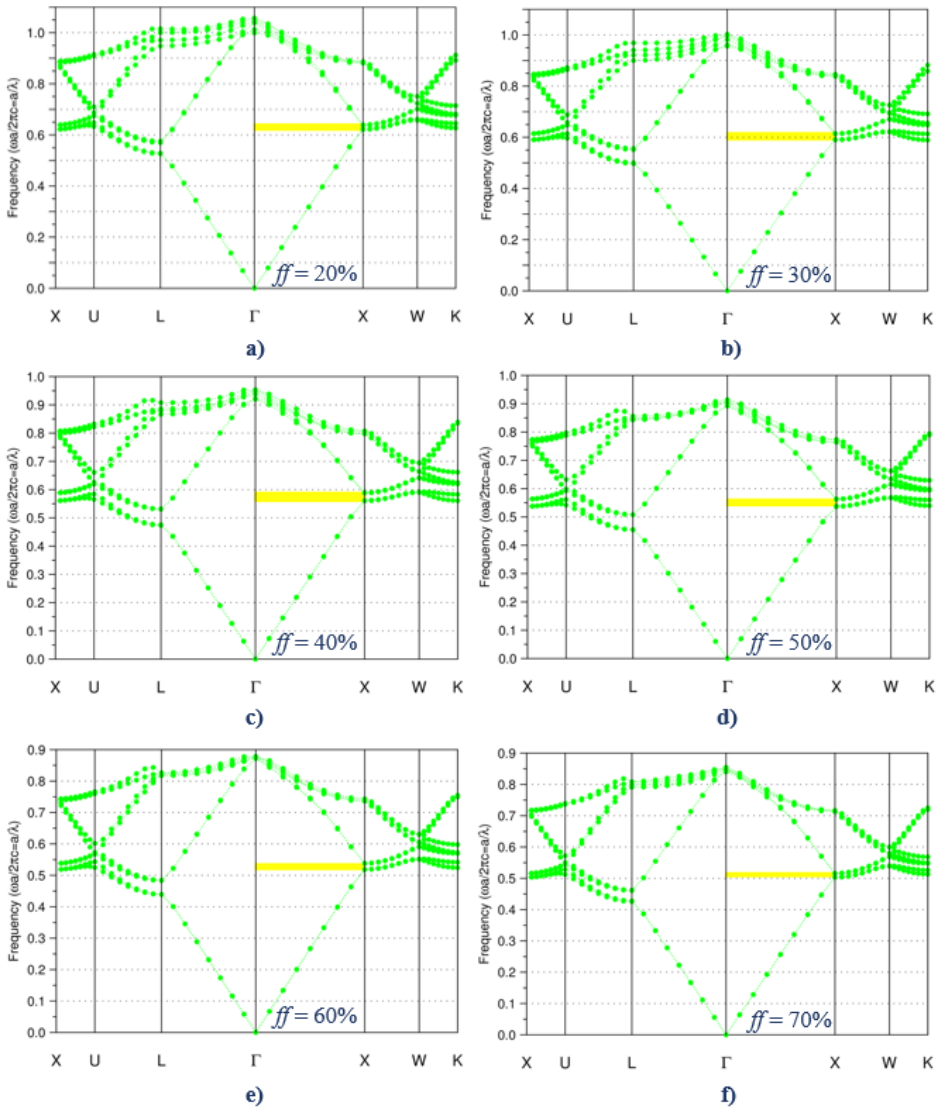

Fig. 3. Calculated dispersion diagrams using RSoft simulation tool BandSOLVE with partial PBGs in Γ – X <001> direction for: a) *ff* = 20% – f) *ff* = 70 % with increment of 10%.

3. FABRICATION AND RESULTS

In our experiment, we used commercial 3D laser lithography system Photonic Proffesional GT. The excitation light source is a Ti-sapphire femtosecond laser with a wavelength

780 nm, pulse width of 100 fs and a repetition rate of 80 MHz. As a photosensitive material the negative high-resolution IP-Dip photoresist with refractive index $n = 1.52$ at wavelength 780 nm was used [16]. The laser beam is focused by a high numerical aperture (NA) objective lens (63×, NA = 1.4). After fabrication, the sample was developed in PGMEA developer and rinsed in isopropyl alcohol.

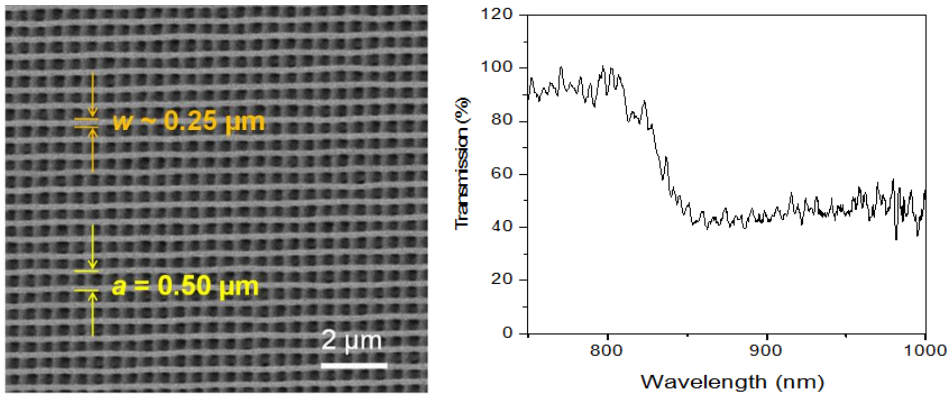

Fig. 4 a) SEM image of fabricated woodpile structure with $a = 0.5$ µm, b) measured transmission characteristic of woodpile structure in Γ – X direction forming PBG in near infrared spectrum.

The quality of prepared structure was studied by SEM (Fig. 4a). Fabricated woodpile structure with period $a = 0.5$ µm shows regular and well separated dielectric columns with width lower than $w = 0.25$ µm (*ff* is slightly lower than 0.5). The PBG effect and optical properties were investigated by transmission measurement in Γ – X direction. In the measured transmission spectrum (Fig. 4b) is evident decrease at wavelength range 860 – 1000 nm, what slightly differs from the theoretically expected position of the PBG (λ ~ 890 – 930 nm). We suppose, that this disagreement between experimental and theoretical values is caused by inhomogeneous *ff* over the whole volume of prepared woodpile structure. Especially, the developing process could be insufficient, what increase the *ff* and causes the PBG red shift. By optimization of the laser lithography parameters as laser power and scanning speed we can achieve more homogeneous structure across the whole volume.

4. CONCLUSION

In this paper, we presented design, simulation and fabrication of IP-Dip polymer-based woodpile structure. We simulated dispersion diagrams of woodpile structure with a horizontal period of 0.5 µm as function of filling factor, which influences the PBG. The woodpile was fabricated by 3D laser lithography system using DLW method. Fabricated structure showed well separated dielectric columns with width lower than 0.25 µm. For this structure we estimated the PBG from simulations at wavelength range of 890-930 nm. The measured transmission spectrum shows broad-band PBG at wavelength range 860 – 1000 nm, which was influenced by inhomogeneous structure across the volume of woodpile structure. For achievement more homogeneous 3D PhC structures, there is a need for optimization of fabrication process parameters. Our results

document the application possibilities of polymer-based 3D PhC structures with PBG effect in photonic devices.

Acknowledgement

This work was supported by the Slovak National Grant Agency under the projects no. VEGA 1/0540/18, VEGA 1/0278/15 and VEGA 1/0886/17 and the Slovak Research and Development Agency under the project no. APVV-16-0129, APVV-15-0763 and APVV-17-0662.

References

[1] X. Xi, et al., *Results Phys.* 7, 4303-4309 (2017).
[2] L. Sun, et al., *PNAS* 115, 1-6 (2018).
[3] G. Freymann, et al., *Adv. Funct. Mater.* 20, 1038 (2010).
[4] X. Zheng, et al., *Appl. Sci.* 8, 1087 (2018).
[5] L. J. Chen, et al., *Proc. Of SPIE* 9671, 967127 (2015).
[6] S. Ogawa, et al, *Science* 305, 227-229 (2004).
[7] Ch. Lee, et al., *AIP Conf. Proc.* 1777, (2016).
[8] K. Gondaira, et al., *Opt. Express* 24, 13518-13526 (2016).
[9] M. Rybin, et al., *Crystals* 5, 61-73 (2015).
[10] B. Brüser, et al., *Appl. Optics* 51, 6732-6737 (2012).
[11] D. Cassagne, C. Jouanin, D. Bertho, *Phys. Rev.* 52, 2217-2220 (1995).
[12] H. Y. Ryu, J. K. Hwang, Y. H. Lee, *Phys. Rev. B* 59, 5463-5469 (1999).
[13] K. B. Samusev, Phys. *Solid State*+ 57, 2494-2501 (2015).
[14] G. Subramania, *Opt. Express* 15, 13049-13057 (2007).
[15] T. Gissibl, *Opt. Matter. Express* 7, 2293-2298 (2017).
[16] Nanoscribe GmbH, http://www.nanoscribe.de/en/products/, (2017).

SIMULATION OF NEAR FIELD EXPOSITION IN UV LITHOGRAPHY

A. Zawadzka[1*], K. Indykiewicz[1], R. Paszkiewicz[1]

[1]Faculty of Microsystem Electronics and Photonics, Wrocław University of Science and Technology, Janiszewskiego Street 11/17, 50-372 Wrocław, Poland
*e-mail: agnieszka.zawadzka@pwr.edu.pl

Abstract: *Optical lithography is a technology that enables the transfer of designed patterns from the mask into a photopolymer surface by UV or DUV light. A major limitation of this process is a diffraction phenomenon, because of the bending of the light on the mask edges that causes falsities in shape and dimensions of designed paths. The presented work will discuss the differences in: wave energy absorption, near and far field, resist layer and the resolution limits in photolithography exposition. The experimental model simulates the light wave propagation through the lithography system. The electric field distribution, dependence on the resist and opaque mask layer thickness will also be analyzed in the work.*

Keywords: near field optical lithography, diffraction limit, lithography simulations

1. INTRODUCTION

Nowadays, due to the rapid advances in electronics, nanotechnology, physics of nanostructures or microbiology, various microfabrication methods have been developed. Technologies such as electron beam lithography or nanoimprint lithography are increasingly used [1, 2]. Despite this, photolithography is still a competitive method when it comes to the price and time of processing, and remains a predominant technology in the semiconductor industry.

The most relevant issue in the lithography is the so-called resolution, the spatial width of the smallest feature which could be printed. Years ago this value was twice the wavelength used to illuminate. Today, the industry needs much higher resolution. In the optical lithography this value differs significantly from other lithography methods mentioned above, due to the physical restriction. The main reason for this is the diffraction limit of light, which defines the minimum size of windows, formulated as Rayleigh limit (1), where d is the minimum feature dimension, λ the illumination wavelength, NA is the numerical aperture of the system and k a parameter dependent on resist material and process technologies, usually about unity [3].

$$d = k\lambda/NA \quad (1)$$

Based on the equation, there are two possibilities to reduce the spatial extension of the light spot, the NA increase or the wavelength decrease. In the optical lithography the major trend follows the second approach. Practically, the minimum feature size is a half of the working wavelength used to exposure [4, 5].

One of the methods to overcome the resolution limit is the usage of an alternative DUV or EUV light sources. Unfortunately using shorter wavelength causes other problems, described in [6, 7]. Thus, simultaneously, other ways are sought to obtain a smaller pattern dimension.

In the past decades, a number of schemes have been studied to improve the lithography resolution. Due to its primarily dependence on the distance between the mask and the sample, many of methods involving near field (NF) optics, to overcome the diffraction limit and provide highly precise fabrication in nanoscale has been checked [8, 9]. It is related to the presence of high spatial frequency components in optical field in the thin resist which enables significant enhancing the electromagnetic field intensity and moreover makes possible to obtain proper focusing at small dimension, defined by mask pattern, due to the evanescent properties [10].

The principle of the near field optical lithography is to ensure the distance between the mask pattern and the border of substrate and resist to be much less than the wavelength of the light used to expose [11]. The schematic diagram of the near and the far field is presented in the Figure 1a. Figure 1b shows the electric field intensity distribution in the plane parallel to UV illumination direction for different printing system, according to different distances between mask and resist, correspondingly from the shortest gap; contact, proximity and projection.

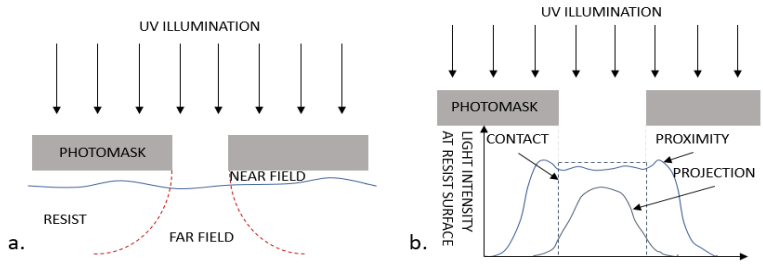

Fig. 1. Schematic diagrams illustrating the near field and far field optical lithography (a) and the intensity for three various printing systems (various widths of the gap between the mask and the resist) (b)

The near field optical lithography demands not only the smallest as possible gap between the resist layer and the mask. Taking into consideration the wave penetration depth in the polymer and the change of resist's chemical properties, the photoresist thickness is equally important. Providing the sum of these widths to be less than the wavelength, the resolution beyond the diffraction limit is possible [12]. Typically, polymer layers thickness of below 1 μm are widely used. As mentioned previously, the optimum value of below 400 nm is required to ensure the NF exposition. Thinner layers obtaining by diluting also provide an almost homogeneous exposure and proper depth profile of pattern. Although, for excessively thin layers, the pattern transfer using etching techniques becomes difficult [11]. The aerial image in optical lithography is formed by the light which illuminates the sample surface covered with resist through the mask with pattern and selectively changes the polymer solubility. Nevertheless, during this process the light beam is both refracted and reflected by the resist and substrate and the final profile of modified structure depends strongly on the distribution of these phenomenon. Moreover, the light wave in photolithography propagates in the air and in a transparent material of mask, encounting an obstacle which is an opaque layer with pattern. Around the edges it bends and spreads behind the barrier, affecting the falsity of printing pattern shapes [13, 14]. It is more important that usually tens of objects are exposed at the same time and light propagates

through near located slits, where the diffraction and interference effects are even more explicit [15].

2. SIMULATIONS AND RESULTS

The resolution achievement of the NF optical lithography depends on many factors. The understanding of the NF phenomenon is required to guide future experiments. To achieve this and specify the impact of diffraction and interference on the electric field distribution, the simulations were conducted.

2.1. Simulations object and conditions

The behavior of electromagnetic field when passing through the mask with Cr opaque layer of various thickness was examined. Furthermore, the electric field distribution for different thickness of photopolymer was investigated. Simulation was made through using the RF module of Comsol Multiphysic software, which solve the Maxwell's equations by the finite element method. Figure 2a illustrates the used lithography system (LS) and defines the Cartesian coordinate system. Figure 2b shows the scheme of test lines for the further electric field distribution studies along the x-axis at various sections of structure.

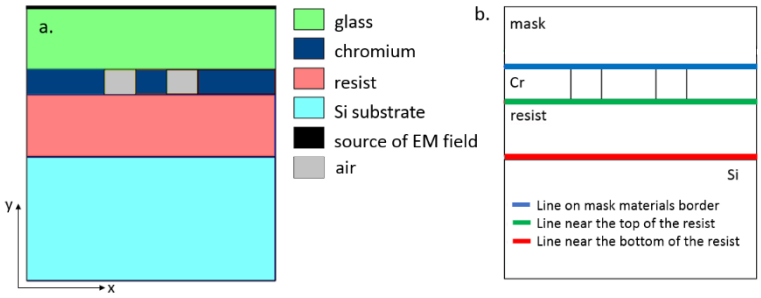

Fig. 2. The lithography system with coordinate system used for simulations (a) and the scheme of test lines of the electric field distribution along the x-axis at various sections of structure

While examining the possibilities of obtaining sub-micrometers patterns in resist, close attention has to be paid for the results of the model with dimensions slits comparable or smaller than the wavelength light, where occurring NF physical effects played a crucial role [16]. The simulations were conducted for LS system with 200 nm slots and path widths, which corresponds to the half of the wavelength.

To determine the relationship between the direction of electric field oscillations and the way of its propagation in the LS, two different polarization possibilities of the light were simulated. For the 405 nm wavelength the TE mode, where the electric field is perpendicular to the plane of the LS were found the wave extincts passing through the slots. Together with TM polarized light and electric field parallel to the plane LS, the light transmits through the mask. For this condition, further simulations were carried out.

Hereinabove mentioned, the higher resolution is obtained by reducing the wavelength of used light. Thus, the experiments for shorter wavelengths were excluded from the study and the impact of other important factors such as polymer and Cr layer thicknesses

on electric field distribution were studied. The preliminary field distribution simulations omitted the change of the resist chemical properties over time.

2.2. Results

The simulations of the optical near field exposition process have been carried out. Firstly, the influence of the opaque mask layer thickness on electric field distribution along the x-axis was examined and is shown in the Figure 3, at various sections of structure, according to the Figure 2b. Three different chromium thicknesses 100, 50, 20 nm were simulated. For all results the electric field boundaries are widened which is clearly seen for the mentioned red and green line placed near the top of resist (Fig 3abc). This is due to the diffraction phenomenon, which causes bending of light at the edges and may affect pattern falsities. Simultaneously, the amplitude of the red line, corresponding to the electric field distribution at the bottom of the resist changes slightly when reducing the Cr thickness and shows that there is no significant relationship between the thickness of the opaque mask layer of chromium and the electric field distribution and amplitude for examined LS parameters.

Notwithstanding, due to the demanded mask opaque layer optical shadowing without any voids neither thinnings and proper mechanical strength the 20 nm Cr forms too slender layer [17]. This indicates that the suitable value of mask thickness for further simulations is 50 nm (Fig. 3b).

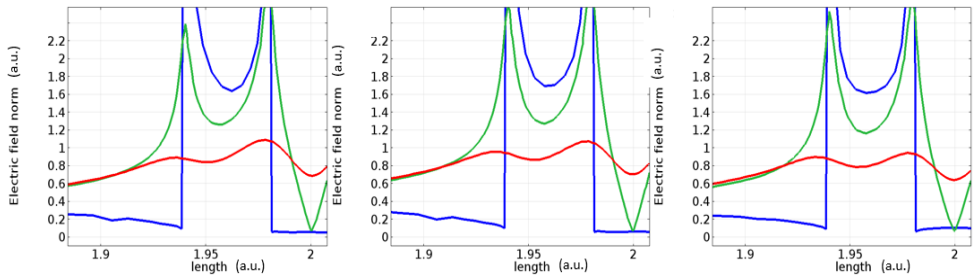

Fig. 3. The electric field distribution of line-space structures along the x-axis at various sections of structure as a function of the mask thickness of 100 nm (a), 50 nm (b) and 20 nm (c) for 100 nm photoresist and 200 nm slits and paths

Numerical calculation of the near field lithography in the case of light wave diffraction has also been performed to examine the dependence of the 300 nm, 100 nm and 50 nm photoresist thickness on the propagation of waves. For the thinner layer of the polymer (50 nm), the sharp borders of the electric field intensity at the mask edges are observed (Fig. 4c). This naturally entails the better contrast of exposing fields and provides the near field lithography. Simultaneously, too small resist layer thickness causes difficulties with etching processes [9]. For thicker polymer layer (300 nm), the wave penetration depth is unproper due to the vanishing of high frequency electric field components along with moving away from the slits in mask and the light penetrates slightly into the bottom of the resist (Fig. 4a). The proper value of photoresist thickness for further research is 100 nm (Fig. 4b).

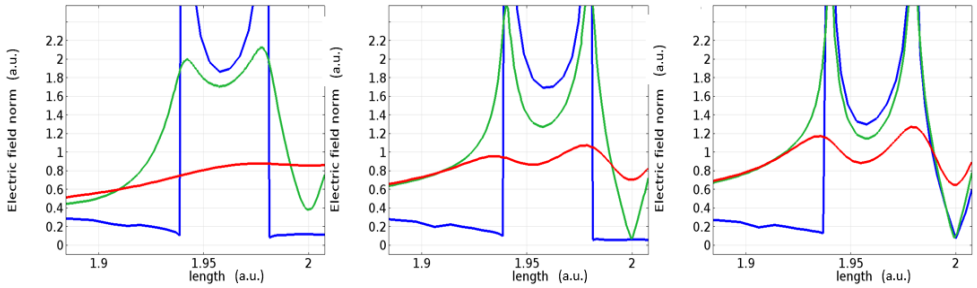

Fig. 4. The electric field distribution of line-space structures along the x-axis at various sections of structure as a function of the photoresist thickness of 300 nm (a), 100 nm (b) and 50 nm (c) for 50 nm Cr mask and 200 nm slits and paths

3. CONCLUSION

An overview of the theoretical resolution limits in optical lithography has been presented. The theoretical restrictions for obtaining sub-wavelength patterns were depicted as well as the advantages and examples of using the near field in optical lithography. Using the numerical electromagnetic simulation of lithography system and solving the Maxwell's equations by the finite element method, the resolution limits and factors which significantly affect the light propagation way have been investigated. The best result of the electric field distribution was obtained for 100 nm photopolymer, while 50 nm was chosen as the appropriate Cr mask thickness. Explicit differences in the electric field intensity were observed for different resist thickness. For 300 nm photoresist the value of the electric field in slits was almost two times higher than for 50 nm layer. The influence of diffraction phenomena on the resist exposure process has been studied.

In this work there was demonstrated that the exposing features of dimensions narrower than the wavelength of illuminated source is possible under certain conditions. The conducted simulations indicate the reasonability of further examinations of this lithographic method. Nevertheless the precise determination of the possibility of obtaining high resolution requires further simulations and experimental work which will be carried out in our laboratories.

Acknowledgement

This work was co-financed by the National Centre for Research and Development grants TECHMATSTRATEG No.1/346922/4/NCBR/2017, the National Science Centre grant No. DEC-2015/19/B/ST7/02494, Wroclaw University of Technology statutory grants and by the Slovak-Polish International Cooperation Program. This work was accomplished thanks to the product indicators and result indicators achieved within the projects co-financed by the European Union within the European Regional Development Fund, through a grant from the Innovative Economy (POIG.01.01.02-00-008/08-05) and by the National Centre for Research and Development through the Applied Research Program Grant No. 178782 and Grant LIDER No. 027/533/L-5/13/NCBR/2014.

References

[1] Y. Chen, *A review. Microelectronic Engineering*, 135, 57-72 (2015).

[2] M. C. Traub, W. Longsine, V. Truskett. *Advances in nanoimprint lithography. Annual review of chemical and biomolecular engineering*, 7, 583-604 (2016).

[3] M. Born, E. Wolf, *Principles of Optics*, Pergamon Press, Oxford (1987).

[4] A. A. Maznev, O. B. Wright, *Upholding the diffraction limit in the focusing of light and sound*, arXiv:1602.07958 (2016).

[5] S. Okazaki, *Journal of Vacuum Science & Technology B: Microelectronics and Nanometer Structures Processing, Measurement, and Phenomena* 9, 2829 (1991).

[6] M.C. Marconi, P. Wachulak, *Progress in Quantum Electronics*, 34, 173-190 (2010).

[7] C. Williams, P. Kok, et al., *Informatik – Forschung und Entwicklung*, 21, 73 (2006).

[8] V. Dryakhlushin, A. Yu.Klimov, V. Rogov, N. Vostokov *Applied Surface Science* 248, Issues 1–4, 200-203 (2005).

[9] M.K. Herndon, R.T. Collins, et al., *Appl. Phys. Lett.*, 74, 141 (1999).

[10] M. Terakawa, N. Nedyalkov, *Advanced Optical Technologies*, 5(1), 17-28 (2016).

[11] M. Alkaisi, R. J. Blaikie, R.J., S. McNab. Nanolithography in the Evanescent Near Field. *Advanced Materials* 13. 877-887 (2001).

[12] M. M. Alkaisi, R. J. Blaikie, et al., *Appl. Phys. Lett.* 75, 3560 (1999).

[13] I. Aviani, B. Erjavec, *Phys. Educ*. 46, 134–136 (2011).

[14] M. Davidović, D. Vasiljević, M. Božić, *Настава физике* 3, 55–59 (2016).

[15] Y. Geints, A Zemlyanov, *Quantum Electronics*. 46. 644-649 (2016).

[16] M. Guillaumee, *Optical Transmission Through Sub-Wavelength Slits in Metals*, Ecole Polytechnique Federale de Lausanne, Swiss (2010).

[17] M. Chen, S. Yu, N. Luo, Y. Gao, *Optik – In Int. J. Light Electron Opt*, 119, 633-636 (2007).